TECHNISCHE UNIVERSITÄT MÜNCHEN

Optical Mercury Magnetometry for Fundamental Physics Experiments

Bernd Taubenheim

Vollständiger Abdruck der von der Fakultät für Physik der Technischen Universität München zur Erlangung des akademischen Grades eines

Doktors der Naturwissenschaften (Dr. rer. nat.)

genehmigten Dissertation.

Vorsitzender:	Prof. Dr. Björn Garbrecht
Prüfer der Dissertation:	
1.	Prof. Dr. Peter Fierlinger
2.	Prof. Dr. Susanne Mertens

Die Dissertation wurde am 22.11.2017 bei der Technischen Universität München eingereicht und durch die Fakultät für Physik am 06.03.2018 angenommen.

ABSTRACT

Contemporary searches for physics beyond the Standard Model (BSM) using spin-clocks recently gained increased attention. New proposed light degrees of freedom as well as established quantities like electric dipole moments (EDMs) can be probed well with such experiments while being in principal inaccessible in accelerator experiments. This thesis describes progress in optical mercury magnetometry and mercury co-magnetometry in which mercury vapor co-habitates the same volume as ultra-cold neutrons (UCNs) in neutron electric dipole moment (nEDM) experiments during the measurement of the spin precession frequencies. New systematic effects are discussed that will become important in nEDM experiments that aim to achieve an uncertainty smaller than 1×10^{-26} e cm. A laser driven magnetometry setup is described with an active control of the laser frequency and power, and an optical readout that is optimized for co-magnetometry. Doppler-free spectroscopy is used to measure spectroscopic properties of mercury to reduce the uncertainty of the magnetic field measurement with the magnetometer. Furthermore, Doppler-free techniques are optimized for the special needs of frequency-locking a laser that is used in mercury magnetometry.

As the precession frequency of mercury atoms is shifted by near resonant light by an amount depending on the detuning from resonance (light shift effect), controlling the laser frequency is critical to avoid large shifts of the precession frequency caused by the readout light. Only for one frequency that is close to, but not exactly on resonance, the light shift effect is zero. When the atomic spectrum of mercury is used as a reference for the laser frequency, it is thus important to know the properties of the mercury spectrum with a high accuracy. A particularly important value is the relative isotope shift ΔIS of the ${}^1S_0 \rightarrow {}^3P_1$ transition between ^{199}Hg and ^{204}Hg. This shift was determined using Doppler-free spectroscopy to be (94.3 ± 0.2) MHz which reduces the uncertainty of this value by two orders of magnitude compared to previously published results. A spectroscopy experiment comprising two Doppler-free spectroscopy setups in parallel was conducted to measure the Stark shift of the ${}^1S_0 \rightarrow {}^3P_1, F = 1/2$ transition in ^{199}Hg using Doppler-free spectroscopy for the first time.

The mercury magnetometry system that was developed in the scope of this thesis can be used for pure mercury magnetometry and for mercury co-magnetometry. The uncertainty of the previously published value of ΔIS caused uncertainties of nEDM measurements when this system is used in the order of 1×10^{-27} e cm and systematic shifts in the order of 1×10^{-29} e cm. The new measurement of ΔIS reduces these uncertainties by a factor of 100. Another new uncertainty that will become relevant if mercury co-magnetometers are used in nEDM experiments is caused by the DC Stark shift. If this effect is not taken into account, it can also cause statistical uncertainties in the order of 1×10^{-27} e cm and systematic effects in the order of 1×10^{-29} e cm. A way to avoid these uncertainties by adapting the laser frequency depending on the electric field is discussed.

ZUSAMMENFASSUNG

Auf der Suche nach Physik jenseits des Standardmodells haben Spin-Uhren zuletzt an Bedeutung gewonnen. Neu vorgeschlagene leichte Freiheitsgrade sowie etablierte Größen wie elektrische Dipolmomente (EDMs) können mit solchen Experimenten gut untersucht werden, während sie in Experimenten mit Beschleunigern nicht zugänglich sind. Präzessionsexperimente mit Quecksilberatomen waren besonders bei der Suche nach EDMs erfolgreich. Diese Arbeit beschreibt den Fortschritt in optischer Quecksilbermagnetometrie und Quecksilber-Co-Magnetometrie, bei welcher Quecksilberdampf während der Präzessionsmessung das selbe Volumen einnimmt wie Ultrakalte Neutronen (UCNs) in einem Neutronen-EDM (nEDM) Experiment. Es werden systematische Effekte diskutiert, die Bedeutung erlangen werden wenn nEDM-Experimente eine Auflösung besser als $1\times10^{-26}\,e\,\mathrm{cm}$ erreichen wollen. Ein Laserbasierter Magnetometrie-Aufbau wird beschrieben, der über eine aktive Regulierung der Lichtfrequenz und -leistung verfügt, sowie über eine Ausleseelektronik die für Co-Magnetometrie optimiert ist. Dopplerfreie Spektroskopie wird verwendet, um spektroskopische Eigenschaften von Quecksilber zu untersuchen, mit dem Ziel, die Unsicherheit der Magnetfeldmessungen mit dem Magnetometer zu verringern. Außerdem werden Dopplerfreie Spektroskopietechniken bezüglich der speziellen Anforderungen der Frequenzstabilisierung eines Lasers in einem Quecksilbermagnetometer optimiert.

Da die Präzessionsfrequenz von Quecksilberatomen durch Licht mit einer Frequenz nahe der Resonanz abhängig von der Verstimmung der Lichtfrequenz von der Resonanz verschoben wird (Light-Shift), ist es besonders wichtig, die Frequenz des Laserlichts genau einstellen zu können, um zu vermeiden, dass das Ausleselicht die Präzessionsfrequenz verschiebt. Nur bei einer Frequenz die nahe bei (aber nicht genau auf) der Resonanz liegt, verursacht das Ausleselicht keinen Light-Shift. Wenn das Atomspektrum von Queckilber als Referenz für die Laserfrequenz herangezogen wird, ist es daher wichtig die Eigenschaften des Quecksilberspektrums mit einer hohen Genauigkeit zu kennen. Ein besonders wichtiger Wert ist die relative Frequenzverschiebung $\Delta\mathrm{IS}$ des ${}^1S_0 \rightarrow {}^3P_1$ Übergangs zwischen ${}^{199}\mathrm{Hg}$ und ${}^{204}\mathrm{Hg}$. Diese Verschiebung wurde mit Hilfe von Dopplerfreier Spektroskopie auf $(94.3\pm0.2)\,\mathrm{MHz}$ gemessen, was die Unsicherheit von $\Delta\mathrm{IS}$, verglichen mit zuvor veröffentlichten Werten, um zwei Größenordnungen reduziert. Ein Spektroskopieexperiment mit zwei parallelen Dopplerfreien Spektroskopieaufbauten wurde durchgeführt, um den Stark-Shift des ${}^1S_0 \rightarrow {}^3P_1, F = 1/2$ Überganges in ${}^{199}\mathrm{Hg}$ zum ersten Mal mittels Dopplerfreier Spektroskopie zu messen.

Das Quecksilbermagnetometriesystem, das im Rahmen dieser Arbeit entwickelt wurde, kann sowohl für reine Quecksilbermagnetometrie als auch für Co-Magnetometrie verwendet werden. Die Unsicherheit des zuvor veröffentlichten Wertes für $\Delta\mathrm{IS}$ verursachte statistische Unsicherheiten bei einer Nutzung dieses Magnetometriesystems in einer nEDM Messung in der Größenordnung $1\times10^{-27}\,e\,\mathrm{cm}$,

und systematische Verschiebungen des Ergebnisses in der Größenordnung 1×10^{-29} e cm. Die neue Messung von ΔIS verringert diese Unsicherheiten um einen Faktor 100. Eine weitere neue Unsicherheit die wichtig sein wird wenn ein Quecksilber Co-Magnetometer in einem nEDM-Experiment eingesetzt wird, steht im Zusammenhang mit dem DC-Stark-Shift. Wenn dieser Effekt nicht berücksichtigt wird kann er ebenfalls zu statistischen Unsicherheiten in der Größenordnung 1×10^{-27} e cm, und zu systematischen Effekten in der Größenordnung 1×10^{-29} e cm führen. Es wird ein Weg aufgezeigt, diese Unsicherheiten mittels Anpassens der Laserfrequenz an das elektrische Feld zu vermeiden.

CONTENTS

ACRONYMS

EDM electric dipole moment

nEDM neutron electric dipole moment

HgEDM mercury electric dipole moment

UCN ultra-cold neutron

EOM electro-optic modulator

AOM acousto-optic modulator

PID proportional-integral-derivative

TA tapered amplifier

SNR signal-to-noise ratio

MSR magnetically shielded room

SFC surrounding-field compensation

SQUID superconducting quantum interference device

VLS vector light shift

NLP no-light-shift point

DAVLL dichroic atomic vapor laser lock

magnetometer transition transition ${}^1S_0 \rightarrow {}^3P_1$, $F = \frac{1}{2}$ in ${}^{199}\mathrm{Hg}$

PBS polarizing beam-splitter

PCB printed circuit board

ND filter neutral-density filter

PTB Berlin Physikalisch-Technische Bundesanstalt Berlin

NV nitrogen-vacancy

BSM beyond the Standard Model

SM Standard Model of particle physics

SEOP Spin-Exchange Optical Pumping

CP Charge-Parity invariance

T Time invariance

IID independent and identically distributed random variables

UV ultra violet

co-magnetometer co-habitating magnetometer

CRLB Cramer-Rao lower bound

CKM Cabibbo-Kobayashi-Maskawa

Part 1

INTRODUCTION

1.1 PROBING FUNDAMENTAL PHYSICS AT LOW ENERGIES

As the Standard Model of particle physics (SM) is currently one of the most successful and universal models aiming to describe nature, experiments all over the world are testing its limits in order to improve our understanding of physics. Investigating effects that can not be explained by the SM and searching for effects that are predicted by the SM are important paths towards a more complete model of physics.

For instance, the particles included in the SM can not explain dark matter [1] or dark energy [2], which seem to be necessary to explain cosmological observations. The SM also fails to explain why we observe so much more matter than anti-matter in the universe [3]. Examples for testing the limits of the validity of the SM are experiments searching for violations of Lorentz invariance or CPT symmetry, which are required by the SM [4].

One way to test the SM and search for physics beyond the Standard Model (BSM) is to create higher momenta in the rest frame of colliding particles in order to observe high energy effects that are of minor relevance at energies used in previous experiments. This recently lead to the observation of the Higgs boson that was predicted by the SM [5, 6] at the Large Hadron Collider [7, 8].

Another way to test the SM is to observe interactions at low energies with an increasing precision to test the SM's predictions and to look for small BSM effects on top of a signal which can otherwise be well described by the SM. These kinds of experiments are ideally designed to generate a signal the potential BSM physics can contribute to, while the dominating Standard Model physics contribute in a way that is well understood. This is important to make small deviations from Standard Model physics visible on top of the Standard-Model dominated signal.

A good example for such systems is an ensemble of particles with a nonzero spin that are precessing in a well known magnetic field. The resulting signal is dominated by the interaction between the magnetic moments associated with the spins and the magnetic field. This comes down to a frequency measurement. Many potential fundamental interactions caused by BSM physics are expected to couple to the spin of the particles in a similar way as the magnetic field as this is the only vector available in the rest-frame of the particles [9]. Magnetometry with atoms or other particles like ultracold neutrons (UCNs) [10] is thus well suited to be used in searches for BSM physics.

The dominating contribution to the frequency of precessing particles with a nonzero spin comes from the magnetic field. To resolve BSM effects on top of the magnetic precession, it is favorable to use small magnetic fields and essential to know these fields as accurately as possible. A common strategy is to use a magnetic shield to reduce the effect of external magnetic fields on the experiment [11]. Then, a small artificial magnetic field is created inside the magnetic shield.

Examples for atomic magnetometers or magnetometer-like experiments being successfully used to probe fundamental physics comprise an experiment setting an upper

limit for the electron electric dipole moment (EDM) [12], Lorentz invariance [13] and a potential coupling between mass and spins [14] with a cesium magnetometer.

When searching for effects coupling to the particles spins and not the magnetic moment, it can be advantageous to use atoms with a closed electronic shell where the unpaired spin comes from a neutron, or alternatively, free neutrons. As the magnetic moments of these are typically a factor of 10^3 smaller than those of atoms with an unpaired electronic spin, the relative shift of the frequency due to a potential BSM effect becomes larger as this effect couples to the spin rather than to the magnetic moment. Examples for experiments using closed-shell atoms are the measurement of the mercury atomic EDM [15] and Lorentz invariance tests using hyperpolarized helium and xenon gas in the same storage volume [16]. Free neutrons are for example used in experiments searching for axion-like interactions [17], Lorentz invariance [18], and EDMs [19].

The ultimate goal of precession experiments is to find correlations between experimental parameters and shifts of the precession frequency. In a two level system this comes down to measuring the resonance transition frequency between the two levels. A sensitive method to do so is Ramsey's method of separated oscillatory fields [20]. Here, two coherent oscillatory pulses each flip the spins by $\frac{\pi}{2}$, separated by a free precession period where the precession frequency is not affected by the oscillatory fields. The efficiency of the second flipping pulse depends on the relative phase between the flipping field and the precessing spins that builds up during the free-precession time. After the second flip, the resulting projection of the spins on the initial polarization axis is determined. Ramsey's method of separated oscillatory fields is thus a very sensitive method to compare the energy difference in a two level system to an external frequency. With a well known external frequency, the absolute energy difference can be extracted.

EDM EXPERIMENTS

In EDM experiments with free neutrons, Ramsey's method of separated oscillatory fields prevailed in the search for frequency shifts caused by an electric field. When a particle with the angular momentum F is subject to a magnetic and an electric field, the magnetic Zeeman splitting is modified by an additional electric splitting. The precession frequency is then determined by [22]

$$\hbar\omega = -(d\boldsymbol{E} + \mu\boldsymbol{B}) \cdot \frac{\boldsymbol{F}}{F}. \tag{1.1.1}$$

By comparing the precession frequencies of particles when an electric field is applied parallel and when it is applied anti-parallel to the magnetic field, potential permanent EDMs that are correlated with the spin can be investigated. A motivation for EDM experiments is given in chapter 1.4.

Predicted values for permanent EDMs in the SM are several orders of magnitude smaller than what experiments could resolve so far. For neutrons, SM EDMs in the order of 1×10^{-30} e cm to 1×10^{-33} e cm are predicted [23] while experiments could so far only exclude that neutrons have an neutron electric dipole moment (nEDM) larger

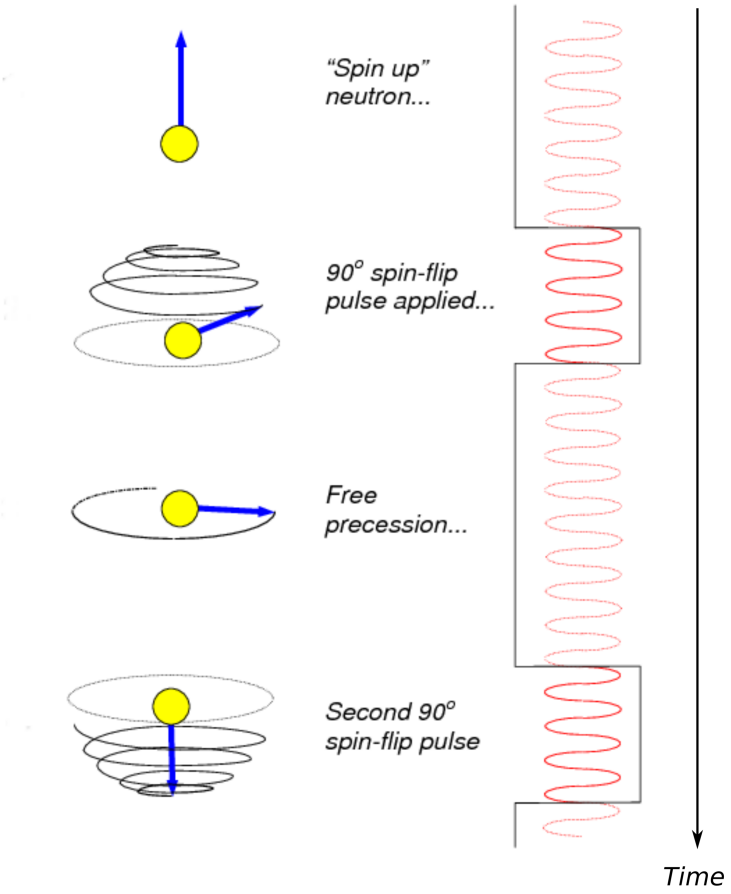

Figure 1.1.1: Visualization of Ramsey's method of separated oscillatory fields. The red signal on the right is the oscillatory magnetic field. The procedure is described in the text. Taken from [21].

than 3.0×10^{-26} e cm (90% CL) [24]. This leaves a compelling window to search for BSM physics that are causing nEDM values in between the two values stated above.

Equation 1.1.1 shows that an EDM that is smaller than 3.0×10^{-26} e cm has a tiny effect on the precession frequency compared to the large magnetic moment. This is true even in electric fields as large as $20\,\mathrm{kV\,cm^{-1}}$. In EDM experiments it is thus crucial to control and monitor the magnetic field as precisely as possible. To keep absolute fluctuations of the magnetic field small, it is favorable to use small magnetic holding fields.

1.2 MAGNETOMETRY IN SMALL MAGNETIC FIELDS

The first magnetometer that could measure the absolute value of a magnetic field was published by Carl Friedrich Gauss in 1833 [25]. It was based on a magnetic probe attached to a torsion pendulum and thus already measured the magnetic field using a frequency measurement. While large magnetic fields can be measured via their force on magnetic samples, this becomes difficult for small fields. A first realization of a Josephson Junction [26] paved the way for superconducting quantum interference device (SQUID) magnetometers [27]. Being able to measure small changes in small magnetic fields, SQUID magnetometers made it possible to detect magnetic fields that are created by activity in the human brain in magnetically shielded environments [28].

With laser systems becoming more common, research on atomic vapor magnetometers became more widespread and their sensitivity became compatible with that of SQUID magnetometers [9]. In general, atomic magnetometers measure the time evolution of relative phases between the Zeeman-split magnetic sub-levels in atoms as their splitting is determined by the external magnetic field. If the atomic system is understood well, the splitting is determined by fundamental constants. Consequently, atomic vapor magnetometers are capable of directly measuring the absolute value of the magnetic field without calibration. Atomic magnetometers are discussed in more detail in section 1.2.1.

A high spatial resolution could be achieved using nitrogen-vacancy (NV) centers in diamonds as probes of the magnetic field that can be operated optically [29]. NV centers are a combination of nitrogen atoms that replace single carbon atoms in diamonds with lattice vacancies that can be excited optically. A high spatial resolution is possible with these probes, as they are fixed in the diamond lattices. Recently, NV magnetometry was improved significantly by placing the diamond with the NV centers into an optical cavity to enhance the absorption of the readout light [30].

1.2.1 ATOMIC VAPOR MAGNETOMETERS

Optical hyper-polarization and optical probing of atomic spin states [31–33] are the foundations that made optical magnetometry with atomic vapor possible. An ensemble of particles is called hyper-polarized when the polarization is increased above the equilibrium polarization caused by an external magnetic field. To optically polarize an ensemble of atoms, a selected transition is driven with a high rate. To keep the atoms precessing instead of just achieving a stationary polarization, either alternating magnetic fields are used [34], or the polarizing light beam is modulated in power, frequency, or polarization.

An experimentally very mature technique is magnetometry with alkali vapors [35]. One reason for this is that the wavelengths that are needed to optically drive the transitions needed to hyper-polarize and read out the alkali vapor have been conveniently

available with tunable diode lasers since decades. Also, the large gyromagnetic ratio of the atoms in the ground state makes them sensitive probes of the magnetic field. This has, however, a downside as well, as the unpaired electron makes the atoms chemically rather reactive and prone to depolarization in collisions with other atoms or the walls of the vapor cell.

Atoms that do not have unpaired electrons in the ground state but have a nonzero nuclear spin, like noble gases or mercury, are much less reactive. Also, the spin polarization of the nucleus is protected by the electron shell against spin-exchange due to collisions. However, as the gyromagnetic ratio of a nuclear spin is about three orders of magnitude smaller than that caused by an electronic spin, the precession of these atoms in the ground state is much slower which is a disadvantage in terms of accuracy of a field measurement. On the other hand, if the ultimate goal is to measure a potential effect on the precession frequency that is not caused by the magnetic field, a slower magnetic precession becomes an advantage instead. Furthermore, long relaxation times of the precessing polarization (in the order of hours [36]) in noble gas magnetometers make long coherent integration times of the magnetic field measurement possible and can make up for the slower spin precession when slow changes of the magnetic field are measured.

A difficulty of using closed-shell atoms in otpical magnetometry is that the wavelengths that are needed to drive the magnetometer are typically in the deep-UV range and technically challenging to produce. However, for mercury magnetometers there are now commercially available laser sources. Such a system is described in section 2.2.1. To hyperpolarize helium and xenon, Spin-Exchange Optical Pumping (SEOP), a technique to use alkali atoms to transfer polarization to helium and xenon nuclei, has been used [37]. Furthermore, using two-photon transitions to directly polarize xenon is being investigated [38]. Here, two photons drive the transitions together so that each of them needs only half of the total energy.

In general, atomic vapor magnetometers measure the total magnetic fields (scalar magnetometers) while SQUID magnetometers always measure the projection of the magnetic field onto the axis that is perpendicular to the pick-up loop (vector magnetometer). However, atomic vapor magnetometers can also be turned into vector magnetometers by applying small magnetic bias fields with a well known direction [39]. As using bias magnetic fields can be problematic if the magnetic field is small and should not be affected by the measurement, a vector magnetometer has been realized using the light shift effect (see section 1.3.1) instead of a real magnetic field [40]. The light shift effects only the atoms inside the vapor cell and does not alter the magnetic field in the experiment.

1.3 PROPERTIES OF MERCURY

Understanding atomic physics and spectra has been supported by and tested in experiments using mercury and especially the ${}^1S_0 \rightarrow {}^3P_1$ transition throughout the last century. A high vapor pressure (0.171 Pa at 293.15 K [41]) made it a practical probe in early atomic physics experiments like the Franck-Hertz experiment [42]. In the past years, mercury has become important as a probe for low-energy physics. Atomic lattice-clock experiments have used the ${}^1S_0 \rightarrow {}^3P_1$ transition to laser-cool the atoms [43, 44]. Fundamental symmetries have been tested directly in a mercury EDM experiment [45], where the atomic vapor is polarized and the polarization is monitored using dichroic rotation of linearly polarized light. In addition to the search for atomic EDMs, mercury is also used as a probe for magnetic fields in neutron-EDM experiments [46].

Naturally occurring mercury is a mixture of seven isotopes (see table 1.3.1) with only two of those having an odd number of neutrons (^{199}Hg with $I = \frac{1}{2}$ and ^{201}Hg with $I = \frac{3}{2}$). As they have a nonzero nuclear spin, the excited state ${}^3P_1$ is split into the hyperfine states with $F \in \left\{\frac{1}{2}, \frac{3}{2}\right\}$ for ^{199}Hg, and $F \in \left\{\frac{1}{2}, \frac{3}{2}, \frac{5}{2}\right\}$ for ^{201}Hg. The hyperfine spectra of the natural abundant isotopes are discussed in more detail in section 2.3.1.3. Figure 1.3.1a shows the relative shifts of all natural abundant isotopes and their commonness of occurrence. In 1.3.1b, a transmission spectrum is shown that is recorded with the spectroscopy setup described in 2.2. Comparing these pictures can be used as a first verification to make sure that natural mercury is observed in the process of building a spectroscopy setup.

The outermost electronic shell in mercury atoms has two electrons. While mercury is more reactive than noble gasses with closed shells, the two species have in common that there is no unpaired electronic spin in the ground state. The magnetic moment of a mercury atom in the ground state is thus dominated by the nucleus. While chemical reactions of mercury atoms in the ground state are usually not a problem in vapor mag-

isotope	mass	abundance	spin	mag. moment
^{196}Hg	195.965807	0.15 %	0	0
^{198}Hg	197.966743	10.1 %	0	0
^{199}Hg	198.968254	17.0 %	$\frac{1}{2}$	+0.5059
^{200}Hg	199.968300	23.1 %	0	0
^{201}Hg	200.970277	13.2 %	$\frac{3}{2}$	−0.5602
^{202}Hg	201.970617	29.65 %	0	0
^{204}Hg	203.973467	6.85 %	0	0

Table 1.3.1: Isotopes and hyperfine structure of mercury. Taken from [47].

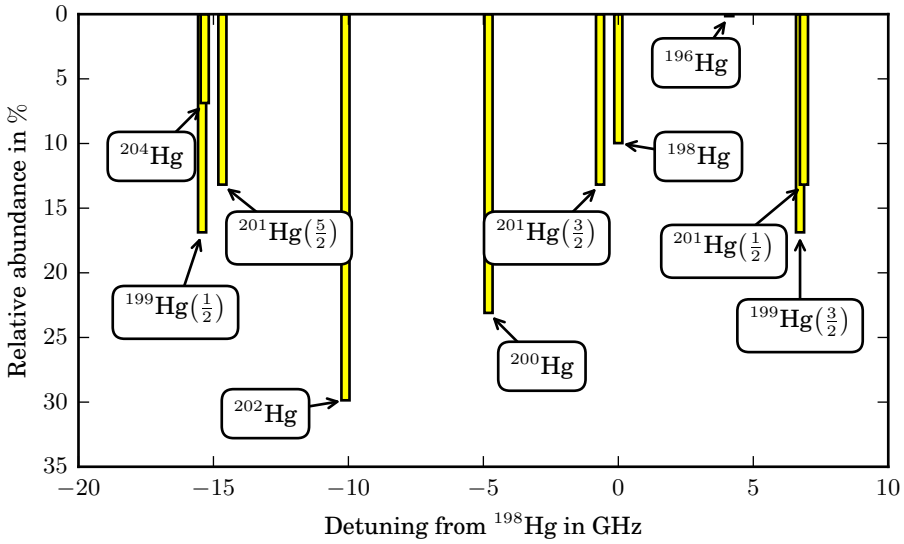

(a) Frequency difference between the hyperfine transitions of all naturally occurring isotopes to the ^{198}Hg transition. The length of the bar represents the abundance of the isotope. The fractional numbers in parentheses denote the quantum number F in the excited state of the transition.

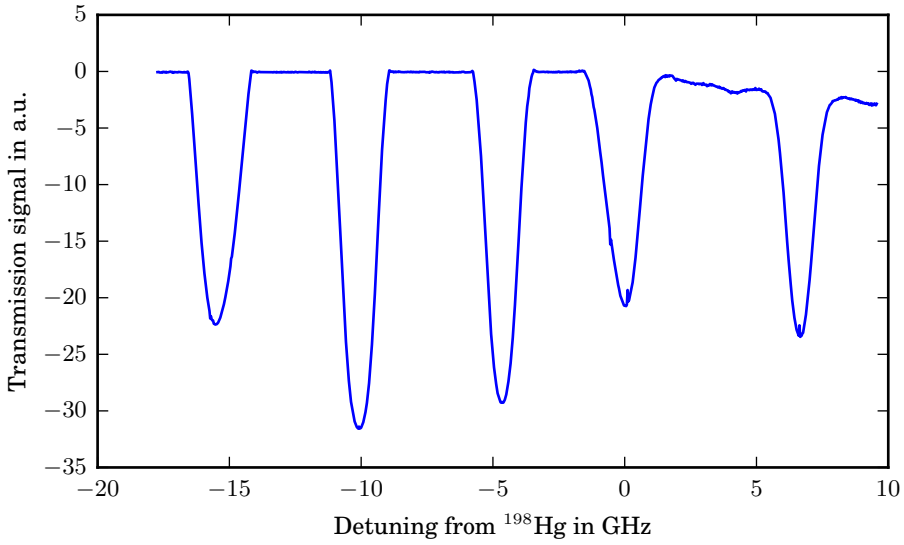

(b) Transmission of a laser beam through mercury vapor. In accordance with figure 1.3.1a, five Doppler-broadened features are observed.

Figure 1.3.1

netometry, the excited state is much more reactive. Implications of the lack of chemical inertness of mercury for magnetometer applications are discussed in section 2.2.3.

In the transition ${}^1S_0 \rightarrow {}^3P_1$, the spin quantum number changes from 0 to 1. Without spin-orbit coupling, transitions with $\Delta S \neq 0$ are forbidden. However, due to a non-negligible spin-orbit coupling in mercury, the ${}^1S_0 \rightarrow {}^3P_1$ transition has a strong amplitude with a lifetime of 119 ns [48]. An instructive discussion of this spin-orbit coupling can be found in [43].

1.3.1 INTERACTION WITH LIGHT

Near resonant light interacts with mercury atoms via virtual and real absorption and emission processes. While in a real absorption, the photon disappears and the atom is excited, the virtual absorption- and re-emission process leads to an effective shift of the atomic energy levels that are involved.

A semi-classical description of the interaction is given in [49]. The laser beam is assumed to have a low intensity and its electric field is represented by a quasi-monochromatic wave. Magnetic fields are assumed to be small in order to keep Zeeman shifts negligible compared to the Doppler broadening. The light wave is seen as a small perturbation of the ground state Hamiltonian adding a shift δE and an absorption $\delta\Gamma$. As the total angular momentum of the ground state is given by $I = \frac{1}{2}$ for ^{199}Hg, the shift and the absorption can have a scalar and an alignment-dependent vector component.

$$\delta E = \delta E_0 + \vec{\mu} \cdot \delta \vec{E}_1$$
$$\delta\Gamma = \delta\Gamma_0 + \vec{\mu} \cdot \delta\vec{\Gamma}_1$$

Figure 1.3.2 shows the absorptivity as derived in [49]. The scalar absorptivity (black dots) is different for the transitions to the hyperfine states with F=1/2 and F=3/2. The vector absorptivity depends on the alignment of the atoms spin and the polarization of the incident light. It reverses its sign on reversal of the relative alignment. As the total absorptivity is the sum of the two, a strong dependence of the total absorption of light that is on resonance with the F=1/2 transition is obvious as the total absorption is zero for parallel atomic and photonic angular momenta. That makes sense as the ground state and the excited state in this transition both have the total angular momentum quantum number F=1/2. Due to conservation of the total angular momentum, when a photon (carrying the angular momentum $\hbar$) is absorbed, the atomic angular momentum of $1/2\hbar$ has to be reversed.

As the scalar light shift is the same for both Zeeman states of the atoms in the ground state and is small compared to the ${}^1S_0 \rightarrow {}^3P_1$ transition, it is not of interest for magnetometer applications.

For the vector light shift, it was shown in [49] and [50] that for ^{199}Hg with $I = F = \frac{1}{2}$ in the ground state, a circularly polarized light beam has the same effect on the atoms as a magnetic field parallel to the k-vektor of the beam. This pseudo magnetic field corresponds to a B-field of the strength (IV.17 in [49])

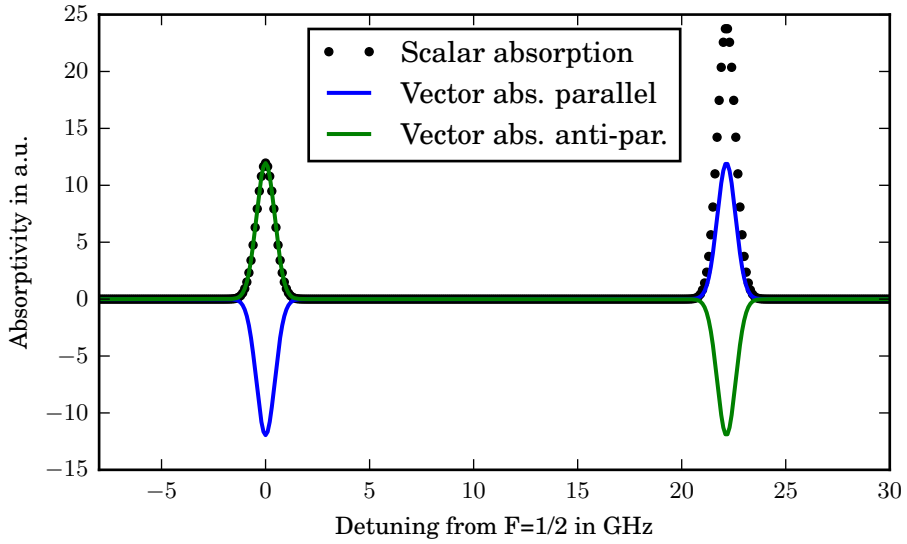

Figure 1.3.2: Scalar- and vector absorptivity for different alignments. The blue line shows the vector absorptivity when the circular polarization vector is parallel to the atomic polarization, and the green line shows the absorptivity when the two are anti-parallel. The scalar absorptivity is shown in black dots. It is independent of the relative alignment. The total absorption is proportional to the sum of the vector- and the scalar- absorptivity. This leads to a strong dependence of the total absorptivity on the alignment.

$$B_{\mathrm{VLS}} = \frac{I_0 \lambda^2 e^2 f_{eg}}{48 \gamma_{\mathrm{Hg}} \pi m_e c^2} \sqrt{\frac{M}{2RT}} (2F_e+1)\left(\frac{11}{4} - F_e(F_e+1)\right) \cdot \mathrm{Re}\left[Z\left(\frac{\sqrt{\ln(2)}}{\Delta \nu_D} (2(\nu - \nu_{\mathrm{eg}}) + i\Gamma) \right) \right] \begin{cases} -1 & \text{for } \sigma^- \\ 1 & \text{for } \sigma^+ \end{cases} \tag{1.3.1}$$

with light of the intensity I_0, the wavelength λ and the detuning from the resonance frequency $(\nu - \nu_{\mathrm{eg}})$, with the elementary charge e, the oscillator strength of the transition $f_{eg} = 0.0243$ [48][51], the electron mass m_e, the speed of light c, the molar mass of ^{199}Hg M, the gas constant R, the temperature T, and the natural linewidth Γ. F_e is F of the excited state and $\Delta \nu_D = \frac{2}{\lambda}\sqrt{\frac{2\ln(2)RT}{M}}$ is the Doppler-width of the transition. The plasma dispersion function Z is given by

$$Z(x) = \frac{1}{\sqrt{\pi}} \int_{-\infty}^{\infty} \frac{e^{-u^2}}{u - x} du. \tag{1.3.2}$$

A typical pseudo magnetic field caused by the vector light shift effect in a mercury magnetometer with low vapor pressure is shown in figure 1.3.3. Implications of this for magnetometry are discussed in section 3.3.1.

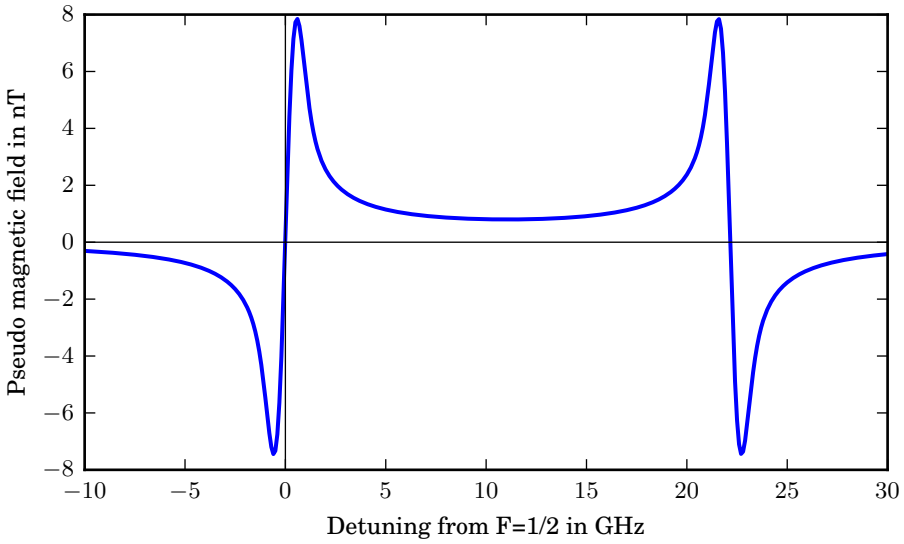

Figure 1.3.3: Pseudo magnetic field caused by a weak laser beam in a typical magnetometer setup with low vapor pressure. Details on how this affects the magnetic field measurement are discussed in 3.3.1.

1.3.2 MERCURY IN CONSTANT MAGNETIC AND ELECTRIC FIELDS

1.3.2.1 *Constant magnetic field*

When a magnetic field is applied to a mercury atom, the levels are shifted by the Zeeman effect. In sufficiently small magnetic fields, where the shifts due to the magnetic fields are small compared to other energy differences, the Zeeman effect is linear and can be written [52]

$$\Delta E_{m_F} = -(\mu_F)\cdot B = g_F \cdot \mu_B \cdot B \cdot m_F, \tag{1.3.3}$$

with

$$g_F = g_J \frac{F(F+1)+J(J+1)-I(I+1)}{2F(F+1)} - g_I \frac{\mu_N}{\mu_B} \frac{F(F+1)+I(I+1)-J(J+1)}{2F(F+1)}. \tag{1.3.4}$$

When a two-level system is prepared accordingly (see section 3.2.1), this energy difference between the Zeeman states leads to a precession with the Larmor frequency $\omega_L = \gamma B$.

In the ground state, only g_I contributes to the gyromagnetic ratio γ and for ^{199}Hg in the ground state $^1S_0$ the gyromagnetic ratio was measured to be $7.590\,115\,2(62)$ MHz T^{-1} [53].

The g-factors of all $^3P_1$ hyperfine states calculated with equation 1.3.4 and neglecting the nuclear contribution are given in table 1.3.2 for the naturally abundant isotopes. g_J was measured in [54] to be $1.48631(8)$.

J	F	g
1	0.5	1.98175
1	1.5	0.990873

(a) g-factors of ^{199}Hg hyperfine states

J	F	g
1	0.5	-0.990873
1	1.5	0.396349
1	2.5	0.594524

(b) g-factors of ^{201}Hg hyperfine states

J	F	g
1	1	1.48631

(c) g-factors of the even isotopes

Table 1.3.2: g-factors of the excited states in odd and even mercury isotopes calculated with [54].

1.3.2.2 *Constant electric field*

In constant electric fields, atoms can be statically polarized depending on their electronic structure. As long as the Stark shift is a small distortion to the Zeeman spectrum, the resulting energy shift of the Zeeman sublevels when the hyperfine structure is not negligible, can be described by a scalar term α_0 and a tensor component α_2 [55]:

$$\Delta E_m = -\tfrac{1}{2}\varepsilon^2\alpha_0 - \alpha_2(3\varepsilon_z^2-\varepsilon^2)\cdot Y \tag{1.3.5}$$

with ε_z beeing the projection of the electric field ε on the magnetic field.

The distinctiveness of the hyperfine and Zeeman states can be found in

$$Y = \frac{[3m_F^2 - F(F+1)]\cdot[3X\cdot(X-1) - 4F\cdot(F+1)\cdot J\cdot(J+1)]}{(2F+3)\cdot(2F+2)\cdot 2F\cdot(2F-1)\cdot 2J\cdot(2J-1)} \tag{1.3.6}$$

with $X = F(F+1)+J(J+1)-I(I+1)$. For the transition $^1S_0 \rightarrow {}^3P_1$, $F = \frac{1}{2}$ in ^{199}Hg (magnetometer transition), the tensor polarizability is thus always zero.

The differential shift $\Delta E(6^3P_1) - \Delta E(6^1P_0)$ of the levels that are involved in the magnetometer transition was measured in [56] to be $-3.32 \pm 0.06\,\mathrm{kHz/(kV/cm)^2}$. For both of these levels, there is no tensor Stark shift to first order as $Y = 0$, effectively making this transition eligible to measure α_0. It was the first measurement that used a laser to measure Stark constants in mercury. A moving mirror in the beam path provided a well defined frequency shift to determine the slope of the transmission signal at an appropriate point in a Doppler-broadened signal. The Stark shift was then extracted from monitoring the transmission at this point while switching on and off the electric field. Isotopically purified ^{199}Hg was used to reduce the influence of the other hyperfine transitions on the transmission signal. However, the transition to the $F = \frac{3}{2}$ hyper-

J	F	mF	Tensor Stark shift in $\frac{\text{kHz}}{(\text{kV/cm})^2}$
0	0.5	-0.5	0
0	0.5	0.5	0
1	0.5	-0.5	0
1	0.5	0.5	0
1	1.5	-1.5	-0.3945
1	1.5	-0.5	0.3945
1	1.5	0.5	0.3945
1	1.5	1.5	-0.3945

Table 1.3.3: Tensor Stark shifts of ^{199}Hg states for perpendicular electric and magnetic fields

fine state in ^{199}Hg cannot be avoided and its influence on the transmission signal had to be estimated. In chapter 2.5.3, an experiment is shown that resolves Stark shifts of the different hyperfine transitions without Doppler broadening. Besides allowing to completely separate the shifts of the hyperfine transitions from each other, no isotopically enriched mercury is needed.

Tables 1.3.3, 1.3.4, and 1.3.5 show the calculated tensor Stark shift for the naturally occurring isotopes and their hyperfine states when the electric field is parallel to the magnetic field. The angle β between the magnetic and the electric field scales the resulting tensor Stark shift with a factor between 2 and -1. In terms ob β, the total Stark shift can be written:

$$\Delta E_{\text{stark}} = \varepsilon^2[-\frac{1}{2}\Delta\alpha_0 - \Delta\alpha_2(2-3\cdot\sin^2(\beta))\cdot Y] \tag{1.3.7}$$

The tensor Stark shift constant α_2 has been measured by [57] to be (1.578 ± 0.016) kHz$/(\text{kV/cm})^2$ using a resonance lamp and level crossing spectroscopy.

As the tensor Stark shift is zero for the ground state of ^{199}Hg and the scalar Stark shift is the same for both magnetic sub-levels, the energy splitting and thus the precession frequency are not directly affected by a constant electric field. However, a combination of the light shift and the Stark shift can cause a shift of the precession frequency. This is discussed in detail in section 3.3.4.1.

J	F	mF	Tensor Stark shift in $\frac{\text{kHz}}{(\text{kV/cm})^2}$
0	1.5	-1.5	0
0	1.5	-0.5	0
0	1.5	0.5	0
0	1.5	1.5	0
1	0.5	-0.5	0
1	0.5	0.5	0
1	1.5	-1.5	0.3156
1	1.5	-0.5	-0.3156
1	1.5	0.5	-0.3156
1	1.5	1.5	0.3156
1	2.5	-2.5	-0.3945
1	2.5	-1.5	0.0789
1	2.5	-0.5	0.3156
1	2.5	0.5	0.3156
1	2.5	1.5	0.0789
1	2.5	2.5	-0.3945

Table 1.3.4: Tensor Stark shifts of ^{201}Hg states for perpendicular electric and magnetic fields

J	F	mF	Tensor Stark shift in $\frac{\text{kHz}}{(\text{kV/cm})^2}$
0	0	0	0
1	1	-1	-0.3945
1	1	0	0.789
1	1	1	-0.3945

Table 1.3.5: Tensor Stark shifts of ^{198}Hg states for perpendicular electric and magnetic fields. This is the same for all isotopes with an even number of nucleons.

1.4 EDM EXPERIMENTS AND MERCURY

Any permanent electric dipole moment that is associated with a spin would violate Time invariance (T) and Charge-Parity invariance (CP) symmetry if it was not zero (see [22]). CP symmetry is violated, when a system is is not invariant when a C- (charge) and a P- (parity) inversion is applied to the system .

The SM does not rule out the possibility of CP violation in general and CP symmetry can also be violated in the SM directly via a nonzero parameter $\bar{\theta}$ in the strong interaction [58]. In weak interaction, a small CP violating phase in the Cabibbo-Kobayashi-Maskawa (CKM) matrix was found already and is included in the SM [59, 60]. However, a larger CP violation would help to explain cosmological observations. For example, no mechanism has been found that can describe the observed dominance of matter over antimatter in the universe [61] with the small CP violation that has been found so far. Sakharov proposed a mechanism that could explain why more baryons than anti-baryons are observed [62]. However, his model needs a mechanism to violate CP symmetry to a larger extent than can be explained by the SM. EDMs would point towards such a CP violating mechanism (see, for example, [22]). If EDMs are found at values that are larger than the SM predictions, they could be caused by the $\bar{\theta}$ term or by BSM physics [63].

To cover different possible sources for CP violation, it is essential to search for EDMs in different systems. As quarks can not be observed individually, the smallest systems that are sensitive to CP violating effects in the quark sector are free protons and neutrons. The need for strong electric fields in EDM experiments makes measurements with charged particles challenging [64]. Consequently, the most precise measurements of isolated hadrons so far were done with ultra-cold neutrons (UCNs). UCNs are free neutrons that are cooled down to velocities below $\sim 8\,\mathrm{m\,s^{-1}}$, leaving them with a kinetic energy that is lower than the fermi potential of most materials. UCNs are thus reflected in wall collisions with any angle of incidence and can be stored in chambers. Cooling free neutrons down to these energies is either done with a Doppler shifting turbine [65] or with superthermal cryogenic converters with super-fluid helium [66] or solid deuterium [67].

Atoms, being composed of nuclei and electrons are sensitive to different interactions. They are especially eligible as probes for electronic EDMs if their ground state has a nonzero electronic spin . Atoms that do not have an electronic spin in the ground state but a non-zero nuclear spin can be used in the search for EDMs in compound systems of nucleons. However, the impact of their electronic shell still has to be considered when interpreting a potential nuclear EDM [68]. Besides in electrons that are bound in atoms, electron EDMs are also searched for in free electrons and in molecules. As large

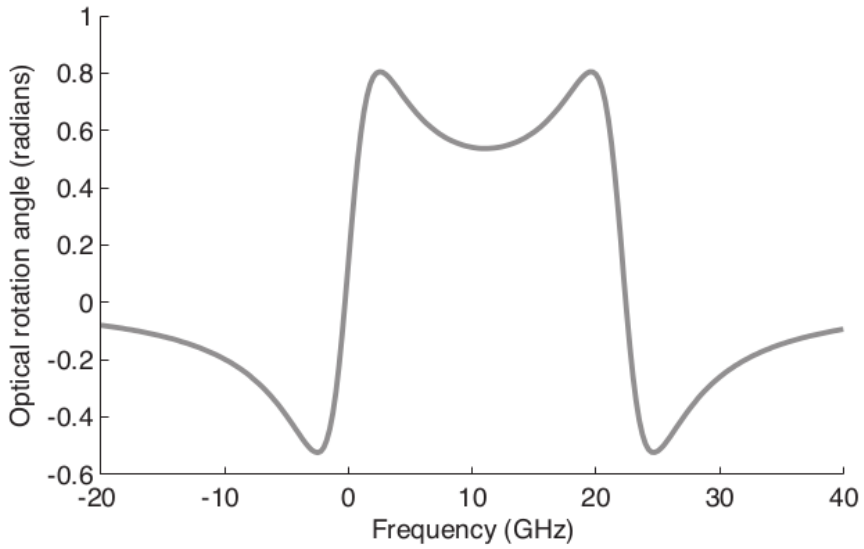

Figure 1.4.1: Rotation angle of linear polarization axis of light traversing polarized ^{199}Hg vapor. Taken from [70].

internal electric fields can be achieved in polar molecules, the best limit on electron EDMs to date is set using the molecule thorium monoxide [69].

The element mercury has a special role in the history of EDM-searches. A direct search for a possible EDM in the isotope ^{199}Hg, which has no unpaired electronic spin in the ground state but a non-zero nuclear spin of $1/2\hbar$, set the currently best upper limit for atomic EDMs of 7.4×10^{-30} e cm (95% C.L.) [15]. Furthermore, ^{199}Hg has been used as a magnetometer to cancel magnetic field fluctuations in nEDM experiments.

1.4.1 MERCURY EDM

In the mercury EDM experiment having set the best upper limit so far [15], a small cell is used with a high mercury vapor pressure. This makes it possible to achieve a high statistical accuracy while not being sensitive to spatially large inhomogeneities of the magnetic field. A buffer gas reduces the wall collisions and quenches the excited atoms in order to enhance the polarization lifetime. Polarization of the vapor is achieved with transverse optical pumping as described in section 3.2.1. For this, the laser wavelength is tuned to the point to the left of the $^1S_0 \rightarrow {}^3P_1$ transition with F=1/2 in the excited state where the light-shift is zero. To detect the precession, the laser is tuned to a wavelength between the F=1/2 and F=3/2 transition, attenuated, and it's polarization is switched from circular to linear. [49] provides analytical results for the rotation of a linearly polarized laser beam when it passes through polarized mercury

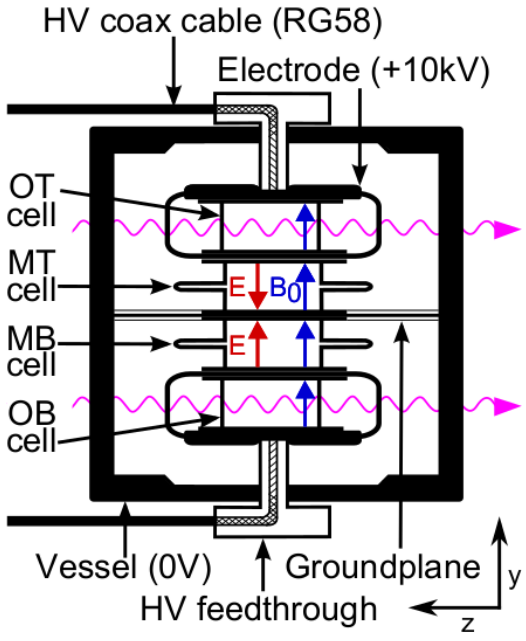

Figure 1.4.2: Cell stack in the mercury EDM experiment [15]. The cells in the middle (MT+MB) are inside the electric field, while the outer cells (OT+OB) are not. All four cells are operated with laser beams but the beams in the center cells point in x-direction and are not shown here. This graphic is taken from [15]

vapor which are shown in figure 1.4.1. The laser is set to the frequency in the middle between the two transitions as the rotation is not zero and the slope is zero as well for the for the rotation as for the light shift curve.

To account for fluctuations of the magnetic field in the experiment, four cells are used as shown in figure 1.4.2. Only the atoms in the two cells in the middle are exposed to large electric fields. With the ground electrode being placed between the two center cells, the electric fields in these two cells have the opposite sign. The outer two cells are used as pure magnetometers that are not affected by the electric field.

1.4.2 NEUTRON EDM

As the density achievable with UCNs is lower than the density achievable with mercury vapor, storage cells in nEDM experiments have to be larger to obtain a high statistical accuracy. So far, nEDM experiments used one precession cell in which the magnetic and the electric field could both be reversed independently [21, 71]. Precession frequencies were then measured in different field combinations and the average difference between the precession frequency in parallel and anti-parallel magnetic and electric fields was extracted.

As any statistical fluctuation of the magnetic field between the measurements with different field configurations causes a statistical uncertainty, the first order correction for this is to monitor the magnetic field with an independent magnetometer.

While with external magnetometers, the magnetic field in the nEDM chamber during a precession period can be reconstructed to an extent that depends on the number of magnetometers and the solid angle they cover around the neutron precession chamber, a co-habitating magnetometer (co-magnetometer) measures the magnetic field inside the neutron precession chamber directly. For this, mercury vapor was added to the neutron precession chamber and the magnetic field was measured averaging over almost the same volume[1] and the same time. More details on the introduction of mercury co-magnetometry in nEDM experiments are given in chapter 3.1.

In next-generation nEDM experiments, a similar setup as in the mercury EDM experiment [15] is planned. In two stacked cells, the neutrons experience opposite electric fields in the same magnetic holding field as shown in figure 1.4.3. The leading uncertainty is then the drift of the magnetic field gradient. Now, the first order correction is to place magnetometers above and below the stack of UCN cells, to monitor the drift of the gradient.

1.4.2.1 *Mercury (co-)magnetometry*

The elements that can be used for co-magnetometry in an nEDM experiment are restricted compared to those available for pure magnetometry. As polarizing helium and xenon still needs SEOP, it is technically difficult to polarize these gases in an nEDM precession chamber. Also, magnetometers using helium or xenon are usually read out with secondary magnetometers which measure the rotating magnetic field created by high-density polarized noble gas vapor. Adding a high density atomic gas to the chamber causes a macroscopic rotating magnetic field not only outside but also inside the cell if the it is not a perfect sphere [73] and would be adverse for the UCNs measurement. However, as mentioned above, two photon transitions in xenon are being investigated and could make pure optical magnetometry with xenon possible in future as described in section 2.2.1 and [38].

With mercury, a high polarization can be achieved with optical pumping in the same way as in the mercury EDM experiment. As no buffer gas can be used without impeding the UCN measurement, the lines in all of the interactions with the atoms are not significantly pressure-broadened in contrast to the lines in the mercury EDM experiment. This leads to the rotation angle of linearly polarized light at the wavelength that is used in the mercury EDM experiment for the readout to be almost zero. Instead of measuring the rotation of linearly polarized light, the transmission of circularly polarized light is used to monitor the precession. However, with circular polarized light on

1 The mercury atoms measure the averaged magnetic field of not exactly but almost the same volume as the UCNs do, as the center of gravity of the UCNs is below the one of the mercury atoms due to gravity having a noticeable impact on the low-energy UCNs.

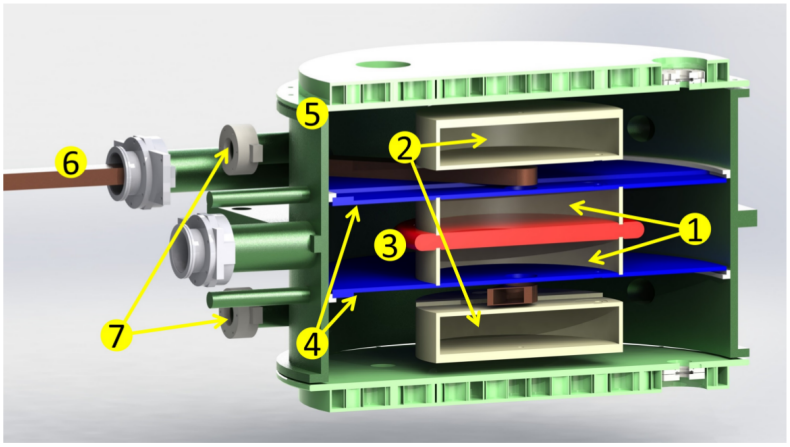

Figure 1.4.3: Cut through a drawing of the cell stack and the vacuum chamber (5) of a next generation nEDM experiment. The cells in the middle (1) are subject to the electric field created by the high voltage electrode (3) and the ground electrodes (4). Here, the UCNs measurement takes place and mercury vapor can be added. The outer cells (2) can be used as mercury vapor magnetometers. Additional magnetometers can be placed close to the precession chambers by using tubes (7) that are traversing the vaccum chamber close to the precession cells. The neutrons are guided into the chambers via (6). Taken from [72].

resonance, the light-shift effect can cause problems at that wavelength, as described in section 3.3.1.

In [24], mercury vapor lamps have been used to polarize and monitor the mercury atoms. However, as convenient lasers at 253.7 nm became commercially available, it makes sense to switch to lasers. While the lamps have a broad spectral width in the order of ~GHz that can barely be manipulated, the lasers spectral width is below 1 MHz and the center wavelength can be chosen freely from a broader range. For more details on the laser source, see section 2.2.1. Naturally, a laser beam diameter is smaller than the diameter of a beam created by a vapor lamp. As the noise of measuring the projection of N_a spins in one light beam is proportional to $\frac{1}{\sqrt{N_a}}$ and the number of atoms in the light beam with the radius r is proportional to r^2, the noise is proportional to $\frac{1}{r}$. However the laser beam can easily be widened until the combination of vibrations and clipping of the beam dominate the noise figure (see section 3.4.2). Being able to tune the laser wavelength principally allows a lightshift-free operation, although this is technically challenging. Issues that have to be addressed to avoid the uncertainties of the results to be dominated by uncertainties that are caused by the light-shift effect are discussed in chapter 3.3. In section 3.4.1, a frequency stabilization for the a laser is shown. It uses the isotope shift measurement presented in section 2.5.2 and a spectroscopy setup as reference.

1.4.2.1.1 *Magnetometry vs. co-magnetometry*

Both strategies, using mercury vapor in the same chambers ((1) in 1.4.3) as the UCNs (co-magnetometer) and adding mercury vapor magnetometers outside the nEDM precession chambers ((2) in 1.4.3), have advantages and disadvantages. In a dual chamber

nEDM experiment, the leading error caused by magnetic field inhomogeneities is the drift of the magnetic field gradient. When one magnetometer cell is added above the nEDM cell stack and one below the stack, the gradient can be monitored. Higher order perturbations and especially magnetic sources that are close to the cell stack can not be corrected appropriately. If there are local magnetic inhomogeneities close to one of the magnetometers, this would lead to a false analysis of the gradient. The great advantage of a co-magnetometer is that it measures the average magnetic field in nearly the same volume (except for the small vertical offset due to gravity as discussed above).

However, a co-magnetometer has disadvantages as well. The wall coating of the precession chamber has to be optimized for both species instead of just for UCNs [74]. Also, with mercury vapor, the chamber can become less robust against high voltage discharges. Furthermore, the mercury vapor density has to be small in order to reduce the impact on the neutrons. This means that instead of the frequency-detuned linear readout scheme, which is used in the mercury electric dipole moment (HgEDM) experiment, an absorptive readout has to be used. As in the co-magnetometer configuration the mercury atoms are subject to the electric field, the DC Stark shift has to be minded as well. Systematic effects in the two different types of magnetometers are discussed in more detail in section 3.3.8.

While all of these problems can be avoided by not using a co-magnetometer and using magnetometers above and below the nEDM cell stack, this approach being limited by the stability of higher order components of the magnetic field is a physical constraint that can not be addressed by improving magnetometric techniques. Moreover, mercury co-magnetometry has already proven successful in [24]. Further improvement of mercury co-magnetometry is thus worth striving for.

This thesis discusses systematic effects and uncertainties that will be relevant for experiments trying to search for smaller EDMs than have been excluded so far and shows how the uncertainties can be reduced and the impacts of these effects in an nEDM experiment with a mercury co-magnetometer are discussed. A magnetometer system was built and optimized for operation as co-magnetometer. It can however also be used as a pure magnetometer as shown in section 3.5. This system and systematic effects in a co-magnetometer are described in part 3. Part 2 presents a Doppler-free spectroscopy setup. This setup was crucial to improve the accuracy of setting the laser-wavelength. Doing this is important as the light-shift can cause systematic effects as described in section 3.3.1.

Part 2

SPECTROSCOPY

2.1

SPECTROSCOPY FOR ATOMIC MAGNETOMETRY

Spectroscopy is an important tool for atomic magnetometry, primarily because of the light-shift effect (see section 1.3.1). The dependence of the Larmor frequency shift caused by near resonant light on its detuning from resonance imposes the need to control the laser frequency with a better accuracy then a conventional wavelengthmeter could do. Missing the optimal wavelength in the readout beam by just 10 MHz in experimental conditions given in table 3.3.1, can cause a shift in the magnetic field measurement of 2.45 fT (see section 3.3.1). Atomic spectroscopy can provide accurate and absolute information on the laser frequency when it uses the same atomic transition as the atomic magnetometer. This is used in section 3.4.1 to control the frequency of the laser light.

Furthermore, spectroscopy is used to measure the influence of experimental parameters on atomic transitions. Section 2.5.3 shows a measurement of the influence of electric fields, which are typically high in EDM experiments, on the magnetometer transition.

The frequency resolution of atomic spectroscopy is limited by the signal-to-noise ratio (SNR) of the spectroscopic signal and the width of the features that are recorded. While the noise of the spectroscopic signal is mainly limited by the quality of the readout electronics, width and height of the features depend on the spectroscopic methods that are used.

Measuring the absorption by mercury vapor as a function of the laser light frequency, produces a Doppler-broadened absorption spectrum as shown in figure 1.3.1b. The width of these features is large enough that some of the hyperfine transitions can not be resolved as they are too close to each other. Spectroscopic techniques that suppress the Doppler shift and hence the Doppler broadening are described in chapter 2.3.

2.2

SPECTROSCOPY SETUP

2.2.1 LASER SOURCE

To drive the $^1S_0 \rightarrow {}^3P_1$ transition in mercury, light with a wavelength of 253.7 nm is produced by a laser system that uses two frequency doubling crystals.[1] A Master oscillator with a mode-hop free tuning range of >20 GHz produces a fundamental laser light with a wavelength of 1014.8 nm which is amplified by a tapered amplifier. The amplified laser beam is then passed to two successive ring resonators housing frequency doubling crystals.

For precise control of the laser frequency, the laser diode is housed in an external reflection grating that acts as a resonator. As this external resonator is much longer than the internal resonator of the laser diode (cm instead of µm), the width of the emitted laser light is reduced to ≤1 MHz. A piezo actuator is mounted to the grating and can simultaneously change the grating profile and the length of the external resonator, providing a convenient mechanism to manipulate the laser wavelength. This is used in section 3.4.1 to stabilize the laser frequency in mercury precession experiments and to scan the laser frequency in spectroscopic measurements. To suppress mode hops, a feed forward feature simultaneously changes the current in the laser diode, which has an effect on the length of the internal resonator of the laser diode.

However, the Feed Forward feature also effects the power of the laser beam. To keep the laser power constant without affecting the wavelength or mode hop stability, a second control loop is necessary. Section 3.4.3 describes the stabilization of the laser power by manipulating the current that is applied to the tapered amplifier.

In an effort to observe the $^1S_0 \rightarrow {}^2\left[\frac{5}{2}\right]_2$ two-photon transition in xenon, for which the light needs to have a wavelength of 256 nm [38], it was tested whether the mercury laser system is capable of generating this wavelength as well. By detuning the wavelength of the seed laser and realigning the laser beam at every stage of the laser system, an output power of ≈1 mW at 256 nm was archieved. More details on the two photon transition in xenon can be found in [38]. Very long spin polarization lifetimes and chemical inertness make xenon an interesting candidate for atomic magnetometry. If the two photon transition can be driven efficiently, purely optical xenon magnetometers can be realized.

2.2.2 SPECTROSCOPY CELLS

All spectroscopy cells are based on commercially available quartz cells.[2] The body of the cells is completely made from quartz and a glass stem is connected to it via a graded

1 Toptica TA/DL-FHG pro

2 FireflySci, Precision Cells Type 61 Standard Cuvette with Graded Seal Tube

Figure 2.2.1: A first prototype cell for the Stark shift measurement (2.5.3). This cell had a vacuum leak and a second layer of glue was added to improve the vacuum. The cell that was used for the measurement was built with much less glue. The dark spots in the middle are likely to be oxidized mercury.

seal tube. This allows heating the cells out without breaking them due to the different thermal expansion coefficients of quartz and glass.

Anti-reflection coating of the windows is not necessary. To avoid reflections of the pumping and the readout beam to overlap in the spectroscopy setup, it is sufficient to mount the cell tilted by a small angle in order to break the symmetry of the two laser beams.

To seal the low-pressure mercury-vapor inside the cell, protecting it from the external atmosphere, two different approaches were tested. It was found that when a valve, which was melted to the glass stem of the cells in order to be able to hook them to the vaccum pump again, was used to seal the cells, they sometimes degraded over time. A more detailed description of this is given in the following section. However, the cells showed a good performance without degradation due to residual gas when they were fire sealed after heating them in an oven while being connected to the vacuum system.

2.2.3 PHOTO-CHEMICAL EFFECT

In recent years, experiments using mercury vapor and 253.7 nm laser light have reported a formation of dark spots at the point where the laser beam enters the cell through the quartz windows [75] or degradation of polarization lifetimes of the atoms inside the cell coincidental with a decline of ^{199}Hg density in the cell when irradiated with laser light [70]. Heating the cells restored the original state of the cells in either case. Both of these effects were observed in our setup as well.

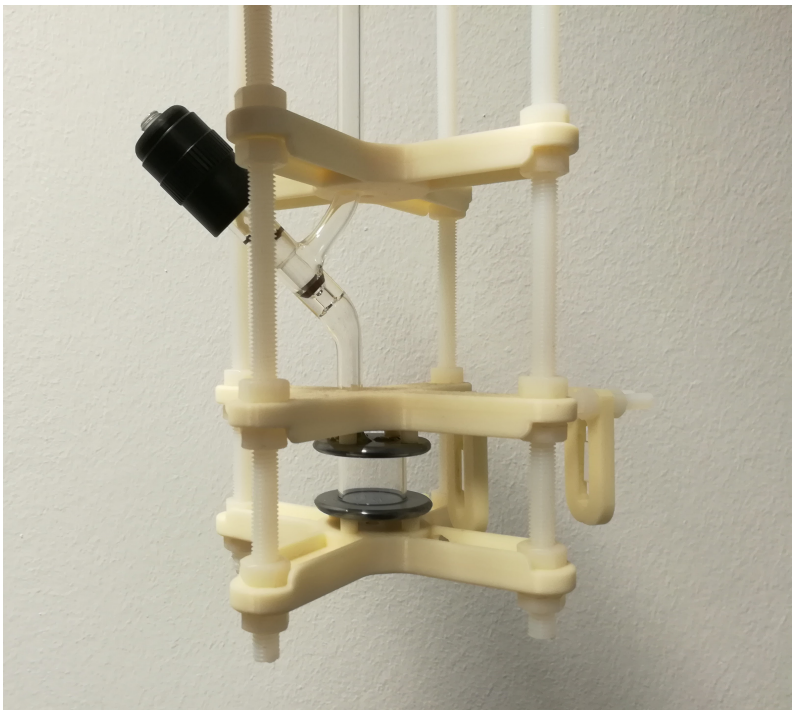

Figure 2.2.2: Small prototype cell in a 3D-printed holding structure to measure spin precession with an electric field. The laser beam traverses the quartz cylinder and is then refocused by two cylindrical lenses. Two silicon wavers (used as electrodes) were glued to the top and the bottom of the cell. One of the wavers had a small hole and a valve was glued to that hole to evacuate the cell and fill in mercury vapor. However, only a depolarization time of a few seconds was achieved in this cell. This was likely caused by residual oxygen inside the cell as described in the text.

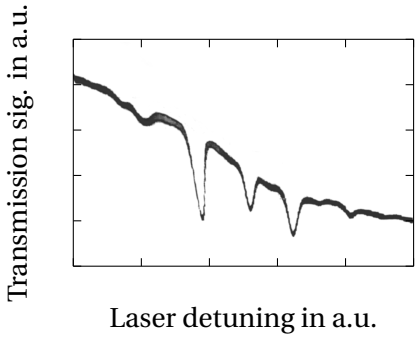

Figure 2.2.3: Doppler-broadened spectroscopy signal recorded in a cell that had been used for precession experiments. The depicted signal is a screenshot from an oscilloscope that was used as a live monitor during the precession experiments. Although the SNR is bad compared to signals that are recorded in the spectroscopy setup, this indicates that the absorption due to ^{199}Hg, ^{204}Hg, and ^{201}Hg is reduced compared to the absorption caused by the other isotopes. These three isotopes are all excited by light that is resonant with the ^{199}Hg, F=1/2 transition, and make up the two outermost features out of five expected. For a full spectrum of mercury with the natural isotopic mixture that was recorded in the spectroscopy setup, see figure 1.3.1b.

In self-made spectroscopy cells, the dark spots sometimes appeared and disturbed the transmission of the laser light. One example of a cell with a bad vacuum is shown in figure 2.2.1. Shifting the cell a bit, so that the laser passed through a clear spot of the quartz glass restored the spectroscopic signals. However, formation of the spots was accompanied by broadening of the Doppler-free signals, indicating a correlation with bad vacuum in the cell. Sometimes to the extent that the Doppler-free signals could not be observed anymore. Like in [75] and [70], the spot could be removed by heating the cell.

Similarly, in a small prototype cell for measuring precession of mercury atoms in magnetic and electric fields (see figure 2.2.2), a degradation of the polarization lifetime was observed as optical pumping and readout light was sent through the cell. At the same time, the absorption of the readout light was reduced.

To investigate this, the laser frequency was scanned over a frequency range that contains the frequencies of the $^1S_0 \rightarrow {}^3P_1$ transition of all isotopes. The x-axis of the oscilloscope was synchronized with the electronics that control the laser frequency scan. Effectively, this turned the precession experiment into a setup able to record Doppler-broadened spectroscopy signals.

Due to the lower cost compared to isotopically purified mercury, this cell contained natural mercury with the natural abundance of all stable isotopes. After the cell had been operated as a magnetometer cell, pumping and reading only the ^{199}Hg transition for precession experiments, the spectrum showed that the abundance of the isotopes had changed (see figure 2.2.3), and there are only spurious amounts of ^{199}Hg and ^{204}Hg left in the cell.

This is a strong indication that these two isotopes were removed from the gas phase selectively by the laser light via chemical reactions of excited atoms, as during the precession experiments the laser light had been locked to ^{199}Hg which is very close to the ^{204}Hg transition. This interpretation is supported by the fact that this only happened in cells that were not sealed by melting the glass stem, but closed with valves, which makes it likely that these cells contain more impurities.

A good candidate for such a reaction is oxidation of the excited mercury atoms. With 1,3-butadien as a reactor, this process was used in [76–79] for isotopic purification.

Using a laser system instead of fluorescence lamps would allow to achieve much better purification of single mercury isotopes as the lamps always excite neighboring hyperfine transitions to some extent due to their spectral width.

Unfortunately, it is not trivial to produce a pure ^{199}Hg cell by simply oxidizing all other isotopes as the Doppler-broadened lines of ^{204}Hg and ^{199}Hg overlap to the extent that they are almost identical. Trying to oxidize ^{204}Hg, one would also oxidize nearly the same amount of ^{199}Hg. As ^{201}Hg overlaps the ^{199}Hg F=1/2 and F=3/2 lines, it is also not possible to extract the ^{199}Hg by selectively oxidizing ^{199}Hg and pumping out the rest. This means that there are at least two steps needed to purify ^{199}Hg. One possible process would be to oxidize ^{201}Hg and ^{199}Hg with light that is resonant with ^{199}Hg (F=1/3) , pumping out the remaining isotopes, and then oxidize the ^{201}Hg via the F=3/2 transition. Then, the purified ^{199}Hg can be pumped out and distilled to a reservoir.

2.3 SPECTROSCOPIC TECHNIQUES

Due to thermal motion of the atoms, the Doppler effect causes a broadening of the intercombination line in the order of GHz as can be seen in figure 1.3.1b. As the natural line width is 1.27 MHz, it is worth to spend some effort to avoid the Doppler broadening.

In general, the spectroscopic methods described below use two anti-parallel beams from the same laser. Because they traverse the atomic vapor in opposite directions, the sign of the Doppler shift experienced by each atom is opposite for the two beams. One beam with a higher power (preparation beam) traverses the mercury vapor in $\vec{z}$-direction and induces a change in the population densities for those atoms having the right velocity in $\vec{z}$ direction ($v_{d,z}$) for the Doppler shift to compensate the detuning of the laser light frequency (ω_l) from the atomic transition (ω_0):

$$v_{d,z} = c \cdot \frac{\omega_l - \omega_0}{\omega_0}.$$

Atoms with a z-velocity larger or smaller than, but close to, $v_{d,z}$ are mainly affected within the width

$$\Delta v_{d,z} = c \cdot \frac{\gamma}{\omega_0}, \tag{2.3.1}$$

where γ is the width of the transition.

A low intensity readout beam with the same frequency traverses the cell in the opposite direction ($-\vec{z}$) and overlaps the saturation beam inside the vapor. It is absorbed by atoms within the velocity interval given in equation 2.3.1 around $-v_z$. As, at any given time, only the population densities of the atoms around v_z is affected by the preparation beam, the readout beam will see a change in the population density only for the frequency of the laser source ω_0, because only there the condition $v_z = -v_z$ is fulfilled.

Of course, if spectroscopic features are very close to each other (not further apart than the width of the Doppler-broadened transition), the two beams can interact with different transitions of the same atom. The spectroscopic picture arising from these interactions depends on the exact spectroscopic method used and how the states that interact in the two transitions are connected (for example by relaxation). The details of these pictures will be discussed in the respective sections 2.3.1 and 2.3.2.

To achieve good results in a Doppler-free spectroscopy with limited laser power like in the Hg-magnetometer setup, the following points are important:

- The beams should be narrow to reduce the overall laser power needed for the spectroscopy without losing signal amplitude.
- In general, but especially if the beam diameters are small, mechanical stability of the beams over their whole path is important to keep the noise on the signal small.
- The angle between the saturation and the readout beam should be small, as a larger angle makes the Doppler-free features broader and smaller, as will be described in section 2.4.1. However, this can also be used as a feature as shown in section 3.4.1.1.

All spectroscopic measurements were done with commercially available cells with optical grade quartz windows having 1 mm and 5 mm optical paths between the windows. The cells were cleaned, evacuated and provided with liquid mercury droplets. The transmitted intensity for small intensities as a function of the penetration depth z is given by

$$I(z) \quad = \quad I_0 e^{-\frac{\sigma}{k_B T} p z},$$

with $\frac{\sigma}{k_B T} \approx 13900 \frac{1}{\text{Pa·m}}$ at room temperature [43]. The vapor pressure p is different for the different isotopes, depending on their natural abundances which are given in table 1.3.1. Before the beam is split for the spectroscopy, cylindrical lenses shape the beam to make it round. Additionally, spherical lenses are used to control the width and divergence, and thus the focal point of the laser beam along its path as described in section 3.2.4.

2.3.1 SATURATION SPECTROSCOPY

Saturation spectroscopy is a simple Doppler-free spectroscopy technique and produces robust spectra that can be described well by theoretic models. This facilitates an accurate fit to the spectroscopic data with a minimal number of free parameters. In saturation spectroscopy, the preparation beam is strong enough to saturate the transition under investigation and is often referred to as saturation beam. The readout beam is weak and probes the population densities as prepared by the saturation beam without affecting them notably. A schematic picture of a saturation spectroscopy setup is shown in figure 2.3.1.

Spectra are obtained by recording the power of the readout beam that is transmitted through the atomic vapor, as a function of the detuning of the laser frequency from the transition. As polarizing beam splitters are used to produce the two beams, both beams are linearly polarized by default. They can also be circularly polarized for the saturation spectroscopy if a transition with $\Delta m = \pm 1$ is under investigation and other transitions are to be ignored.

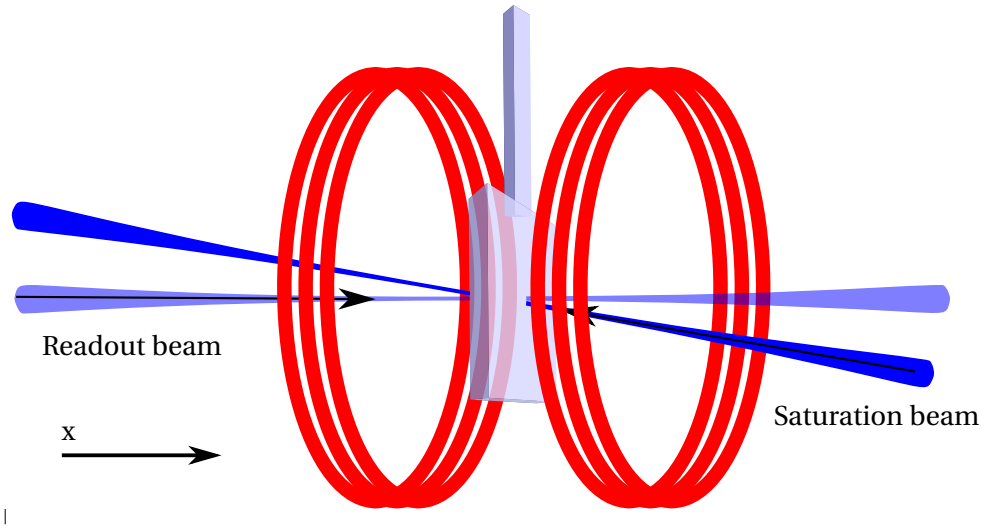

Figure 2.3.1: Schematic picture of a saturation spectroscopy setup. The strong preparation beam and the weak readout beam overlap inside the spectroscopy cell. A magnetic field can be applied with the Zeeman coils (red) to resolve the magnetic structure of the transitions.

2.3.1.1 *Signal shape*

The frequency dependent change in population density caused by the saturation beam as a function of detuning δ from resonance is determined by the shape of the laser line and the shape of the atomic transition. The natural line width of the magnetometer transition is 1.27 MHz and it has a Lorentzian shape $\mathscr{L}_\Gamma(\delta)$, where Γ is the width of the distribution. However, due to saturation effects, this can be broadened to several times its natural width. The shape of the broadened transition is still described by a Lorentzian. For more details on saturation broadening, see section 2.4.2.

Depending on whether the saturation beam populates or depopulates the level under investigation, the amplitude of $\mathscr{L}_\Gamma(\delta)$ can be positive or negative.

The transmission of the weak readout beam as a function of detuning from resonance depends on the density of atoms having the right velocity for the Doppler-shift to compensate the detuning, and the population densities of the levels interacting in this transition.

The velocity distribution of the mercury atoms along the direction of the readout beam can be described by a Gaussian G_d with the width d, which leads to an optical absorption parameter $\kappa(\delta) = C \cdot G_d(\delta)$ with a constant C. For a detuning δ close to zero, $\kappa(\delta)$ is additionally altered by the non-equilibrium population densities created by the saturation beam. The total absorption parameter is then

$$\kappa(\delta) = C \cdot G_d(\delta) \cdot (1 - g \cdot \mathscr{L}(\delta)). \tag{2.3.2}$$

Here, the scaling factor g includes the sign of the Lorentzian. With a transmission $A(z) = A_0 \cdot e^{-\kappa z}$ through a cell with the optical length z, to first order, the recorded signal is described by a Gaussian dip on the flat background A_0 with a much smaller

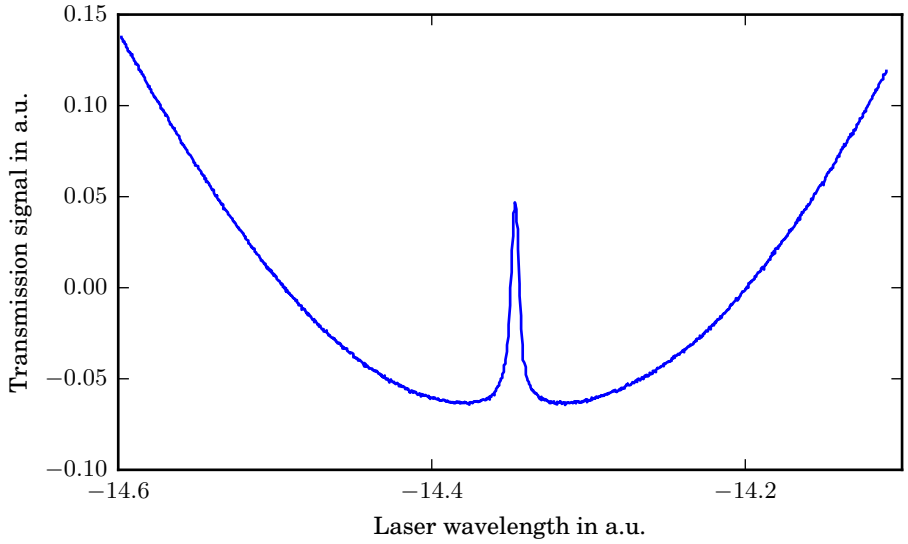

Figure 2.3.2: Transmission signal of the readout beam in saturation spectroscopy. The Doppler-free feature appears on top of a Doppler-broadened dip. No magnetic field was applied when this spectrum was recorded.

Lorentzian peak or dip on top. Figure 2.3.2 shows such a saturation spectroscopy signal of ^{202}Hg without a magnetic field applied to the spectroscopy cell.

2.3.1.2 *Structure of the magnetometer transition*

To construct the whole spectroscopic picture of the magnetometer transition regarding the magnetic sub-levels of the transition when a magnetic field is applied, the linear polarization of the pumping and readout beam can be seen as a superposition of σ^+ and σ^- light, driving the $\Delta m_f = \pm 1$ transitions. Ground state and excited state of the magnetometer transition both have the total angular-momentum quantum number $F = \frac{1}{2}$.

In the transmission signal of the readout beam, features show up for frequencies where one of the two possible transitions are resonant with the same atoms as one of the two transitions driven by the preparation beam. This is the case for atoms having a velocity that allows both beams to drive a transition at the same time. The following description of the possible interactions of readout and pumping beam is visualized in figure 2.3.3.

A magnetic field shifts the Zeeman levels $m_f \in \left\{\frac{1}{2}, -\frac{1}{2}\right\}$ by $\pm\beta$. A laser beam which is on resonance with the unshifted transition can only be absorbed by atoms having the z-velocity $v_{\text{zee}} = \pm c \cdot \frac{\beta}{\omega_0}$.

The σ^+ component of the saturation beam depletes the $m_f = -\frac{1}{2}$ level and populates the $m_f = \frac{1}{2}$ level for atoms having the velocity in beam direction v_{z^+}. At the same time, the σ^- component depletes the $m_f = -\frac{1}{2}$ and populates the $m_f = \frac{1}{2}$ level , but for atoms having the z-velocity $v_{z^-} = v_{z^+} + 2 \cdot v_{\text{zee}}$.

For the σ^+component of the readout beam, the population density created by the σ^+component of the saturation beam causes a positive Lorentzian peak in the spectrum, and the σ^-component causes a negative Lorentzian.

As the readout beam traverses the vapor in the opposite direction, when the saturation beam is on resonance with the σ^+ transition for atoms having the z-velocity v_{z^+}, the σ^+transition of the readout beam is on resonance with atoms having the z-velocity $-v_{z^+}$. This leads to the simultaneous-resonance condition

$$v_{z^+} = -v_{z^+} = 0. \tag{2.3.3}$$

Figure 2.3.3a visualises that both beams have the same frequency in the frame of the resting atoms.

Other than that, when the σ^+component of the readout beam interacts with a change of the population density caused by the σ^-component of the saturation beam, the energy difference between these two transitions is $2\cdot\beta$. For both beams to interact with the same atoms, the condition is

$$v_{z^+} = -v_{z^-}, \tag{2.3.4}$$

and with $v_{z^-} = v_{z^+} + 2\cdot v_{\text{zee}}$, this leads to

$$v_{z^+} = v_{\text{zee}} = -v_{z^-}. \tag{2.3.5}$$

Figure 2.3.3c shows this situation where the saturation beam has to be Doppler shifted up by the same amount as the probe beam is shifted down for an atom to be resonant with both beams simultaneously.

For the spectroscopic picture, this means that there is a positive Lorentzian feature on resonance with the σ^+transition and a negative Lorentzian feature shifted by $-\beta$ relative to the σ^+ transition. The latter can thus be found at the position the σ^+-transition would have without magnetic fields.

With the same arguments, it can be shown that the σ^- component has a positive Lorentzian feature on resonance with the σ^- transition, and negative feature at the position of the unshifted transition (see figures 2.3.3c and 2.3.3d). Combining the two circularly polarized components to a linearly polarized laser beam, the transmission signal is described by:

$$\begin{aligned}\kappa(\delta) = C^+\cdot G_d^+(\delta-\beta)\cdot(1-g^+\cdot\mathscr{L}(\delta-\beta)+g_2^+\cdot\mathscr{L}(\delta))\\ + C^-\cdot G_d^-(\delta+\beta)\cdot(1-g^-\cdot\mathscr{L}(\delta+\beta)+g_2^-\cdot\mathscr{L}(\delta))\end{aligned}$$

As long as the Doppler width is much larger than the Zeeman shift, the two Gaussians centered around the shifted σ^+ and σ^- transitions can be approximated to be the same:

$$G_d^+(\delta-\beta) \simeq G_d(\delta) \simeq G_d^-(\delta+\beta) \tag{2.3.6}$$

and the absorption parameter becomes

Table 2.3.1: All lines that can be observed in natural mercury for the ${}^1S_0 \rightarrow {}^3P_1$ transition. The number of possible transitions with $\Delta m = \pm 1$ is $\#t$, with $\#t_i$ different Zeeman sub-levels in the excited state. The number of features (#features) that can be caused by this configuration is $2 \cdot \#t_i - 1$. Features that are observed in the spectra that are shown in figure 2.3.4 show #pos positive- and #neg negative features.

isotope	F in ${}^1S_0$	F in ${}^3P_1$	$\#\ t$	$\#t_i$	#features	#pos, #neg	Ref.
199	$\frac{1}{2}$	$\frac{1}{2}$	2	2	3	2, 1	2.3.4a
199	$\frac{1}{2}$	$\frac{3}{2}$	4	4	7	4, 3	2.3.4h
201	$\frac{3}{2}$	$\frac{1}{2}$	4	2	3	2, 1	2.3.4e
201	$\frac{3}{2}$	$\frac{3}{2}$	6	4	7	4, 3	2.3.4g
201	$\frac{3}{2}$	$\frac{5}{2}$	8	6	11	6, 5	2.3.4b
even	0	1	2	2	3	3, 0	2.3.4f, 2.3.4d, 2.3.4c

$$\kappa(\delta) = C \cdot G_d(\delta) \cdot (1 - g^+ \cdot \mathscr{L}(\delta - \beta) + g_2^+ \cdot \mathscr{L}(\delta) - g^- \cdot \mathscr{L}(\delta + \beta) + g_2^- \cdot \mathscr{L}(\delta)). \quad (2.3.7)$$

With $g_2^\pm = g_2^+ + g_2^-$, this becomes

$$\kappa(\delta) = C \cdot G_d(\delta) \cdot (1 - g^+ \cdot \mathscr{L}(\delta - \beta) - g^- \cdot \mathscr{L}(\delta + \beta) + g_2^\pm \cdot \mathscr{L}(\delta)). \quad (2.3.8)$$

This is a Gaussian Doppler-broadened feature with Doppler-free features at the frequencies of the $\sigma^+$and the σ^- transition and one crossover feature at the undisturbed frequency of the hyperfine transition that points to the opposite direction. The Doppler-free features all have a Lorentzian shape in this model. However, as will be shown in chapter 2.4, the shape can be modified by line-broadening effects.

2.3.1.3 *Spectroscopy of the different hyperfine states*

When a magnetic field is applied to the vapor, features caused by even isotopes can be distinguished from those caused by odd ones in saturation spectroscopy. Also, the different hyperfine transitions of the odd isotopes can be identified based on their structure.

Table 2.3.1 provides an overview of the possible interactions between the saturation and the probe beam for different isotopes and their accessible hyperfine states. To identify the hyperfine states, one can count the number of transitions $\#t_i$ that have different energies when a magnetic field is applied. As the Zeeman shift of the magnetic sub-levels in the ground state can not be resolved, $\#t_i$ is the number of magnetic sub-levels in the excited state.

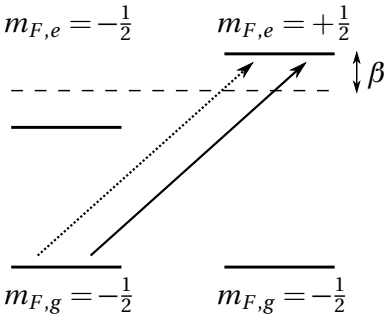

(a) Saturation- and readout beam driving the same transition. Less atoms can absorb the readout beam which leads to a higher transmission.

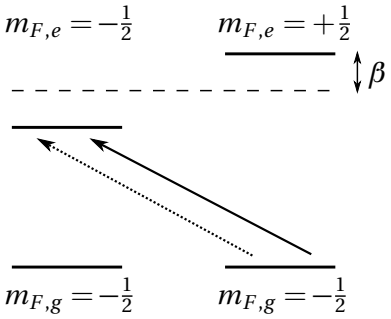

(b) Same situation as in (a) but for the opposite circular polarization of the laser light.

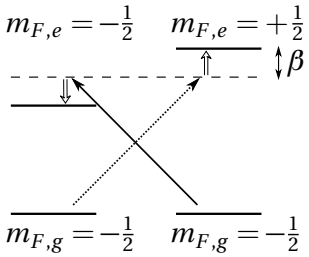

(c) Laser on resonance with the unshifted transition. The Doppler effect (double-arrows) shifts the saturation- and readout beam in opposite directions.

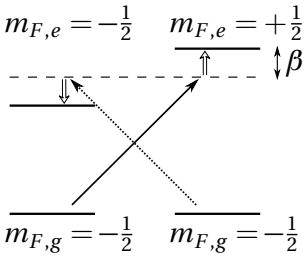

(d) Same situation as in (c) but for the opposite circular polarization of the laser light. The optical density for the readout beam is increased due to optical pumping with the saturation beam.

Figure 2.3.3: Simultaneous resonance conditions for the σ^+ and σ^- transition in probe- and saturation-beam. Dashed arrow: probe beam, solid arrow: saturation beam. In (a) and (b), the laser frequency is detuned by $+\beta$ and $-\beta$ and both beams are resonant with resting atoms. In (c) and (d), the laser frequency is neither resonant with the σ^+ nor the σ^-transition. However, the Doppler-effect can shift both beams by the same amount in opposite directions. This creates another possibility for the probe- and the saturation beam to interact with the same atoms, when the energy of the photons corresponds to the midpoint of the σ^+ and the σ^- transition.

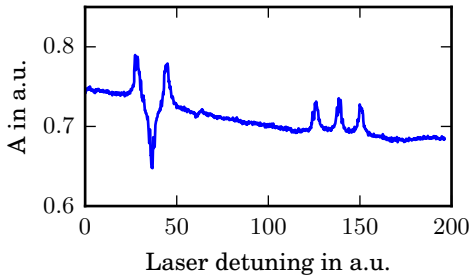

(a) ^{199}Hg (F=1/2) and ^{204}Hg with 4 A in the field coil.

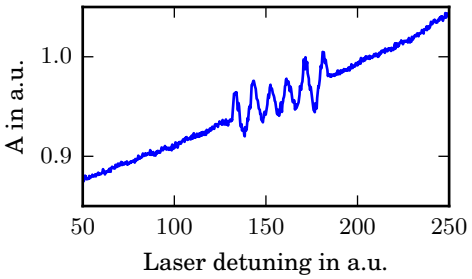

(b) ^{201}Hg (F=5/2) with 8 A in the field coil.

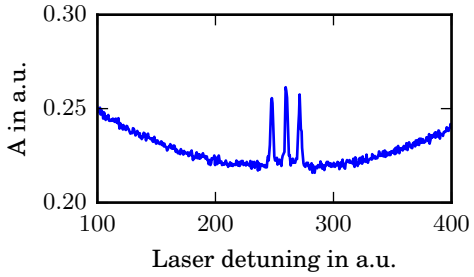

(c) ^{202}Hg with 4 A in the field coil.

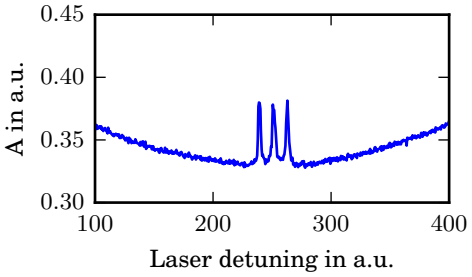

(d) ^{200}Hg with 4 A in the field coil.

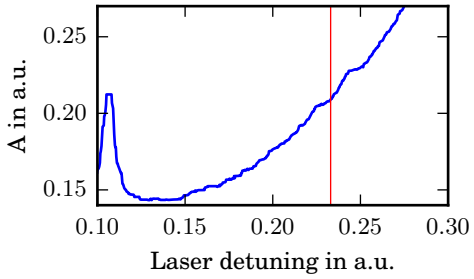

(e) ^{199}Hg (F=3/2) and ^{201}Hg (F=1/2), recorded in a different setup.

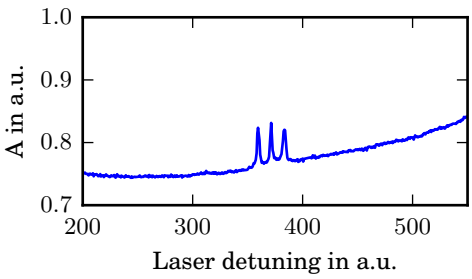

(f) ^{198}Hg with 4 A in the field coil.

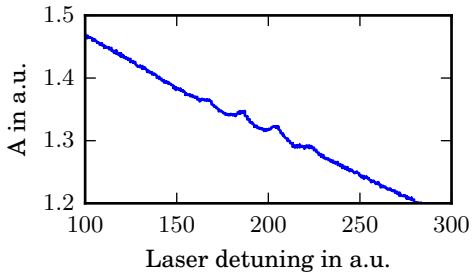

(g) ^{201}Hg (F=3/2), recorded in a different setup.

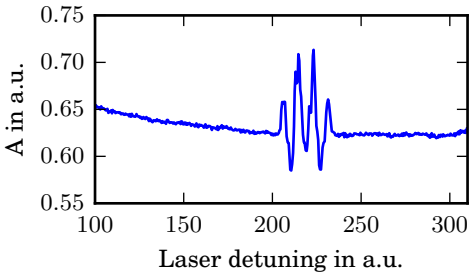

(h) ^{199}Hg (F=3/2) with 4 A in the field coil.

Figure 2.3.4: Transmission spectra obtained with saturation spectroscopy of the different hyperfine transitions of all naturally abundant isotopes in a magnetic field. The different shapes can be used to identify the transitions as described in section 2.3.1.3.

For ^{199}Hg (F=1/2) for example, there is one σ^+ and one σ^- transition or in total two transitions with different energies for each beam. The combination of each possible transition of the saturation beam with the energies $E^{(s)}(\sigma^\pm) = \omega_0 \pm \beta$ with each possible transition of the probe beam with the energies $E^{(p)}(\sigma^\pm) = \omega_0 \pm \beta$, potentially causes a feature in the spectroscopic picture at the mean value of the energies of the two transitions. The amplitude and its sign depend on how the population density that is probed by the readout beam is affected by the preparation beam. For the ^{199}Hg (F=1/2) transition, the features show up at the energies

$$E_1 = \overline{\left(E^{(s)}(\sigma^+), E^{(p)}(\sigma^+)\right)} = E(\sigma^+) = \omega_0 + \beta, \tag{2.3.9}$$

$$E_2 = \overline{\left(E^{(s)}(\sigma^-), E^{(p)}(\sigma^-)\right)} = E(\sigma^-) = \omega_0 - \beta, \tag{2.3.10}$$

and

$$E_3 = \overline{\left(E^{(s)}(\sigma^+), E^{(p)}(\sigma^-)\right)} \tag{2.3.11}$$

$$= \overline{\left(E^{(s)}(\sigma^-), E^{(p)}(\sigma^+)\right)} \tag{2.3.12}$$

$$= \frac{\omega_0 + \beta + \omega_0 - \beta}{2} = \omega_0, \tag{2.3.13}$$

which is the center between the two Zeeman shifted transitions and thus independent of the magnetic field.

In general, combining the $\#t_i$ transitions that can be driven by the preparation and the readout beam and determining their pairwise means, leads to $2 \cdot \#t_i - 1$ possible distinct values where features can be found in the spectroscopy. The sign of each feature depends on whether the pumping beam increases or decreases the population density seen by the probe beam for each combination.

For all even isotopes, $F = 0$ in the ground state and $F = 1$ in the excited state. Like for ^{199}Hg, there are two transitions with different energies, but the feature caused by the cross-talk of the σ^+ and the σ^- transition is positive as shown in figure 2.3.4c, 2.3.4d, and 2.3.4f. The reason for this is that the saturation beam always depletes the sole ground state on resonance.

Figure 2.3.4 shows the transitions as observed with the saturation spectroscopy setup. All spectra but the ones showing ^{201}Hg (F=1/2) and ^{201}Hg (F=3/2) were obtained using a spectroscopy setup where the saturation beam was weakened by a neutral-density filter (ND filter) and reflected back through the cell as probe beam. This avoids broadening of the features due to an angle between the two beams (see section 2.4.1). However, ^{201}Hg (F=1/2) and ^{201}Hg (F=3/2) could not be resolved and were recorded later in a setup that had a nonzero angle between the two beams but a lower noise on the transmission signal. The ^{201}Hg (F=1/2) transition is again not resolved well. The large feature on the left is one of the features of the ^{199}Hg (F=3/2) transition and is included for reference. The red line indicates where the ^{201}Hg (F=1/2) transition is expected to be, based on [80].

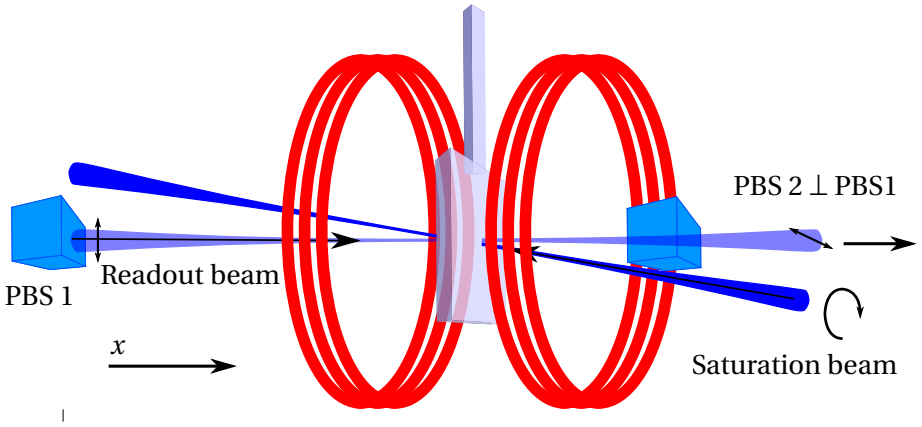

Figure 2.3.5: Schematic picture of a polarization spectroscopy setup. The strong preparation beam and the weak readout beam overlap inside the spectroscopy cell. The polarizing beam splitter cubes in the readout beam are crossed. A magnetic field can be applied with the Zeeman coils (red) to resolve the magnetic structure of the transitions.

2.3.2 POLARIZATION SPECTROSCOPY

Another technique to produce Doppler-free signals, but with a lower Doppler-broadened background than saturation spectroscopy, is polarization spectroscopy [81]. Due to the lower background, it is less sensitive to power fluctuations. Like in saturation spectroscopy, a laser beam is split and the two beams intersect in the mercury vapor coming from opposite directions.

Starting from a saturation spectroscopy setup, a second beam splitter cube with the polarization axis oriented orthogonal to the first one is added to the readout beam as shown in figure 2.3.1. If the two polarizers were perfect, no power would be transmitted through the second one as long as the light is off-resonant. On resonance, the polarization of the readout beam is modified by the birefringence created by the preparation beam.

The linearly polarized light of the probe beam can again be described by two counter-rotating circularly polarized waves. As the laser wavelength is scanned through resonance, the refractive indices $n_\pm$ and the absorption coefficients $\alpha_\pm$ of the mercury vapor are affected differently for the two circular polarization components. This leads to a rotation and an elliptical deformation of the linear polarization (see figures 2.3.6 and 2.3.7). Consequently, the polarization is not perfectly orthogonal to the second polarizer anymore, and a small intensity is transmitted.

A big advantage of this technique over saturation spectroscopy is the small background of the resulting signal due to the crossed polarizers.

The shapes of the Doppler-free features depend on the transition under investigation, the exact angle between the linear polarizers in the probe beam, and the polarization of the preparation beam. For a detailed discussion of polarization spectroscopy, see [81].

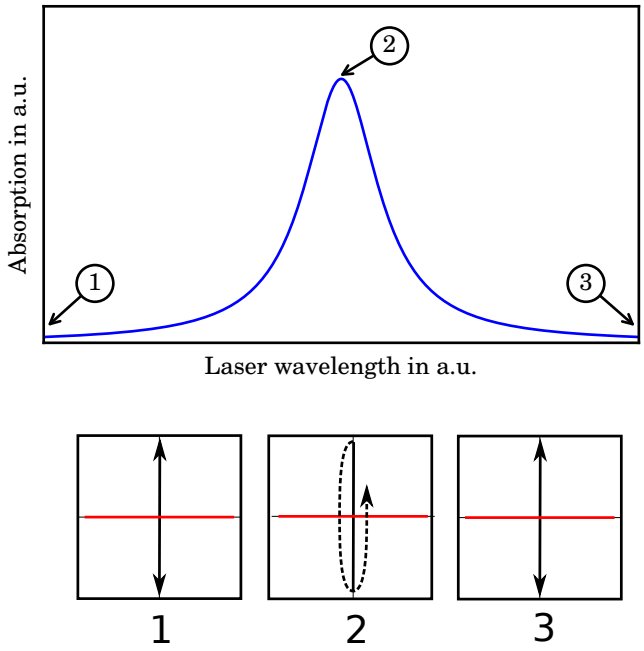

Figure 2.3.6: Absorption of a linearly polarized laser beam in a polarized ^{199}Hg vapor. The linear polarization can be written as two counter-rotating circular polarization components. In polarized vapor, the absorption is stronger for one of the two circular polarization components. The transmitted laser beam thus obtains a circular polarization component.

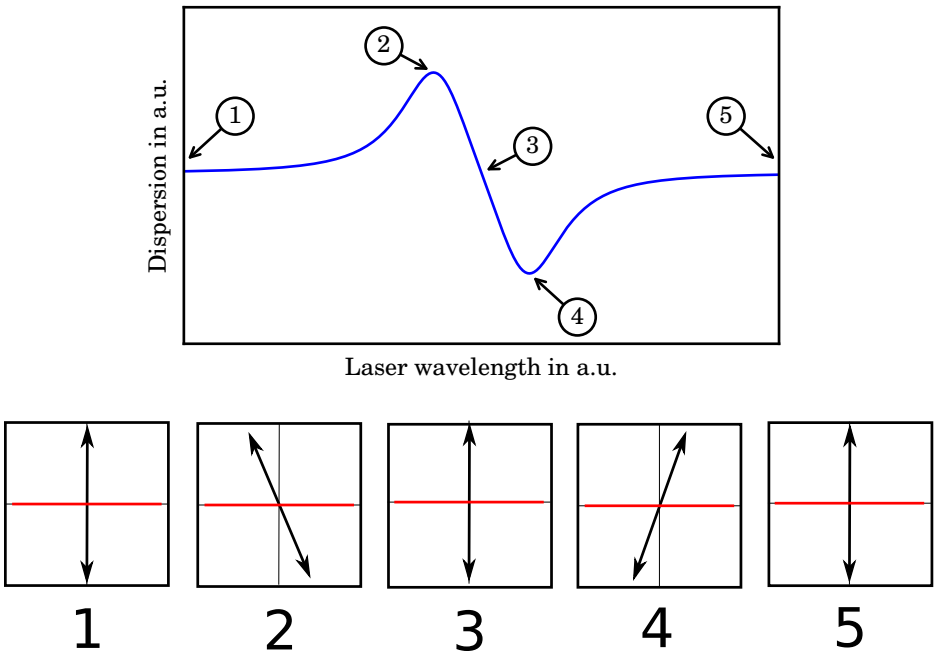

Figure 2.3.7: Optical dispersion in polarized ^{199}Hg vapor. The dispersion near resonance is different for the two circular polarization components of a linearly polarized laser beam passing a polarized atomic vapor. This leads to a phase shift between the two circular polarization components.

Signals can be selectively made dispersive, pure Lorentzian or a mixture of both. This technique can produce dispersive signals with a low Doppler-broadened background centered around a Zeeman shifted transition. Section 3.4.1.2 shows how the advantages of polarization spectroscopy can be used to improve the accuracy and flexibility of the frequency lock of lasers.

2.4

BROADENING EFFECTS IN DOPPLER-FREE SPECTROSCOPY

Several effects can broaden the features in Doppler-free spectroscopy. Because the frequency resolution of a spectroscopy gets worse as the features get broader, this should usually be avoided if possible. The fact that these mechanisms can also change the shape of the features makes it even more important to understand them in detail. To determine the resonance frequency of a feature in a spectrum, the signal has to be fitted. However, to develop a suitable mathematical model, the effects have to be well understood.

On the other hand, the broadening effects can also be advantageously in some cases. In section 3.4.1 will be shown how this is used to optimize the slope of an error signal for frequency locking the laser.

2.4.1 ANGLE BROADENING

When the two laser beams in Doppler-free saturation spectroscopy traverse the atomic vapor completely anti-parallel (i.e., when the angle between the two beams is zero), the Doppler effect is completely suppressed for the narrow spectroscopic features. However, if there is a non-zero angle between the two laser beams, the Doppler-effect contributes to the width of these features again.

In an intuitive approach to understand this effect, figure 2.4.1 shows the velocity of an atom $\vec{v}_{\text{tot}}$ and its projection on the k-vector of the laser beam $v_{\parallel}$.

Atoms with $v_{\parallel}$ see the laser frequency shifted by

$$\omega = \omega_0(1 + \frac{v_{\parallel}}{c}). \tag{2.4.1}$$

The length of $v_{\parallel}$ in figure 2.4.1 represents the velocity needed to compensate a given detuning ω of the laser from resonance. The atoms' total velocity $\vec{v}_{\text{tot}}$ can be decomposed into $v_{\parallel}$ and a component $v_{\perp}$ which is perpendicular to the k-vector of the laser beam. As $v_{\parallel}$ is determined by equation 2.4.1 when the detuning ω is given, for an atom to absorb the laser beam, its velocity vector $\vec{v}_{\text{tot}}$ has to point to some point on the plane that is normal to $\vec{k}$ ($v_{\perp}$-plane in figure 2.4.1). The distribution depicted along the y axis in figure 2.4.1 represents the number of atoms

$$n^{\beta}(v_i)\mathrm{d}v_i, \tag{2.4.2}$$

where β is the width of the distribution, that have a velocity within the interval $[v_{\text{i}}, v_i + \mathrm{d}v_i]$ projected onto an arbitrary axis i. As the velocity distribution is isotropic, $n^{\beta}(v_i)$ is the same for all freely chosen axes i. For an ideal gas, it is given by

$$n^{\beta}(v_i)\mathrm{d}v_i \propto e^{-\left(\frac{v_i}{\beta}\right)^2}\mathrm{d}v_i. \tag{2.4.3}$$

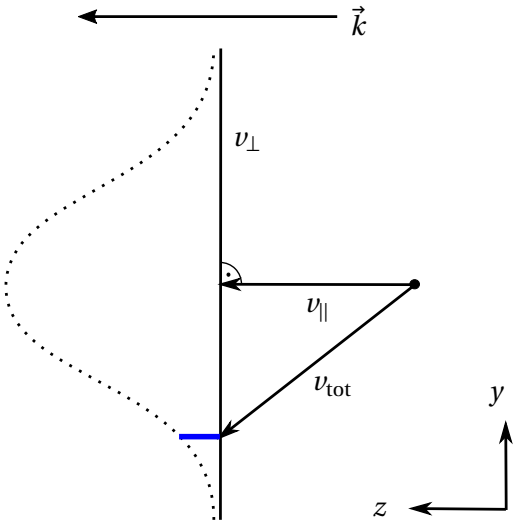

Figure 2.4.1: Decomposition of a particle's velocity parallel and orthogonal to the direction of the laser beam. The dotted line shows the probability distribution for atoms in thermal equilibrium to have the corresponding velocity in y-direction.

In Doppler-broadened spectroscopy with only one beam traversing the vapor, the absorption of laser light is proportional to $n^\beta(v_\parallel)$.

Figures 2.4.2a and 2.4.2b show the same velocity decomposition as figure 2.4.1, but for preparation and readout beam at the same time, for the case when they are aligned perfectly anti-parallel. Scanning the laser through resonance, the length of $v_\parallel$ is scanned from positive to negative values for one beam and vice versa for the other. For both beams to interact with one atom, its velocity vector has to point to both $v_\perp$ planes at the same time, which corresponds to the condition

$$v_{\parallel,r} = v_{\parallel,s}. \tag{2.4.4}$$

Here, the only $v_\parallel$ where this condition is fulfilled is $v_\parallel = 0$. At this point, all atoms with any v_y fulfill 2.4.4 simultaneously and the velocity distribution has no effect.

However, when there is a nonzero angle between the laser beams, as shown in Figures 2.4.2c and 2.4.2d, the $v_\perp$ planes intersect also for nonzero $v_\parallel$. The coordinate system is chosen such that both beams now have an angle $\frac{\theta}{2}$ to the z-axis and no x-component. Then they have a common y-component, and still opposite z-components. The strength of the resulting interaction between the two beams and thus the effect on the transmission of the readout beam depends on the number of atoms with the y-velocity

$$v_{\text{y}}^r = v_{\text{y}}^s = v_{\text{y}}^{\text{res}}, \tag{2.4.5}$$

where "res" stands for resonance.

As the x-axis is chosen such that the beams do not have an x-component, the atoms' velocities can have an arbitrary x-component. The y-component is linked to the component parallel to the laser beam and thus defining the Doppler-shift through equation 2.4.1 by

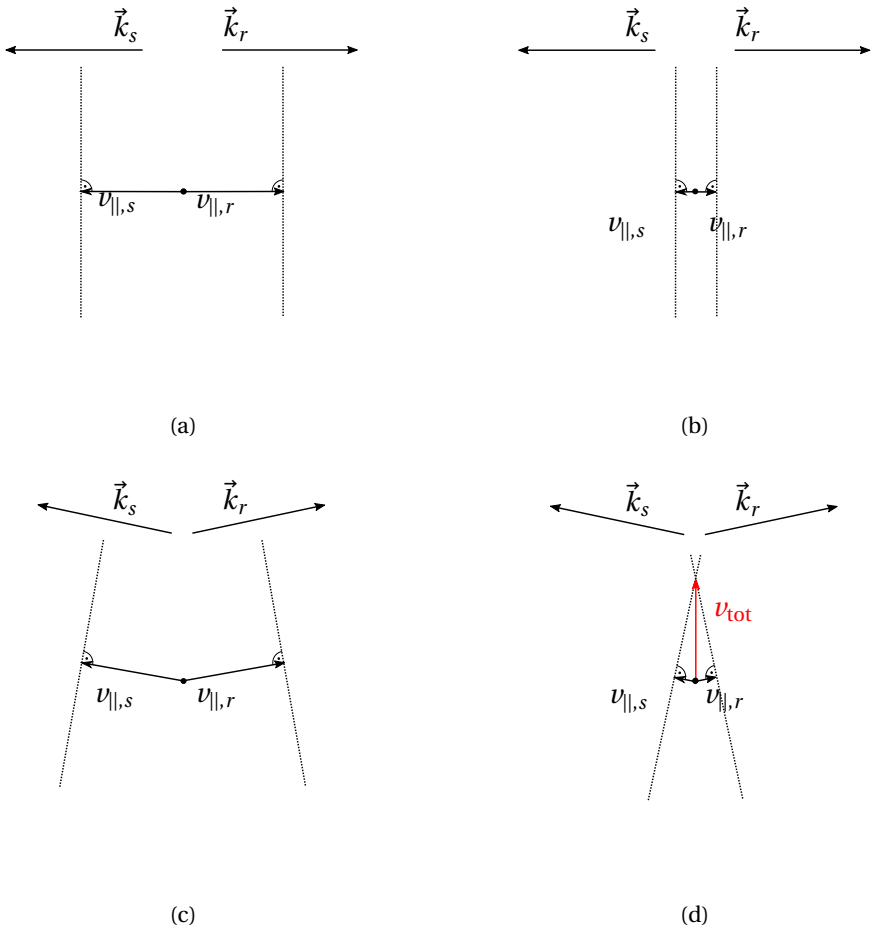

Figure 2.4.2: Scanning the frequency detuning of the laser from large to small values. In (a) and (b), the beams are perfectly anti-parallel, in (c) and (d) there is a nonzero angle between them. For anti-parallel beams, an atom can only interact with both beams when $v_{\parallel}^{s} = -v_{\parallel}^{r} = 0$. If there is a non-zero angle between the two beams, atoms with a nonzero velocity v_{tot} can interact with both beams simultaneously, as shown in (d).

$$v_{\mathrm{y}}^{\mathrm{res}} = \frac{v_{\parallel}}{\sin(\frac{\theta}{2})}. \tag{2.4.6}$$

Along the y-axis, the velocity distribution is given by equation 2.4.3.

When the laser frequency is scanned through resonance, the strength of the interaction is proportional to the number of atoms with v_y^{res} per velocity interval $d\,v_{\parallel}$

$$\begin{aligned} n\left(v_{\mathrm{y}}^{\mathrm{res}}(v_{\parallel})\right) d\,v_{\parallel} &= C \cdot e^{-\left(\frac{v_y^{res}}{\beta}\right)^2} \\ &= C \cdot e^{-(\frac{v_{\parallel}}{\beta \cdot \sin(\frac{\theta}{2})})^2} d\,v_{\parallel}. \end{aligned} \tag{2.4.7}$$

This is the same distribution as in equation 2.4.3, but with the width $\beta \cdot \sin\left(\frac{\theta}{2}\right)$ instead of β. When a Lorentzian profile is used for the resonant velocity instead of a δ-function at $v_{\mathrm{y}}^{\mathrm{res}}$, the line shape of the resulting Doppler-free feature is a convolution of a Gaussian with the width $\beta \cdot \sin\left(\frac{\theta}{2}\right)$ and the Lorentzian with the natural linewidth of the transition, which can be described by a Voigt profile.

The Gaussian contribution can quickly become the dominating effect for the line width. For a transition that is Doppler-broadened to 1 GHz, an angle between the two beams of 10 mrad already causes a Gaussian broadening of ~5 MHz.

2.4.2 SATURATION BROADENING

For light passing through atomic vapor with a low intensity, the absorption rate is directly proportional to the intensity. However, when the intensity and thus the absorption rate increases, the population of the involved levels is altered significantly, causing the absorption rate to grow slower than proportional to the laser intensity. This means that the fraction of the light that is transmitted increases with the intensity of the laser beam. For laser beams with infinitely large intensities, the vapor would become invisible.

The saturation parameter $S(\omega)$, which is defined as the ratio between the absorption and relaxation rate in the atomic vapor, changes with the detuning of the laser from resonance and gets smaller as the absorption probability at the wing of the transition goes down. However, due to the non-linearity mentioned above, the saturation parameter does not decrease proportional to the absorption probability. This causes a broadening of the Doppler-free feature. It still has a Lorentzian shape, but the width is

$$\Delta\omega_S = \Delta\omega(1+S_0)^{\frac{1}{2}}, \tag{2.4.8}$$

where $\Delta\omega$ is the natural linewidth, and $S_0 = S(\omega_0)$ [82].

2.5 MEASUREMENTS

The Doppler-free spectroscopy setup that was developed for this project is capable of measuring atomic properties of mercury that are crucial for mercury magnetometry and can furthermore be useful for other experiments using ^{199}Hg.

To improve the accuracy of the magnetic field measurements, the difference between the $^1S_0 \rightarrow {}^3P_1$ lines for ^{199}Hg and ^{204}Hg (referred to as relative isotope shift in the following) was measured. This was necessary as the uncertainty of the literature value of this relative isotope shift was too large for our purpose. This value is important as it is used for calibrating the frequency axis for spectroscopic measurements as done in section 2.5.3 and to set the laser frequency as described in section 3.4.1. Any uncertainty of the laser frequency leads to an uncertainty of the magnetic field measurement due to the light shift as described in section 3.3.1. To avoid that this effect dominates the uncertainty of the magnetic field measurement, the relative isotope shift was measured with a higher accuracy (see section 2.5.2).

With the DC Stark shift becoming relevant as a new source of a systematic effect in EDM measurements, it has to be accounted for in the frequency lock of the laser. This is described in more detail in section 3.3.4.1. Section 2.5.3, shows a spectroscopy setup with the capability to apply an electric field to the atomic vapor. A Stark shift measurement in this setup demonstrates that high voltage can be applied to a quartz cell containing vapor pressure mercury and the Stark shift can be resolved.

2.5.1 FITTING THE SPECTRA

Most of the Doppler-free spectra recorded with this setup are composed of Lorentzian or Voigt peaks pointing up or down on Doppler-broadened Gaussian backgrounds, as described in section 2.3.1. Depending on the method used to obtain the Doppler-free features, whether a magnetic field was present, and which isotopes are to be investigated, the Doppler-free peaks are distributed differently on the, sometimes overlapping, Doppler-broadened backgrounds. Whether the Doppler-free features have a pure Lorentzian line shape or are better described by Voigt functions, depends on the broadening mechanisms that were present while the spectra were recorded. When there is a non-zero angle between the preparation beam and the readout beam, the initially Lorentzian features are broadened and obtain a Gaussian component as shown in section 2.4.1. This makes the Voigt function the best theoretical model to describe their shape. A flexible fitting routine was developed to make it possible to fit different kinds of spectra with only few manual inputs required.

In a first step, the parameter guesser tries to find the positions of all Doppler-free features in the spectrum. As the data analysts usually know how many peaks they are expecting to find in the spectrum, the guesser uses this number of expected peaks N_p as an input. This makes it easier to avoid falsely identifying random background spikes

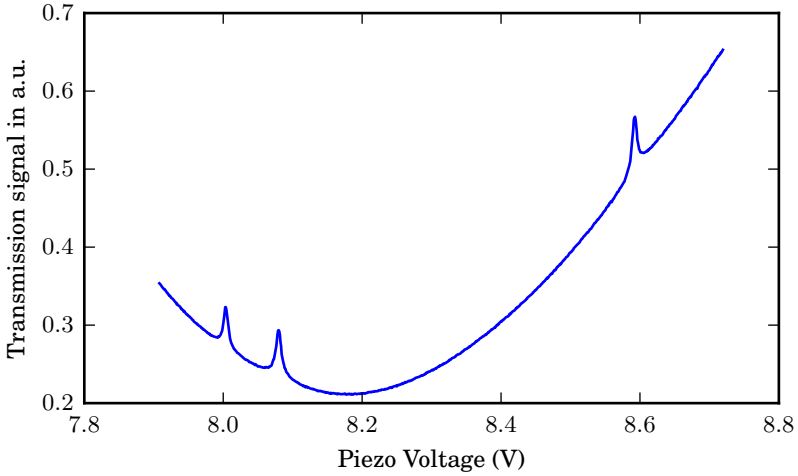

Figure 2.5.1: Raw saturation spectroscopy signal showing the transitions in ^{199}Hg, ^{204}Hg and ^{201}Hg.

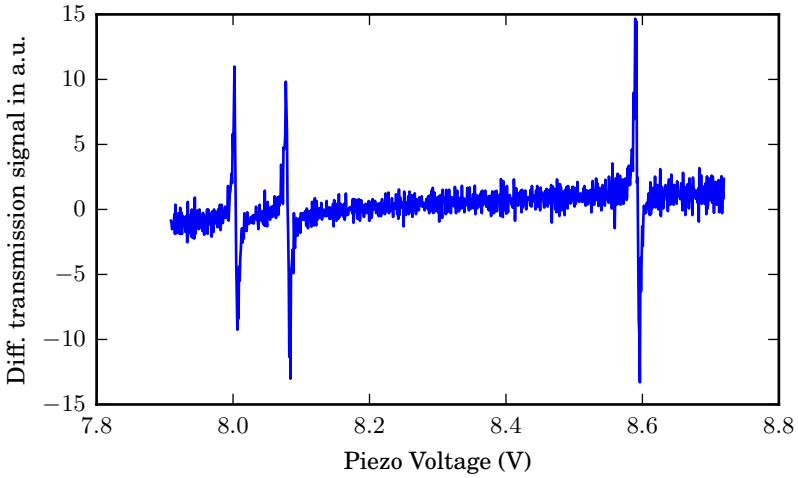

Figure 2.5.2: Derivative of the signal shown in figure 2.5.1. This is used to make the parameter guessing for the Doppler-free features more robust.

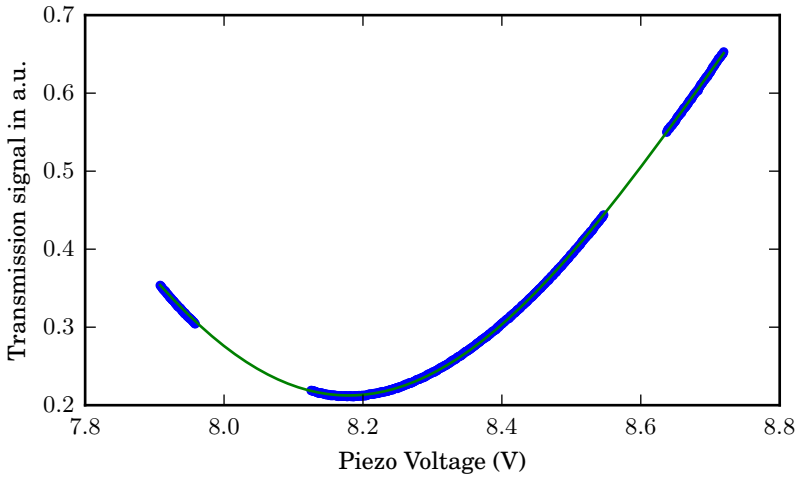

Figure 2.5.3: Raw signal with the regions around the peaks cut out. In a first step, the Doppler-broadened background is fitted to this signal without Doppler-free features to get accurate staring parameters for the fit to the whole signal.

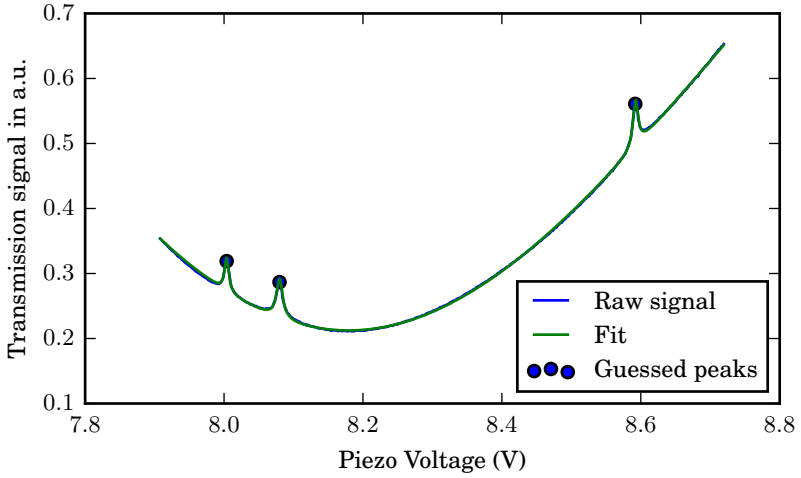

Figure 2.5.4: Raw signal and fit to it. Here, the whole model was fitted (Doppler-broadened background plus Doppler-free features). The large points mark the peaks as guessed.

as signals. Instead of having to carefully define thresholds for accepting or rejecting a peak, a coarse threshold is used to generate a larger list of possible peaks. The probability of each peak to be a real signal is then computed, and only the best results are accepted until the predefined number of peaks is reached.

This procedure is illustrated in the following with signals that were recorded for the measurement of the isotope shift (see section 2.5.2). The raw signal showing features caused by ^{199}Hg (F=1/2) , ^{204}Hg, and ^{201}Hg (F=3/2) without a magnetic field applied to the atomic vapor is shown in figure 2.5.1.

First, the derivative of the spectrum is computed. This transforms the not very steep Gaussian background to values close to zero and Lorentzian features to dispersive signals as shown in figure 2.5.2. After identifying the positions of all positive and negative features in this spectrum above a threshold, the probability of each pair of positive and negative peaks to be part of the same dispersive signal is computed. It turned out to be enough to evaluate how symmetric and how close together the peaks are. This is done by inverting the sign of the amplitude of the negative peaks. Then, the relative distances between all inverted peaks to all positive peaks is computed and the N_p pairs with the smallest distances are assumed to be caused by real features in the signal.

In a next step, the guessed peaks are cut out of the raw signal as shown in figure 2.5.3. This helps to fit the Gaussian background. In this spectrum, there are three transitions that all cause a Doppler-free feature and a Doppler-broadened feature. Although the Doppler-broadened features overlap, it would not be accurate to fit one Gaussian peak to the background signal. Instead, the sum over a Gaussian for each transition is used (see figure 2.5.3).

The result of the background fit and the guessed parameters for the Doppler-free features are used as initial guesses for the parameters in a complete model of the signal and the parameters are optimized with a least squares fit. Figure 2.5.4 shows the original data and the final fit. The large points mark the peaks as guessed in the parameter guessing procedure.

2.5.2 ISOTOPE SHIFT

All spectra that are generated with this setup are recorded with the voltage that is applied to the piezo (see section 2.2.1) on the x-axis. To find the right point in the spectroscopy for the laser-lock to stabilize the frequency of the laser to the no-light-shift point (NLP) (see section 3.4.1), and to extract the frequency information from spectroscopy signals as done in section 2.5.3, this voltage has to be converted to the frequency of the laser light. A frequency standard that is genuinely available in this spectroscopy is the relative isotope shift between the ^{199}Hg and the ^{204}Hg lines which are very close to each other. The frequency difference between these peaks serves as a calibration source of the x-axis in the vicinity of the ^{199}Hg peak, and has the advantage that it does not change or drift due to any environmental parameters.

Unfortunately there is no published value of this shift with a sufficient accuracy for the purpose of using it as a standard. The best published measurement can be found in [80] with a relative isotope shift between the two lines of (97 ± 17) MHz.

Therefore, in order to enhance the accuracy of the laser lock and values that are extracted from mercury spectra, the relative isotope shift between ^{199}Hg and ^{204}Hg was measured again with the available spectroscopy setup within the context of this work.

2.5.2.1 *Measurement procedure*

For an auxiliary calibration of the x-axis, the Zeeman coil was used to produce a known magnetic field that splits the magnetic sub levels. A saturation spectroscopy setup was chosen to resolve this splitting. Because the Zeeman coil is relatively small, measuring the magnetic field next to the spectroscopy cell would not provide an accurate enough estimate of the magnetic field at the point where the two laser beams overlap. Instead, the magnetic field was measured using the Zeeman shift in spectra containing features caused by transitions in ^{198}Hg and ^{201}Hg (F=3/2). As the relative isotope shift between these two had been measured with sufficient accuracy before [80], it is suited to serve as a calibration source for the frequency axis of the magnetic field measurement.

When the magnetic field is known, the x-axis of a spectrum containing ^{199}Hg and ^{204}Hg features can be calibrated using the Zeeman splitting of ^{204}Hg.

2.5.2.2 *Analysis procedure*

In a first step, spectra containing the $^1S_0 \rightarrow {}^3P_1$-transition of ^{198}Hg and ^{201}Hg (F=3/2) with the voltage applied to the piezoelectric crystal on the x-axis are recorded for different currents in the field-coil (see figure 2.5.5b) and the Zeeman splitting is extracted from a fit. The splitting between the two hyperfine transitions $\Delta\mathrm{IS}^V_{198-201_{F=3/2}}$ could be extracted from the same spectrum. However, as the Zeeman splitting leads to a bad resolution of the ^{201}Hg (F=3/2) peak, a second spectrum is recorded without a current in the field coil (see figure 2.5.5a). From this spectrum, the splitting between the two isotopes can be extracted more accurately.

The spectra with and without magnetic field were recorded 50 times for each current value. As the fit did not converge correctly in some cases, results that deviated more than 3σ from the median of the values of each current setting were dismissed. While the Zeeman splitting of the ^{198}Hg transition Z^V_{198} grows linear with the current in the field coil, the isotope shift $\Delta\mathrm{IS}^V_{198-201_{F=3/2}}$ is independent of the magnetic field. In the following, the slope of the Zeeman splitting as a function of the current in the field coil is m^V_{198}.

Spectra showing features caused by ^{199}Hg (F=1/2) and ^{204}Hg (see figure 2.5.6) were recorded for the same current settings in the field-coil.

With these values and the literature value for the difference $\Delta\mathrm{IS}^{\mathrm{freq}}_{198-201_{F=3/2}}$ between the $^1S_0 \rightarrow {}^3P_1$-transition of ^{198}Hg and ^{201}Hg (F=3/2), of (0.6763 ± 0.0004) GHz [80], the

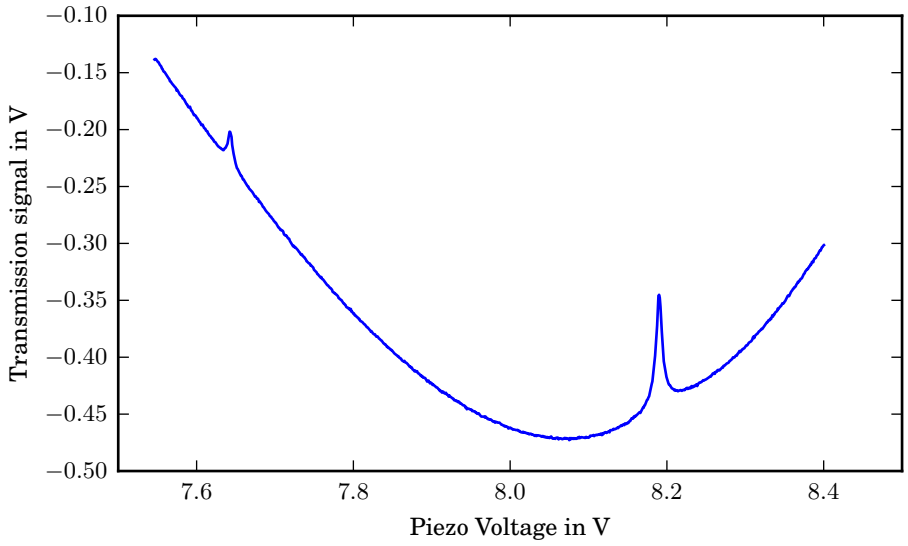

(a) Without magnetic field

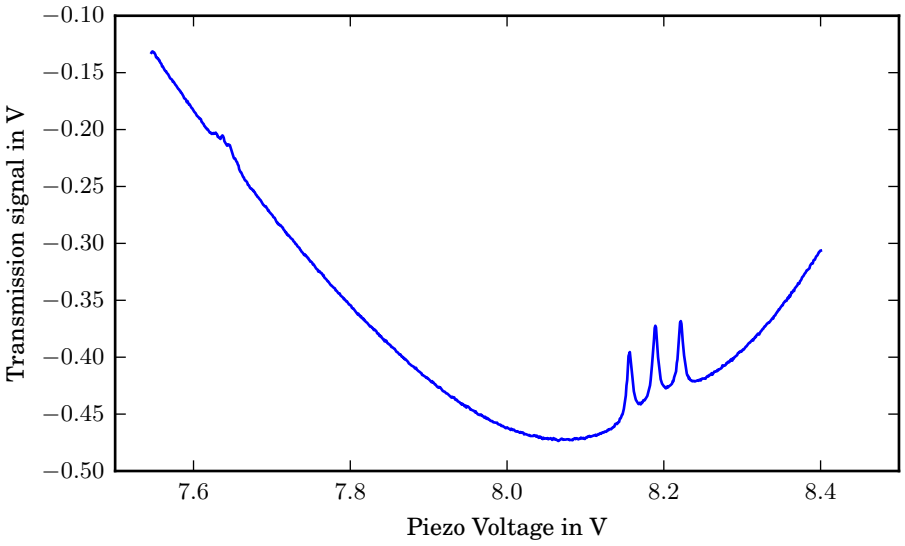

(b) With magnetic field

Figure 2.5.5: Spectra showing the $^1S_0 \rightarrow {}^3P_1$-transition of ^{198}Hg and ^{201}Hg (F=3/2). The spectrum without magnetic field is used to extract the isotope shift, and the spectrum with magnetic field is used to extract the Zeeman splitting.

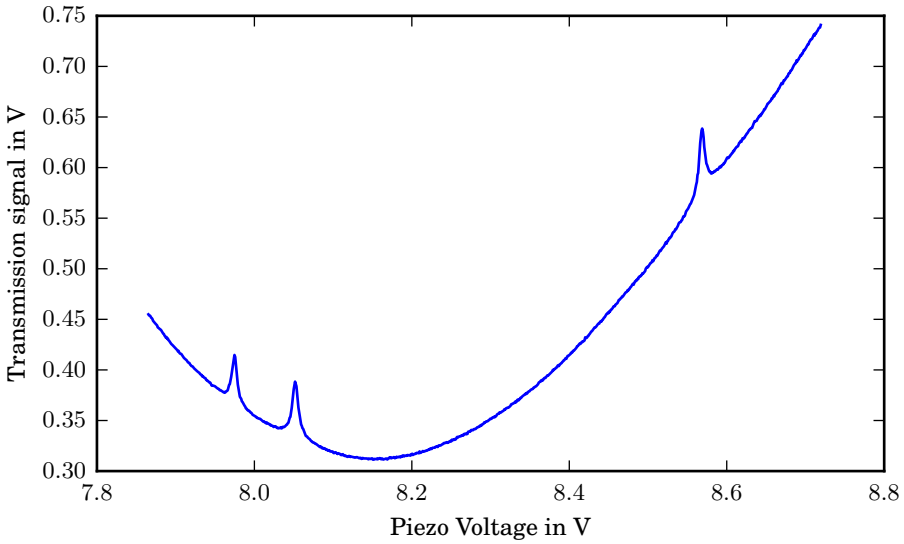

(a) Without magnetic field

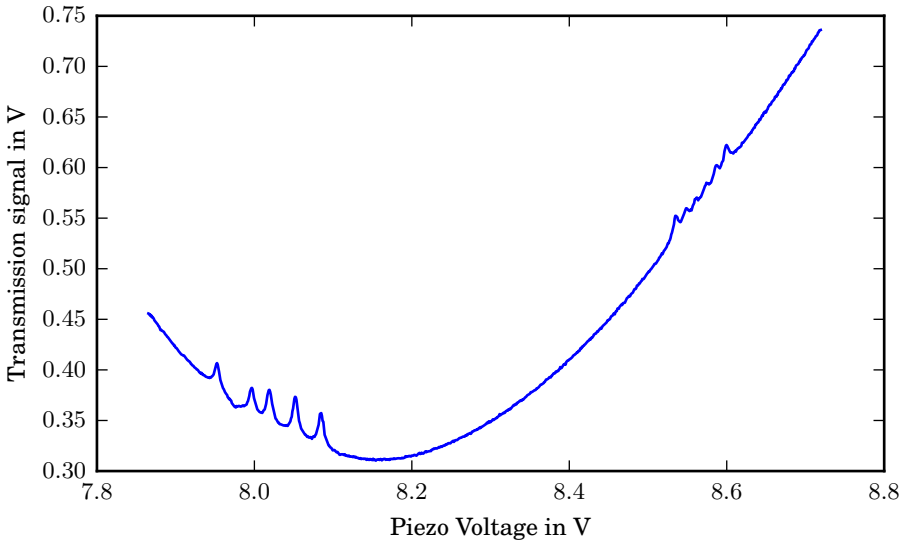

(b) With magnetic field

Figure 2.5.6: Spectra showing the $^1S_0 \rightarrow {}^3P_1$-transition of ^{199}Hg (F=1/2), ^{204}Hg and ^{201}Hg (F=5/2). The spectrum without magnetic field is used to extract the isotope shift, and the spectrum with magnetic field is used to extract the Zeeman splitting.

slope m_{198}^{freq} of the Zeeman splitting of the ${}^3P_1$-state of ^{198}Hg in Hz when it is plotted against the current in the field coil can be calculated:

$$m_{198}^{\text{freq}} = m_{198}^{V} \cdot \frac{\Delta\text{IS}^{\text{freq}}_{198-201_{F=\frac{3}{2}}}}{\Delta\text{IS}^{V}_{198-201_{F=\frac{3}{2}}}}. \tag{2.5.1}$$

The calibration of the frequency axis in the spectra containing the ^{199}Hg peak uses the same relation, and leads to the relative isotope shift between ^{199}Hg and ^{204}Hg

$$\Delta\text{IS}^{\text{freq}}_{199-204} = \Delta\text{IS}^{V}_{199-204} \cdot \frac{m_{204}^{\text{freq}}}{m_{204}^{V}}. \tag{2.5.2}$$

Using the approximation that the Zeeman splitting of the excited state in ^{204}Hg is the same as in ^{198}Hg,[1] one can use $m_{204}^{\text{freq}} = m_{198}^{\text{freq}}$ and calculate the difference $\Delta\text{IS}^{\text{freq}}_{199-204}$ in Hz between the ${}^1S_0 \rightarrow {}^3P_1$-transition of ${}^{199}\text{Hg}_{F=\frac{1}{2}}$ and ^{204}Hg:

$$\Delta\text{IS}^{\text{freq}}_{199-204} = \frac{\Delta\text{IS}^{V}_{199-204} \cdot m_{198}^{V} \cdot \Delta\text{IS}^{\text{freq}}_{198-201_{F=3/2}}}{m_{204}^{V} \cdot \Delta\text{IS}^{V}_{198-201_{F=3/2}}}. \tag{2.5.3}$$

Correlations

Spectra resolving the Zeeman splitting and the Isotope shifts are recorded in an alternating sequence. Fluctuations of measurement results of both are composed of fluctuations of the frequency response of the piezo crystal, and noise on the spectroscopy signal amplitude. While the noise on the signal amplitude is uncorrelated, the fluctuations of the frequency response can be partially correlated. Figure 2.5.7 shows the results of the fits to the recorded spectra while a current of 2.4 A was applied to the magnetic field coil. In figure 2.5.7a and figure 2.5.7b, the Zeeman splittings and the relative isotope shifts that were extracted from the spectra are shown. Figure 2.5.8 shows the Zeeman splitting on the y-axis and the isotope shift on the x-axis.

These correlations are useful as they cancel out a potentially large uncertainty. The frequency response of the laser to the voltage that is applied to the piezoelectric crystal can drift over time and the linear component of this drift changes the measured values m_{198}^{V} and m_{204}^{V} . However, this drift is visible in the isotope shift measurements $\Delta IS^{V}_{198-201_{F=3/2}}$ and $\Delta IS^{V}_{199-204}$ which should be independent of the current applied to the field coil. Instead of extracting m_{198}^{V}, m_{204}^{V}, $\Delta\text{IS}^{V}_{198-201_{F=3/2}}$ and $\Delta\text{IS}^{V}_{199-204}$ from the data independently, substituting $m_{198} = \frac{m_{198}^{V}}{\Delta\text{IS}^{V}_{198-201_{F=3/2}}}$ and $m_{204} = \frac{m_{204}^{V}}{\Delta\text{IS}^{V}_{199-204}}$ in 2.5.3, leads to

1 Differences in the Zeeman splitting between different isotopes are typically small. For example, [83] quotes a relative difference of the g-factors of two Ca-ions to be 10^{-8}. For our purpose a relative difference of 10^{-3} would be small enough.

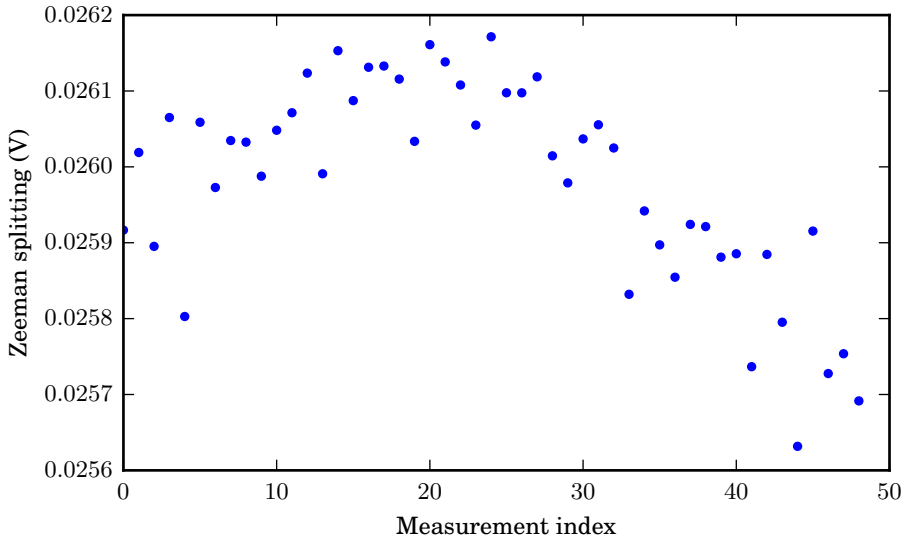

(a) 50 Consecutive measurements of the Zeeman splitting

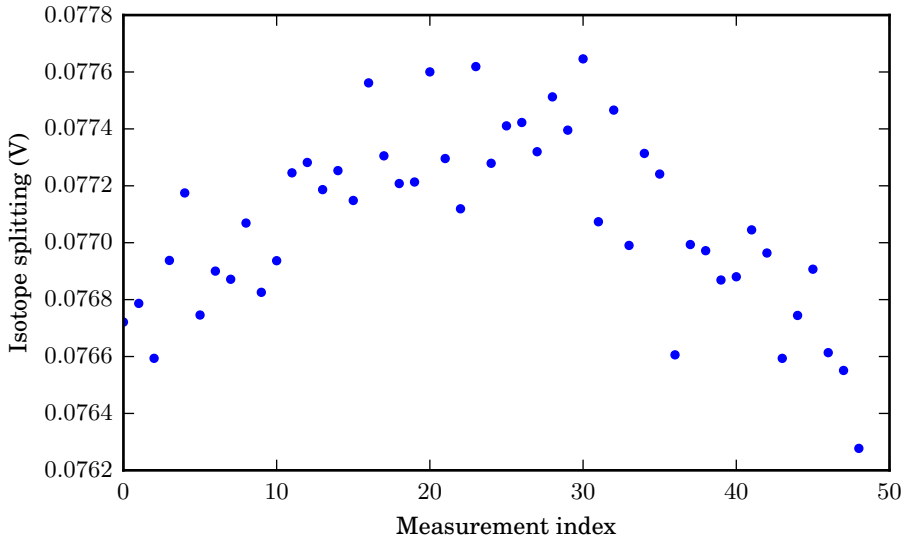

(b) Measurements of the relative isotope shift that were recorded in an alternating pattern with the Zeeman splitting.

Figure 2.5.7: Zeeman splitting (a) and relative isotope shift (b) as extracted form the spectra for each of the 50 measurements for one current value in the magnetic field coil.

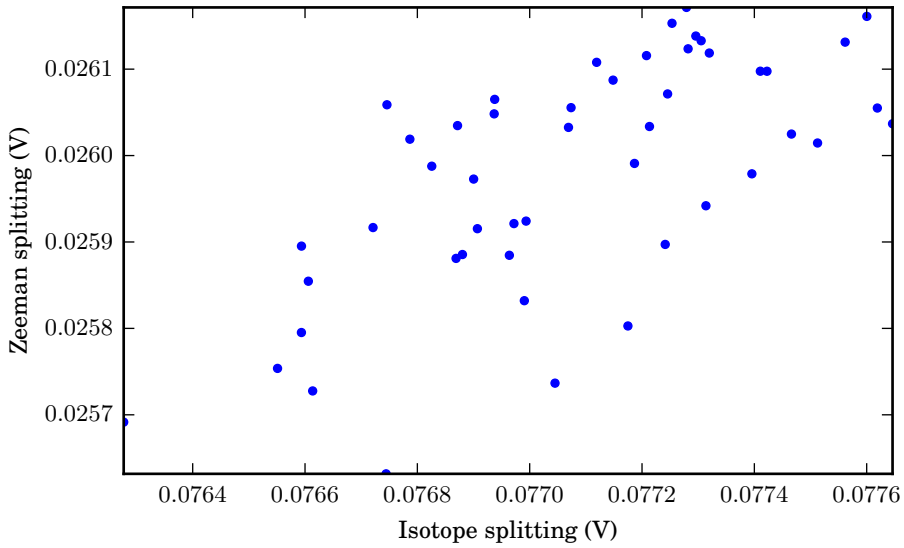

Figure 2.5.8: Relative isotope shift and Zeeman splitting as extracted from spectra that are recorded in an alternating pattern. Each point was measured without a magnetic field to determine the relative isotope shift. Then, the current was switched on and another spectrum was recorded to determine the Zeeman splitting.

$$\Delta\mathrm{IS}^{\mathrm{freq}}_{199-204} = \frac{m_{198}\cdot\Delta\mathrm{IS}^{\mathrm{freq}}_{198-201_{F=3/2}}}{m_{204}}. \tag{2.5.4}$$

To determine m_{198} and m_{204}, the results of the fits to the spectra that were recorded with the same current value i are averaged to obtain $Z^{V,i}_{198}$, $Z^{V,i}_{204}$, $\Delta\mathrm{IS}^{V,i}_{198-201_{F=3/2}}$ and $\Delta\mathrm{IS}^{V,i}_{199-204}$. In a next step, $Z^{i}_{198} = \frac{Z^{V,i}_{198}}{\Delta\mathrm{IS}^{V,i}_{198-201_{F=3/2}}}$ and $Z^{i}_{204} = \frac{Z^{V,i}_{204}}{\Delta\mathrm{IS}^{V,i}_{199-204}}$ are plotted against the current values i and fitted with a linear function with an offset. The resulting slopes are m_{198} and m_{204}.

2.5.2.3 *Uncertainties*

To determine the statistical uncertainties of the Z^{i}_{198} and Z^{i}_{204}, the correlations between the Zeeman splittings $Z^{V,i}$ and the Isotope splittings $\Delta\mathrm{IS}^{V,i}$ that were measured during the same time period have to be considered. Figure 2.5.8 shows a strong correlation for the measurement of Z^{i}_{204} for $i = 2.4\,\mathrm{A}$. The Bravais-Pearson-correlations for the different current values are given in table 2.5.1. To obtain the uncertainties of the $Z^{i} = \frac{Z^{V,i}}{\Delta\mathrm{IS}^{V,i}}$, the uncertainties $\delta Z^{V,i}$ and $\delta\Delta\mathrm{IS}^{V,i}$ are estimated by calculating the standard deviation of the 50 measurements for each current value. The uncertainties are then propagated considering the correlations between the consecutive isotope shift and Zeeman shift measurements using

$$\delta Z^{i} = Z^{i}\cdot\sqrt{\left(\frac{\delta Z^{V,i}}{Z^{V,i}}\right)^{2} + \left(\frac{\delta\Delta\mathrm{IS}^{V,i}}{\Delta\mathrm{IS}^{V,i}}\right)^{2} - 2\frac{\mathrm{cov}\left(\Delta\mathrm{IS}^{V,i}, Z^{V,i}\right)}{\Delta\mathrm{IS}^{V,i}Z^{V,i}}}. \tag{2.5.5}$$

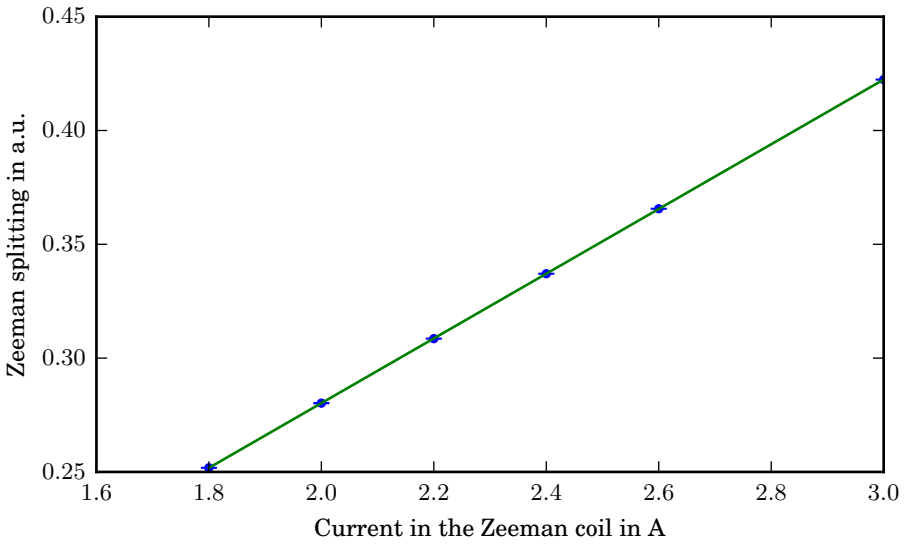

(a) Measured Zeeman splitting over the current in the field coil and linear fit.

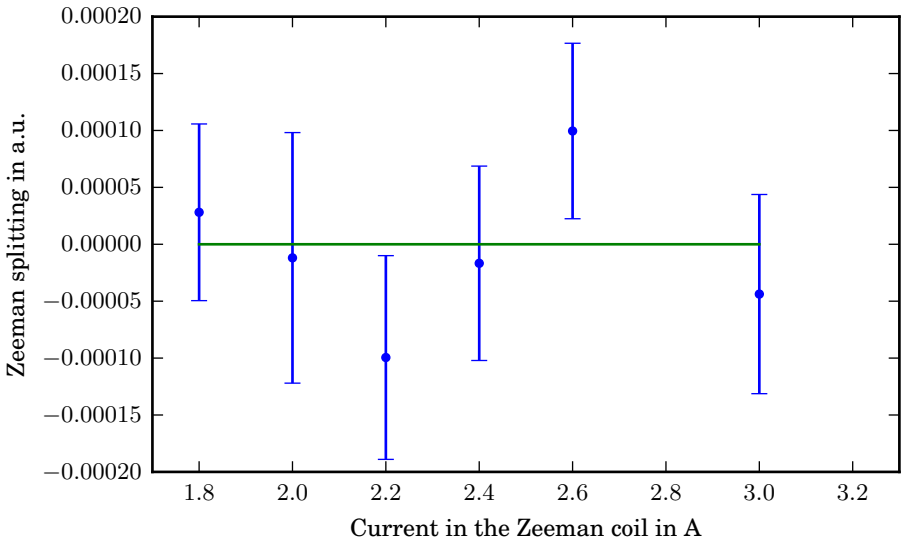

(b) Residuals of the fit that is shown in (a).

Figure 2.5.9: Fit to the Zeeman splittings in ^{204}Hg and residuals.

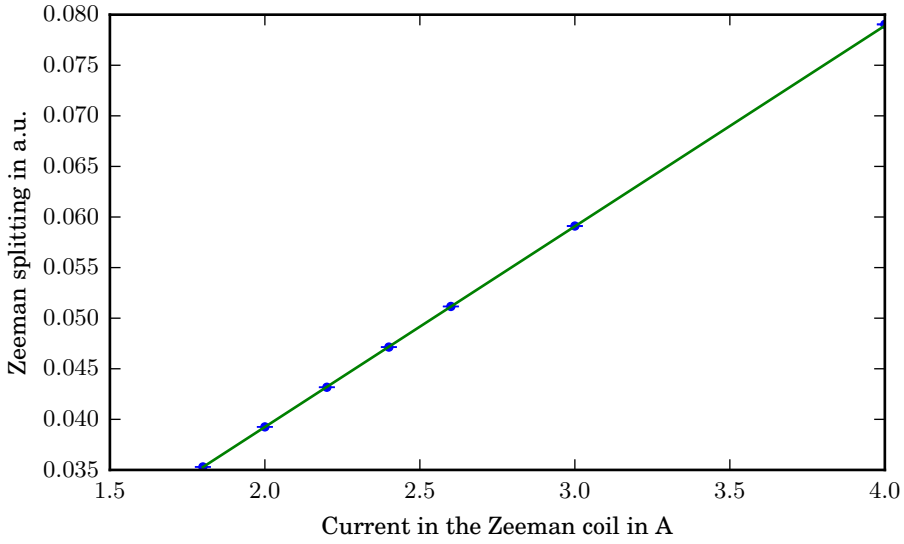

(a) Measured Zeeman splitting over the current in the field coil and linear fit.

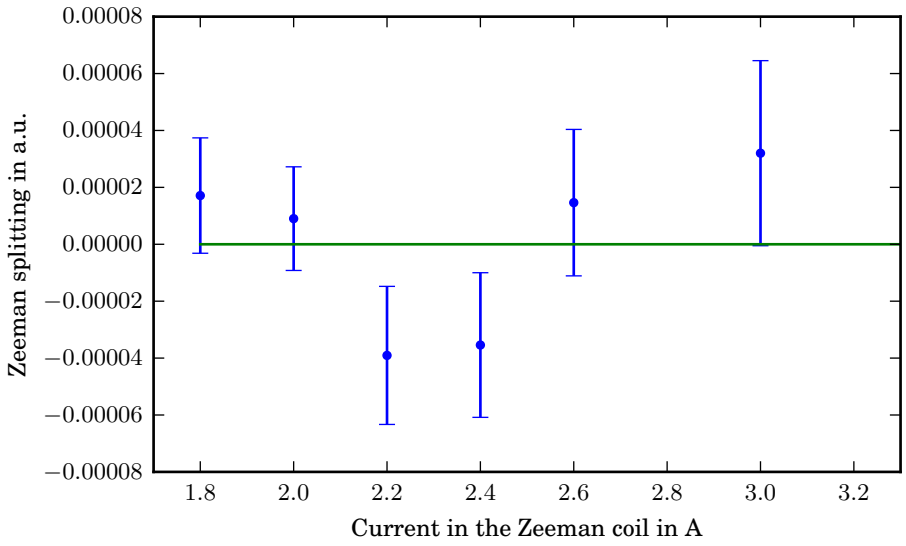

(b) Residuals of the fit that is shown in (a).

Figure 2.5.10: Fit to the Zeeman splittings in ^{198}Hg and residuals.

Current (A)	Correlation 204	Correlation 198
1.8	0.58	0.67
2	0.46	0.64
2.2	0.56	0.62
2.4	0.69	0.65
2.6	0.77	0.65
3	0.67	0.5

Table 2.5.1: Bravais-Pearson-Correlations between the simultaneous Zeeman- and Isotope splitting measurements. "Correlation 204" is the correlation between the measurements of the Zeeman splitting in ^{204}Hg and the corresponding measurements of the relative isotope shift between ^{204}Hg and ^{199}Hg, F=1/2. and "Correlation 198" is the same for the Zeeman splittings in ^{198}Hg and the isotope shifts between ^{198}Hg and ^{201}Hg, F=3/2.

Here, $\mathrm{cov}(\Delta\mathrm{IS}^{V,i}, Z^{V,i})$ is the covariance between $\Delta\mathrm{IS}^{V,i}$ and $Z^{V,i}$. The resulting Z^i and δZ^i are shown in figure 2.5.9 and figure 2.5.10. The least-squares fitting algorithm determining the slopes m_{198} and m_{204} uses these uncertainties to estimate the uncertainties δm_{198} and δm_{204} of the fit results. Uncertainties of the slopes are not correlated and contribute to the uncertainty of the final result according to

$$\sigma_{m_{198}} = \frac{\Delta\mathrm{IS}^{\mathrm{freq}}_{199-204}}{m_{198}} \cdot \delta m_{198} = 126.3\,\mathrm{kHz},$$
$$\sigma_{m_{204}} = \frac{\Delta\mathrm{IS}^{\mathrm{freq}}_{199-204}}{m_{204}} \cdot \delta m_{204} = 116.8\,\mathrm{kHz}$$

This leads to a statistical uncertainty of the frequency difference $\Delta\mathrm{IS}^{\mathrm{freq}}_{199-204}$ between the transitions to ^{199}Hg and ^{204}Hg of

$$\sigma_{\Delta\mathrm{IS}^{\mathrm{freq}}_{199-204}} = \sqrt{\sigma^2_{m_{198}} + \sigma^2_{m_{204}}} = 172.0\,\mathrm{kHz}. \tag{2.5.6}$$

This measurement procedure of $\Delta\mathrm{IS}^{\mathrm{freq}}_{199-204}$ relies on knowing the relative isotope shift between ^{198}Hg and ^{201}Hg (F=3/2), which, as already discussed above, was measured in [80] to be $\Delta\mathrm{IS}^{\mathrm{freq}}_{198-201_{F=3/2}} = (0.6763 \pm 0.0004)\,\mathrm{GHz}$. As the measurement compares two relative isotope shifts, this causes a systematic uncertainty of the final result for $\Delta\mathrm{IS}^{\mathrm{freq}}_{198-201_{F=3/2}}$ of

$$\sigma_{\Delta\mathrm{IS}^{\mathrm{freq}}_{198-201_{F=3/2}}} = \frac{\Delta\mathrm{IS}^{\mathrm{freq}}_{199-204}}{\Delta\mathrm{IS}^{\mathrm{freq}}_{198-201_{F=3/2}}} \cdot \delta\Delta\mathrm{IS}^{\mathrm{freq}}_{198-201_{F=3/2}} = 55.8\,\mathrm{kHz}. \tag{2.5.7}$$

2.5.2.4 *Result*

The result of the linear fit to the corrected Zeeman splitting in ^{204}Hg is $0.1422\,\mathrm{A}^{-1} \cdot I - 0.004\,12$, with the uncertainty of the slope being $0.000\,17\,\mathrm{A}^{-1}$. The fit is shown in figure 2.5.9a and the residuals of the fit in figure 2.5.9b. A linear fit to the Zeeman splitting in ^{198}Hg (shown in figure 2.5.10) yields $0.019\,83\,\mathrm{A}^{-1} \cdot I - 0.000\,415$, with the uncertainty of the slope being $2.7 \times 10^{-5}\,\mathrm{A}^{-1}$. Using equation 2.5.4, the resulting frequency difference $\Delta\mathrm{IS}^{\mathrm{freq}}_{199-204}$ is

$$94.30 \pm 0.17(\mathrm{stat.}) \pm 0.06(\mathrm{sys.})\,\mathrm{MHz}.$$

This is an improvement of about two orders of magnitude compared to the previously measured result from [80] (97 ± 17) MHz. It could still be improved by implementing a frequency shift that is well known in one of the two spectroscopy setups to get rid of the systematic uncertainty caused by the isotope splitting between ^{198}Hg and ^{201}Hg (F=3/2), and by recording more spectra or using a better readout for the spectral signals to reduce the statistical uncertainty. However, the calibration of the laser frequency that uses the relative isotope shift presented here is not the largest uncertainty in a mercury co-magnetometer in an nEDM experiment any more (see section 3.3.4.4).

However, repeating the isotope shift measurement using a known frequency offset is advised to validate this result with an independent measurement with different systematics. To do this, an acousto-optic modulator (AOM) can be used to shift the readout beam by a known frequency in one of the two spectroscopy setups. Shifting only the readout beam makes the power-loss in the AOM less critical.

2.5.3 MEASUREMENT OF THE DC STARK SHIFT IN A DOUBLE-SPECTROSCOPY SETUP

The Stark shift can cause shifts in the magnetic field measurement when mercury is used in EDM experiments as shown in section 3.3.4.1. The reason is that the electric field is typically applied only to the mercury vapor in the precession cell, but not to the atoms in the spectroscopy which are used as a reference for the laser frequency. One option to avoid this problem is to apply the same electric field to the spectroscopy as is used in the EDM measurement chamber.

As there was no experience with Doppler-free spectroscopy cells containing mercury vapor in equilibrium with liquid mercury that can apply a large electric field to the mercury vapor, a test cell was built with the goal of detecting a DC Stark shift to demonstrate that there is an electric field in the cell and that the spectroscopy is capable of resolving small shifts.

The DC Stark effect shifts the magnetometer transition because the $^3P_1$ and the $^1S_0$ levels are shifted differently by static electric fields. This differential Stark shift in ^{199}Hg has been measured to be $(-3.32 \pm 0.06)\,\mathrm{kHz}/(\mathrm{kV/cm})^2$ [56]. For the first time, a laser was used for a Stark shift measurement in mercury in this experiment. The result was achieved with Doppler-broadened spectroscopy signals and calibration of the frequency axis with a well defined frequency shift that was produced by mirrors in the laser beam that move forth and back with a known velocity.

This chapter shows a measurement using a Doppler-free spectroscopy to resolve the Stark shift. The calibration of the x-axis uses the frequency difference between the two isotopes ^{199}Hg and ^{204}Hg. A measurement of this differential isotope shift which makes this calibration more accurate is shown in the previous chapter.

2.5.3.1 *Spectroscopy cell with electrodes*

A quartz cuvette [2] with a 5 mm free path between the optical windows was modified for the purpose of this measurement. The profile of the inner volume is rectangular with the dimensions 1 mm times 5 mm. The side walls were removed from the cell by grinding, and vacuum-suited heat-resistant epoxy was applied to the edges of the remaining cell (see figure 2.5.11). The electrodes were made from commercially available cylindrical quartz windows with a diameter of two inches. They were cleaned and nickel-molybdenum was sputtered on one side of each electrode using a sputtering machine that was designed for coating components for the nEDM experiment [84]. These electrodes were glued to the cell body with the conductive surfaces facing each other (see figure 2.5.12). To apply high voltage, copper clamp connectors were designed to connect the high voltage cables to the nickel-molybdenum surface of the electrodes at a point as far away as possible from the spectroscopy cell.

While being heated in an oven, the cell was evacuated through a glass valve that was attached to the cell stem by melting. This worked well to get the cell clean initially. However, it got dirtier after some weeks of operation. The advantage of using a valve is that, if a high voltage breakdown releasing dirt into the cell occured, it could easily

2 FireflySci, Precision Cells Type 61 Standard Cuvette with Graded Seal Tube

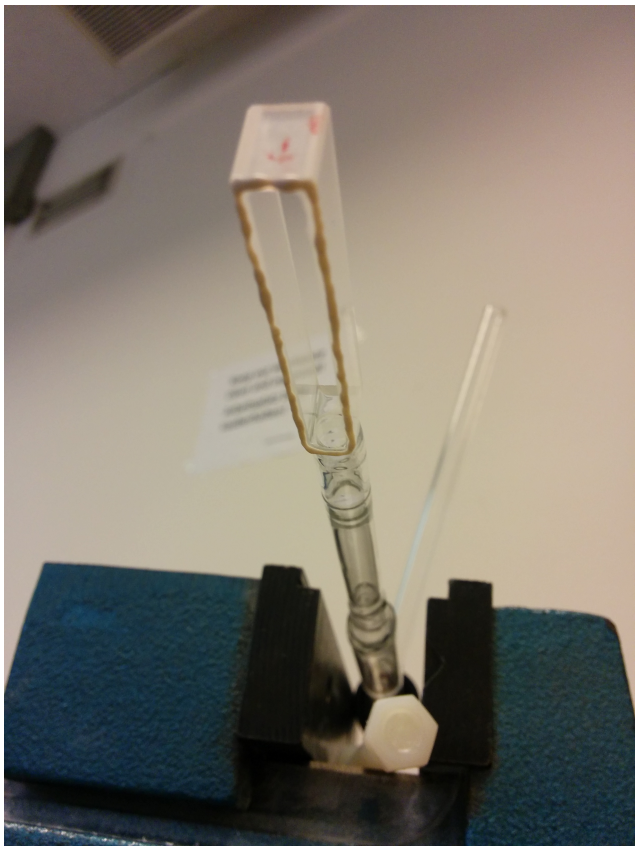

Figure 2.5.11: Spectroscopy cell with a valve attached (pointing down) and two faces removed. Glue is already applied to one side of the cell.

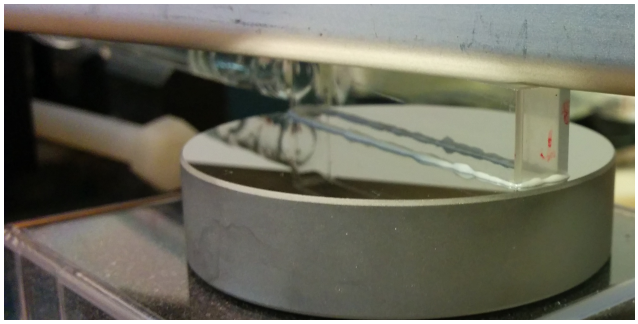

Figure 2.5.12: Spectroscopy cell being glued to one of the two nickel-molybdenum coated quartz electrodes. The width of the remaining optical windows of the cell is 1 cm.

be cleaned again. However, for a cell that needs to be working reliably for months or years, instead of using a valve, the cell stem should be sealed off with a torch.

2.5.3.2 *Optical setup*

By splitting up the laser beam further and copying the spectroscopy setup on the optical breadboard, two spectroscopic signals could be recorded at the same time, sharing the same laser light. One signal is recorded in the cell with the electrodes (Stark cell), the other one in a normal spectroscopy cell without an electric field (reference cell). This allows resolving signal shifts which are smaller than the typical drift of the laser wavelength between two measurements. Polarization spectroscopy (see section 2.3.2) was chosen for this measurement since this technique provided the best SNR.

Without applying a strong magnetic field to the cell, the residual earth magnetic field would define the relative alignment between magnetic and electric field. While this alignment is not important for the scalar Stark shift, it does matter for the tensor Stark shift as described in section 1.3.2.2.

To give the magnetic field in the Stark cell a well defined direction and to make sure that the $\sigma^+$and the σ^- transitions are both shifted (as expected for the Stark shift), a magnetic field was applied to the Stark cell parallel to the direction of the laser beam. This means that the electric and the magnetic field are oriented perpendicular. Although they would be parallel in an EDM experiment, this does not make a difference for the magnetometer transition in ^{199}Hg as the tensor Stark shift does not contribute to this transition, and the scalar Stark shift does not depend on the relative alignment of electric and magnetic field (see section 1.3.2.2). The magnetic field strength was chosen such that it was large enough to resolve both transitions in distinct features. In the reference cell, no magnetic field was applied as this makes the fit model simpler and the amplitude of the signal larger.

2.5.3.3 *Signal*

The preparation beam was circularly polarized, and the angle of the analyzer cube with respect to the original polarization axis of the readout light was chosen such as to get Doppler-free signals without a dispersive component (see figure 2.5.13). Details on how to choose this angle can, for example, be found in [82] and [85].

In order to accurately determine the positions of the peaks as accurately as possible, the signal was fitted with a Gaussian background and a Voigt peak for each feature. As there are many free parameters in this model and the fit needed to be applied to 250 data sets, a reliable parameter guessing was important.

The fitting procedure is described in section 2.5.1. Figure 2.5.14 shows the raw data with the fit of the full model and the peaks as found by the parameter guesser.

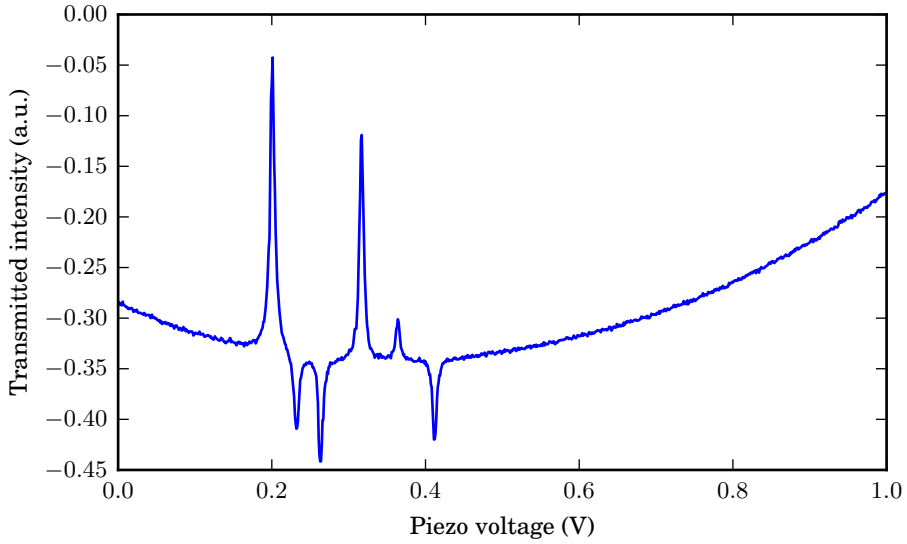

Figure 2.5.13: Typical raw signal of the DC-Stark measurement. On the Doppler-broadened background, Zeeman-split Doppler-free features caused by ^{199}Hg, F=1/2 and ^{204}Hg are observed.

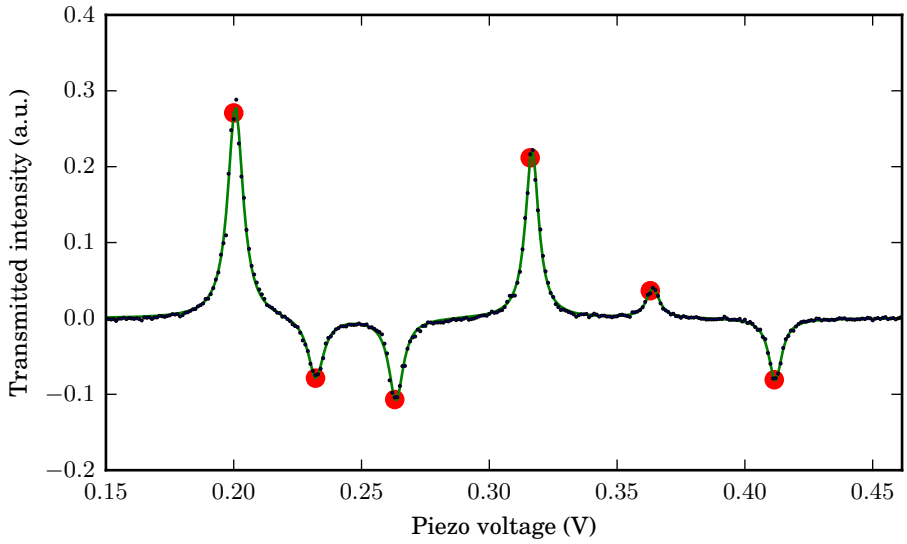

Figure 2.5.14: Zoom to a typical signal in the DC-Stark shift measurement. The raw signal is shown in blue, the result of the fit in green, and the peaks as they were guessed by the parameter-guessing are shown as red dots.

2.5.3.4 *Results*

For each out of five different voltages, 50 spectra were recorded. The distance between the peaks caused by the isotopes ^{199}Hg and ^{204}Hg in each spectrum was used to calibrate the frequency axes. To determine the corresponding conversion factor, the voltage distance between the ^{199}Hg and the ^{204}Hg features in the recorded spectra was determined and divided by the frequency difference of the two features. A measurement of this frequency difference is shown in section 2.5.2.

Computing the difference between the positions of the peaks in the Stark cell and the peaks in the reference cell then provided the shift that is caused by the electric field. Since the same laser is used to drive both spectroscopy setups simultaneously, fluctuations of the laser frequency are canceled. As the fit did not converge correctly in some cases, results that deviated more than 3σ from the median values of each voltage setting were dismissed.

Figure 2.5.15 shows the resulting shift plotted against the Voltage applied to the Stark cell. Both isotopes are shifted by the scalar Stark shift, but only the ^{204}Hg transition is additionally shifted by the tensor Stark shift. The tensor Stark effect shifts the σ^+ and the σ^- features in ^{204}Hg by the same amount and in the same direction, which is opposite to that of the scalar Stark shift.

This reduces the overall shift of the ^{204}Hg transition by an amount depending on the relative alignment of the electric and the magnetic field. In section 1.3.2.2, it was shown that the tensor Stark shift scales with the angle β between the electric and magnetic field as

$$\Delta E_{\text{Stark}} = \varepsilon^2[-\frac{1}{2}\Delta\alpha_0 - \Delta\alpha_2(2-3\cdot\sin^2(\beta))\cdot Y]. \tag{2.5.8}$$

Here, $\Delta\alpha_0$ and $\Delta\alpha_2$ are the differences between the polarizabilities of the excited state $^3P_1$ and the ground state $^1S_0$, ϵ is the electric field, and Y is the factor containing the information on the hyperfine state as defined in section 1.3.2.2.

For the ^{199}Hg transition, $Y = 0$ for both magnetic sub-levels and the total shift of both transitions is

$$\Delta E_{199} = -\varepsilon^2\frac{1}{2}\Delta\alpha_0. \tag{2.5.9}$$

Fitting a quadratic model to the measured shifts of the ^{199}Hg states, provides a result for the scalar Stark shift α_0.

When the magnetic holding field and the electric field which causes the Stark shift are perpendicular as in this setup, the factor $(2-3\cdot\sin^2(\beta))\cdot Y$ for the tensor Stark shift α_2 is $\frac{1}{4}$ for the ^{204}Hg transition and the total Stark shift is

$$\Delta E_{204} = \varepsilon^2[-\frac{1}{2}\Delta\alpha_0 + \frac{1}{4}\Delta\alpha_2]. \tag{2.5.10}$$

If the electric and magnetic fields were parallel to each other, the factor in front of $\Delta\alpha_2$ would be $-\frac{1}{2}$.

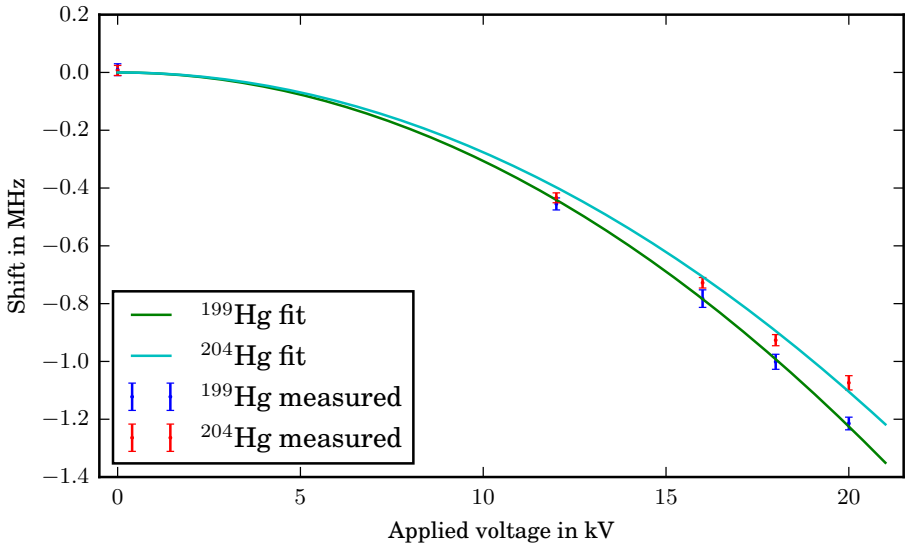

Figure 2.5.15: DC Stark shift of the $^1S_0 \rightarrow {}^3P_1$, $F = \frac{1}{2}$ transition in the isotopes ^{199}Hg and ^{204}Hg. The tensor Stark shift is different for the two isotopes.

The quadratic fits in figure 2.5.15 result in $-3.150 \pm 0.123\,\mathrm{kHz/kV^2}$ for the ^{199}Hg and in $-2.840 \pm 0.111\,\mathrm{kHz/kV^2}$ for the ^{204}Hg transition. Here, the uncertainties are only taking into account the statistical accuracy of the measured shifts.

However, the largest uncertainty in the measurement is the electric field. The spectroscopy cells are ground by hand and the electrodes are glued to the cell manually. Assuming an accuracy of 0.3 mm for the distance of the electrodes of 1 cm, this leads to a systematic uncertainty of the measured relative Stark shifts of

$$-3.150 \pm 0.123(\mathrm{stat.}) \pm 0.197(\mathrm{sys.})\,\mathrm{kHz/kV^2} \tag{2.5.11}$$

for ^{199}Hg, and

$$-2.840 \pm 0.111(\mathrm{stat.}) \pm 0.163(\mathrm{sys.})\,\mathrm{kHz/kV^2} \tag{2.5.12}$$

for ^{204}Hg.

Additionally, the electric field can be disturbed by the quartz windows. As this measurement was designed to demonstrate that the Stark shift can be accounted for in spectroscopy (and thus the frequency lock of the laser), and not to determine the Stark constants with increased accuracy, no extensive electric field simulations were performed to investigate this effect. The observed shifts of both isotopes are somewhat smaller than expected from the literature values for α_0 and α_2. A likely cause of this could be that the electric field was smaller than than expected.

However, the ratio of the measured shifts $\frac{\Delta E^{meas}_{204}}{\Delta E^{meas}_{199}} = 0.90 \pm 0.05$ is in accordance with the values from [56, 57] $\frac{\Delta E_{204}}{\Delta E_{199}} = \frac{0.5\alpha_0 - 0.25\alpha_2}{0.5\alpha_0} = 0.88 \pm 0.01$. This value is independent from the electric field, and the fact that it agrees with the literature values supports the above assumption that the electric field is smaller than expected.

However, this measurement shows that it is feasible to construct a Doppler-free spectroscopy cell with electrodes, with the electric field inside the cell being proportional to the applied voltage. This can be used to compensate the Stark shift in an experiment with electric fields using a spectroscopy as a reference for the laser frequency. Additionally, it demonstrates the feasibility of measuring small shifts of atomic lines with Doppler-free spectroscopy when an additional Doppler-free reference setup is used.

In contrast to the previous measurements of the differential Stark shifts in mercury, the technique described here uses Doppler-free spectroscopy. This allows a clear distinction between the contributions of the different isotopes without having to use isotopically purified mercury samples. More importantly, the different hyperfine transitions of each isotope are resolved completely and do not contribute to the measurement of each other's differential Stark shifts [56].

Part 3

MAGNETOMETRY

3.1 MERCURY MAGNETOMETRY IN EDM EXPERIMENTS

Mercury co-magnetometry was a major improvement in accuracy for experiments searching for an EDM in neutrons. The first nEDM experiments with UCNs already used magnetic shielding and stable current sources [71, 86]. The UCNs were stored in material bottles and Ramsey's method of separated oscillatory fields was used to measure the difference between their precession frequencies in parallel and anti-parallel magnetic and electric fields. However, there was no way to measure fluctuations of the magnetic field independently, and so, the uncertainties of the result were dominated by these fluctuations.

With a first mercury co-magnetometer, a new upper limit for the nEDM was set by correcting the UCN frequency measurements for fluctuations of the magnetic field detected with the mercury magnetometer [46, 87]. The vapor was polarized with a discharge lamp in a pre-polarizer chamber inside the magnetic shielding and then released into the precession chamber that was filled with a new bunch of UCNs. The mercury vapor was polarized parallel to the magnetic field just like the UCNs. So, in order to start the Ramsey cycle, the magnetization of both particle ensembles had to be flipped to the precession plane. That was done using two individual field flips for each species that affected the other species only marginally [21].

Although the idea was to confine both species in the same chamber in order to expose them to the same average magnetic field, it turned out that the average height of the UCNs, which are not in thermal equilibrium with the walls of the precession chamber, was a little lower than that of the mercury vapor. This small offset between the different average heights the field was measured at, limited the capability to correct the neutron frequency measurements for fluctuations of the magnetic field. Furthermore, geometric phases that are covered in section 3.3.2 started to dominate the uncertainty of the results [88].

A new method to analyze data taken with UCNs and mercury took advantage of the different distributions of the two species in the precession chamber [89]. It extracts the average vertical gradient during a Ramsey cycle from the two measurements of the magnetic field at different average heights. As the geometric phase effect scales linearly with the vertical magnetic field gradient, while an effect caused by an nEDM is independent from this gradient, the two effects can now be separated in the analysis [89]. With this technique, the upper limit on the nEDM was found to be 3.0×10^{-26} ecm (90% CL) in the Sussex experiment [24].

3.2 MAGNETOMETRY OVERVIEW

3.2.1 PHYSICS OF POLARIZATION, PRECESSION AND READOUT OF MERCURY VAPOR

In the Sussex experiment, the mercury vapor was polarized longitudinally. A dedicated polarization cell was close to, but outside the precession chamber. This made it possible to polarize a new bunch of atoms while the last ones are measuring the magnetic field. A discharge lamp produced the pumping beam with a circular polarization. The light then traversed the pre-polarization chamber parallel to the magnetic holding field. Due to the spin dependence of the probability to absorb a photon (see section 1.3.1), only atoms in one Zeeman state can absorb the polarization beam. By doing so they are transfered to the other Zeeman state where they do not absorb the polarizing light anymore.

With the magnetic field pointing in z-direction, the Zeeman states the atoms can be aligned to, $m_F = +1/2$ and $m_F = -1/2$, can be written $|+\rangle_z$ and $|-\rangle_z$. The notation in this chapter follows [52].

When the degree of polarization of the vapor has reached equilibrium, only atoms that were depolarized in a collision with the walls or other particles in the chamber are affected by the light. How fast the equilibrium polarization is reached primarily depends on the power of the polarizing light. Today, lasers can produce appropriate pumping beams with several 10 mW.

With these, the mercury vapor can be polarized using transverse optical pumping [90] which eliminates the need of alternating magnetic fields in mercury magnetometry. To do this, the circularly polarized beam is chopped such that pulses of light traverse the vapor perpendicular to the magnetic field B_0 with a rate that is synchronized with the mercury Larmor frequency $\omega_L = \gamma_L \cdot B_0$. Every time a pulse of photons that are moving in x-direction are absorbed by the mercury vapor, a bunch of atoms is prepared such that their spin points in $|+\rangle_x$ (or $|-\rangle_x$) direction. These can be written as a superposition of the up and down states given above, as

$$|+\rangle_x = \frac{|-\rangle_z + |+\rangle_z}{\sqrt{2}} \tag{3.2.1}$$

$$|-\rangle_x = \frac{|-\rangle_z - |+\rangle_z}{\sqrt{2}}. \tag{3.2.2}$$

In nEDM experiments, the mercury vapor can be polarized while the UCNs are filled into the precession cell (20 s to 30 s), which facilitates the optical pumping process. The duty cycle of the optical pumping can then be optimized to reach a high degree of equilibrium polarization as described in [70].

For a time independent Hamiltonian H, the time evolution of a quantum mechanical state is

$$|\Psi(t)\rangle = e^{\frac{-iHt}{\hbar}} |\Psi(0)\rangle . \tag{3.2.3}$$

As the holding field B_0 shifts the states $|+\rangle_z$ and $|-\rangle_z$ by $\pm\frac{\gamma}{2}B_0 = \pm\frac{\omega_0}{2}$, the time evolution of an atom that was prepared in $|+\rangle_x$ is

$$|\Psi(t)\rangle = \frac{e^{i\omega_L t/2}|-\rangle_z + e^{-i\omega_L t/2}|+\rangle_z}{\sqrt{2}}. \tag{3.2.4}$$

When a readout beam is sent through the vapor in x-direction, it measures the probability of the state $|\Psi(t)\rangle$ to be found in x-direction. Due to the different frequencies in the phase factors of the two pure z-states in equation 3.2.4, the probability to measure the atom in x-direction is modulated with the Larmor frequency ω_L.

Repeating the polarizing light pulse every time the magnetization has made a full turn and the $|+\rangle_x$ state is restored adds more atoms to the ensemble of polarized atoms. Polarizing the vapor longitudinally in one of the pure spin states $|+\rangle_z$ or $|-\rangle_z$ and then flipping the magnetization to the precession plane results in the same precession as preparing the atoms directly in the mixed state.

An advantage of transverse optical pumping over longitudinal polarization is that no pre-polarizing chamber is needed inside the shield and that no field flip has to be applied that could potentially impair the spatial or cycle-to-cycle homogeneity of the Ramsey cycle that is used to measure the precession frequency of the UCNs.

3.2.2 DECAY OF THE SIGNAL

An ensemble of polarized atoms experiences several mechanisms that reduce the degree of polarization. The depolarization rates of these mechanisms are proportional to the polarization and thus lead to an exponential decay. The four leading relaxation mechanisms $T_{1,\text{mag}}$, $T_{2,\text{mag}}$, T_{wall}, and T_{light} are sketched out in the following with a focus on mercury co-magnetometry in an nEDM experiment.

A relaxation mechanism that is present for both, stationary longitudinal (parallel to the magnetic field) polarized atoms and precessing perpendicularly polarized atoms, is the relaxation rate $T_{1,\text{mag}}$. The spins of particles like ^{199}Hg atoms that move fast in a small magnetic field can not follow the magnetic field lines adiabatically. In a short free flight such a spin accumulates a small angle to the magnetic field lines. As the atoms are diffusely reflected when they hit the cell walls or other atoms in the cell, each free path between the reflections is independent of all other paths and the angles accumulated by summing up all free paths are independent and identically distributed random variables (IIDs) forming a random walk.

A rough estimation of the expected depolarization time can be made using (see chapter A)

$$\frac{1}{T_1} = \frac{\langle \Delta B_T \rangle^2}{B_0^2} \cdot \frac{\bar{l} \cdot v_{\text{th}}}{4}. \tag{3.2.5}$$

Here, the average magnetic field with the magnitude B_0 points in $z-$direction and $\langle \Delta B_T \rangle$ is the average change of the transverse component of the magnetic field during a free flight of an atom through the cell. The average free path through the cell is $\bar{l}$ and the average velocity of an atom is v_{th}.

This is only a rough estimation that can be used if the magnetic field inhomogeneities are dominated by well known gradients. In [91] is shown how the $T_{1,\mathrm{mag}}$ time for more advanced field configurations can be calculated.

A second depolarization mechanism that is present for longitudinal and transversal polarization is caused by atoms sticking to the wall for short periods of time in local magnetic fields that differ from the holding field B_0. The corresponding relaxation time T_{wall} depends on the surface material. Different wall coatings were tested [92, 93] to achieve long T_{wall} times with mercury vapor. For most materials, $1/T_{\mathrm{wall}}$ will dominate the relaxation rate which demands a careful choice of the wall coating material and a clean precession cell. While this is easier in a dedicated magnetometer cell than in a co-magnetometer, [21] shows that sufficient T_{wall} times can also be achieved in a mercury co-magnetometer in an nEDM experiment.

Precessing atoms additionally experience a relaxation $T_{2,\mathrm{mag}}$ of the ensemble polarization because the atoms are exposed to different average magnetic fields due to the different random paths they take during the precession time. In the high pressure regime where single atoms only diffuse through a small fraction of the cell, this is a large effect as the phase between two atoms that are in different field regions grows linearly with the precession time. However, in the small pressure regime all atoms map approximately the same volume on different, random, paths. This motional narrowing leads a smaller relaxation as the phase each spin accumulates relative to the ensemble-average can again be modeled with a random walk. The central limit theorem states that after N steps in a random walk, the phases of the spin ensemble will be Gaussian distributed with the width $\sigma \propto \sqrt{N}$, or, for a continuous random walk after the time t: $\sigma \propto \sqrt{t}$. More details on the $T_{2,\mathrm{mag}}$ time can be found in [94] and [91].

The vertical and longitudinal decay of the polarization does not always lead to a Gaussian spin distribution. If the particles are not in thermal equilibrium with the cell walls or if they are not reflected diffusely but specularly, the independence of the single steps in a random walk is not necessarily given anymore. The resulting distribution of the spins is then better described by a Tsallis distribution then by a Gaussian. This has been tested in numerical simulations for different conditions and particles [95]. While any static projection measurement of a spin ensemble is not sensitive to the shape of the spin distribution but only to its average, it is possible to detect the evolution of the q-value in a Tsallis distribution in the envelope of a continuous projection measurement signal of a free precession decay. In the case of a purely Gaussian[1] broadening of the distribution, the envelope of the projection signal is an exponential function. However, if the spin distribution is described by a Tsallis distribution that gains a higher q-value additionally to the broadening during the decay, the shape of the envelope function is not purely exponential anymore.

1 The Gaussian distribution is a special case of the Tsallis distribution. .

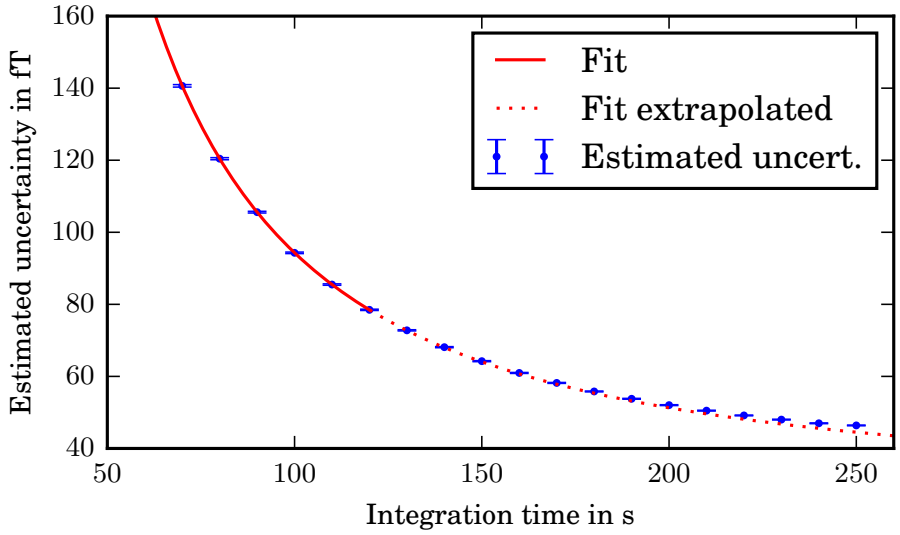

Figure 3.2.1: Accuracy of the magnetic field measurement over the averaging time extracted from real data. The decay time of the recorded signals was ~120 s. This measurement was done with the magnetometer described in chapter 3.4, but with an older version of the power stabilization that only reduced power fluctuations for small frequencies (to prevent a drift of the laser power).

The relaxation $1/T_{\text{light}}$ of the polarization due to resonant ultra violet (UV) light depends on the absorption rate which is determined by the laser intensity, the ^{199}Hg density, and the relative alignment between the polarization and the laser beam. To measure T_{light}, identical polarization procedures are used in a series of measurements that monitor the decay of the polarization with switching off the readout beam for different time periods during the decay. T_{light} is typically small for readout intensities <1uW. To measure T_{wall}, the relaxation can be measured in different field gradients and with known, or without, depolarization due to the readout light. Then, T_{wall} can be extrapolated from the results. To distinguish between $T_{2,\text{mag}}$ and $T_{1,\text{mag}}$, the relaxation has to be measured in transversely polarized, precessing, atomic vapor and in longitudinally polarized vapor.

3.2.3 FUNDAMENTAL SENSITIVITY OF AN ATOMIC VAPOR MAGNETOMETER

The theoretical statistical accuracy an idealized atomic vapor magnetometer with N particles can achieve is [52]

$$\delta B_{\text{SNL}} \approx \frac{1}{\gamma}\sqrt{\frac{\Gamma_{\text{rel}}}{N\tau}}. \tag{3.2.6}$$

Where Γ_{rel} is the relaxation rate of the particles and τ is the averaging time of the field measurement. This theoretical model assumes a noise-free readout of the atomic magnetization and that there are no systematic or statistic effects that falsify the measurement, which is not possible in reality. The most fundamental noise source in this

system is shot noise. The uncertainty of extracting the magnetic field strength from fitting the frequency of a decaying sinusoidal signal with the initial signal-to-noise ratio (SNR) S_n is given by the Cramer-Rao lower bound (CRLB) [36, 75]

$$\delta B \geq \frac{\sqrt{12}}{S_n \cdot T^{3/2} \gamma_{Hg}} \cdot \sqrt{C}, \tag{3.2.7}$$

with the observation time T and the gyromagnetic ratio γ_{Hg} of ^{199}Hg. The factor $\sqrt{C}$ is 2.17 for a polarization decay time of 100 s and a sampling rate of 100 Hz as chosen in [75]. If the noise is dominated by the photon shot noise and the signal amplitude is 8% of the readout beam intensity, the SNR is given by $S_n = 0.08 \cdot \sqrt{\dot{N}}$ with $\dot{N}$ being the photon rate. For a readout beam with 10 µW, the CRLB is

$$\delta B = 3 \cdot 10^{-16} T. \tag{3.2.8}$$

When the mercury magnetometer is used in an nEDM experiment, this translates to the uncertainty of the nEDM result as

$$d_n = 1 \times 10^{-27}\, e\,\text{cm}.$$

As the uncertainty is statistical and uncorrelated, it can be reduced by a factor of $\sqrt{N}$ by repeating the measurement N times.

A detailed description of key components that are designed to keep statistical and systematic uncertainties small is given in chapter 3.4. A discussion of systematic effects in mercury magnetometry is presented in chapter 3.3.

The dependence of the accuracy of a field measurement on the averaging time in real data is shown in figure 3.2.1. A free precession decay was recorded for 250 s and the precession frequency was extracted using fits to subsets of the data that start at the beginning of the decay and average over different time intervals. For each fit, the uncertainty of the magnetic field measurement is estimated based on the variance of the fit results (for details of the fit procedure, see [96]). This was done for 10 successive decays and the results were averaged. To achieve a long polarization lifetime in the small precession cell that was used (see figure 3.5.2), the readout power was reduced to <250 nW. The fit to the first six data points in figure 3.2.1 scales with $T^{-\frac{3}{2}}$ and shows that the uncertainty follows the CRLB (see equation 3.2.7). However, for averaging times >200 s, the estimated uncertainty is slightly higher than expected from the fit which is likely caused by a drift of the magnetic holding field.

3.2.4 MAGNETOMETER SETUP

The light emitted from the laser that was described in section 2.2.1 has some imperfections that need to be addressed to make it better suited for measurements of the magnetic field inside the magnetically shielded room (MSR). Section 3.4.1 describes

the efforts to fine tune and stabilize the frequency of the laser light and the importance of this stabilization is shown in section 3.3.1.

As the power fluctuations of the laser beam dominate the noise of the magnetometer signal when the laser is running freely [96], a feedback is implemented to stabilize the total power of the beams that feed the frequency lock and the magnetometer itself. Further details on this are presented in section 3.4.3.

Another challenge in the magnetometer setup comes with the divergence of the laser beam. As the magnetometer is designed to work without optical fibers, the readout beam has to travel more than 5 m from the laser source to the optical readout on the other side of the MSR.

To measure the shape of the beam at different positions, a razor blade was driven through it in radial direction with a micrometer screw, and the power that passed by the razor blade was measured at every step [97].

Mapping the shape at different distances from the laser source provides a picture of the divergence of the beam. It turned out that the laser beam profile is elliptical and diverges differently in the directions of the two semi axes of the ellipse. One of these axes showed a convergence with around $470\,\mu m\,m^{-1}$ as the beam leaves the laser, and along the other axis, the beam was diverging with $240\,\mu m\,m^{-1}$. Fig 3.2.2 shows the measurement of the widening component. For more details, see [97]. As it is crucial that no readout light is cut off on its way to the photo diode, the readout setup was designed to have a large optical aperture (see section 3.4.2). To additionally reduce the divergence, a beam shaping setup was introduced. A good solution for this turned out to be the combination of two cylindrical lenses and a telescope with spherical lenses.

Figure 3.2.3 shows a schematic drawing of the laser setup for a magnetometer measurement. To be able to adjust the angle and the transverse position of the beam, two adjustable mirrors are placed between the laser and the beam shaping setup. A small fraction of the beam is then split from the main beam with a non-polarizing beam splitter to feed the power-lock setup.

The main beam is split again multiple times with polarizing beam splitter cubes preceded by $\lambda/2$ plates to feed the spectroscopy setup and to generate a strong polarization beam and a weak readout beam. These are sent through mechanical shutters to switch the two beams on and off selectively and to generate the pulsed beam that is needed for transverse optical pumping as described in section 3.2.1.

After having passed a $\lambda/4$ plate to circularly polarize them, the two beams are sent upwards vertically from the optical table. A second breadboard mounted vertically in front of the holes that go through the shielded room (see section 3.5 for more details on the MSR) carries more adjustable mirrors that reflect the beams into the shielded room. Both beams traverse the vapor cell, and while the readout beam is aimed to hit the readout as centered as possible, the pumping beam should miss the photo diode to avoid excessive electronic saturation. The readout is described in more detail in section 3.4.2.

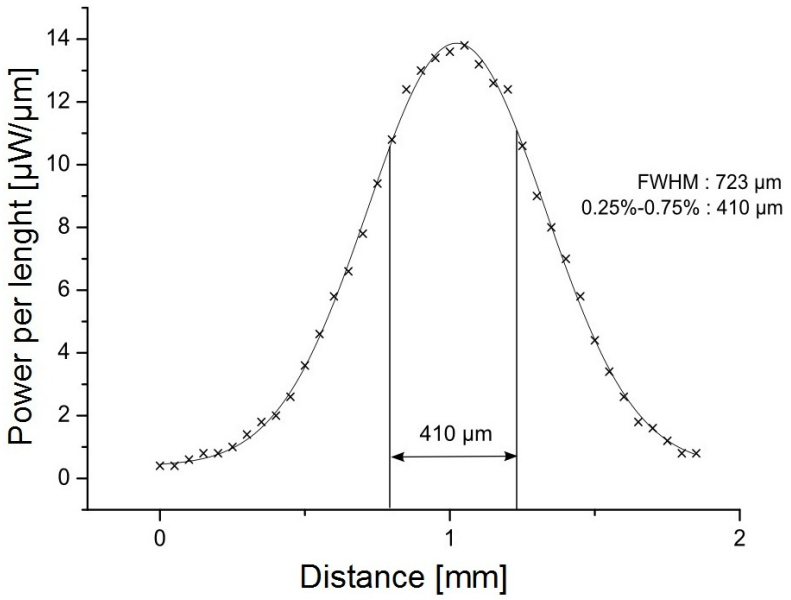

(a)

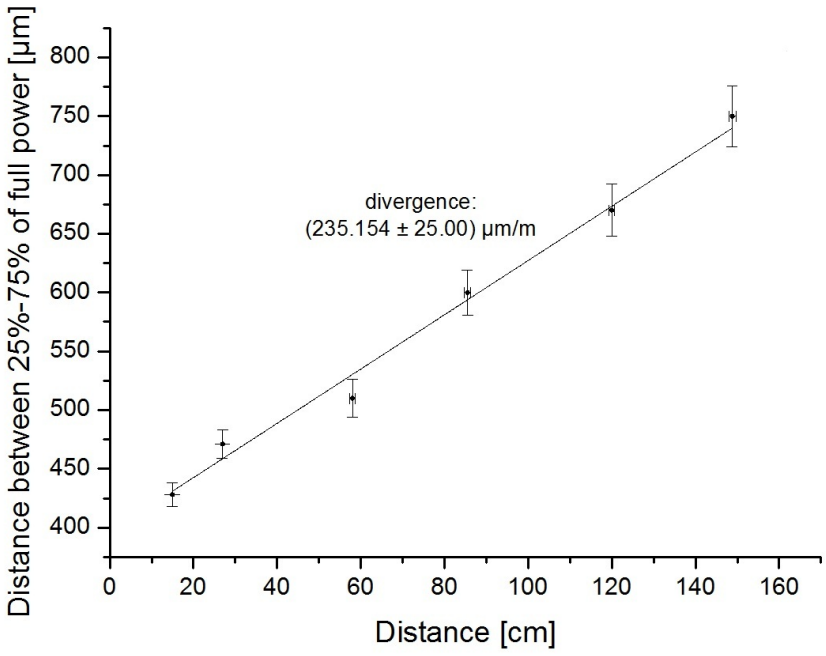

(b)

Figure 3.2.2: Measurement of the beam divergence. A razor blade is driven through a laser beam in radial direction with a micrometer screw and the intensity that can pass the blade is measured at different blade-positions and plotted over the position as shown in (a). This is done at different positions along the laser beam to determine the divergence as shown in (b). The figures are taken from [97].

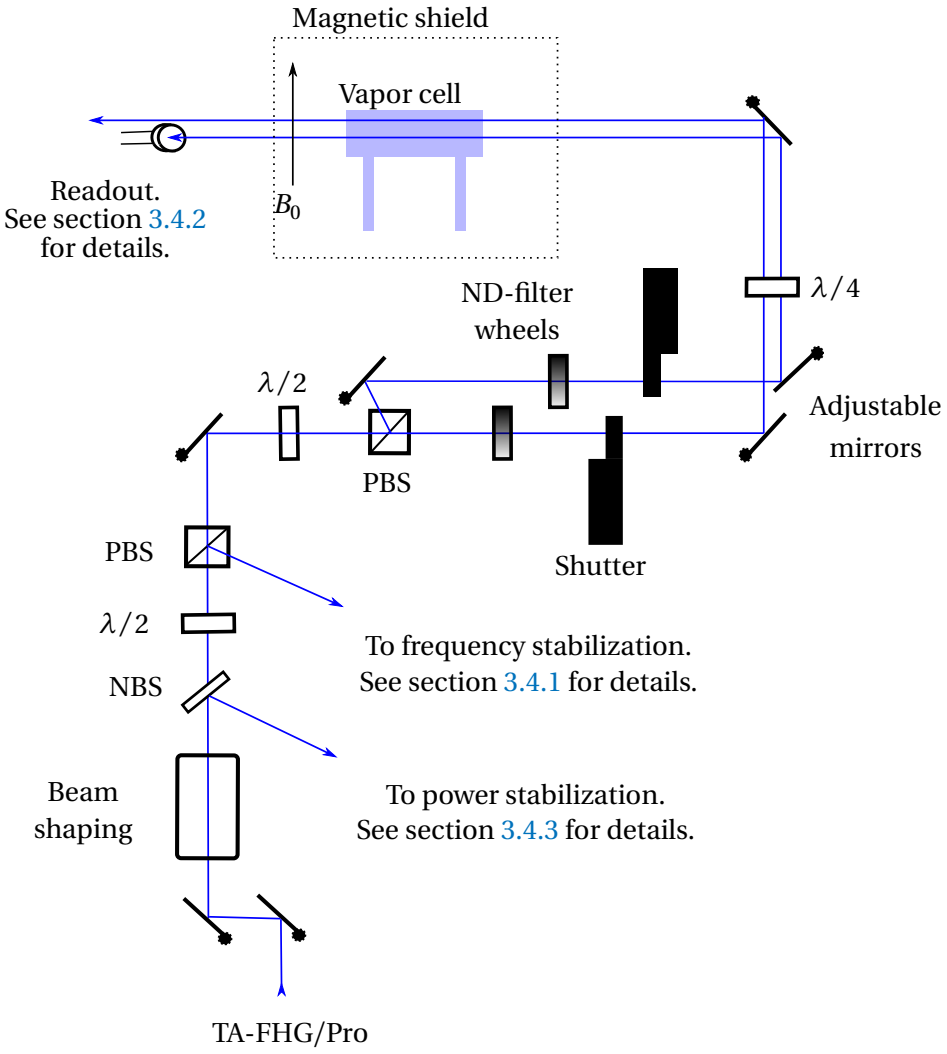

Figure 3.2.3: Schematic of the mercury magnetometer setup. PBS: Polarizing beamsplitter cube. NBS: Non-polarizing beam splitter. This shows the general setup of a mercury magnetometer based on an absorptive readout. It can be used to operate a co-magnetometer or a pure magnetometer.

3·3 SYSTEMATIC EFFECTS

Various sources of systematic uncertainties for measuring magnetic fields with mercury in a direct measurement or in nEDM experiments have been discussed in previous works. Besides estimating the impact of these known effects like the direct light shift [50] and geometric phases [88, 91], this chapter shows that for a next generation EDM experiment, also the DC-Stark shift has to be taken into account.

A systematic effect causing a shift in the measured precession frequency $\delta\omega$ of mercury atoms leads to a shift in the measurement of the magnetic field of the size $\delta B = \frac{1}{\gamma_{Hg}}\delta\omega$. Effects causing $\delta\omega$ to scale anti symmetric with the electric field E in an EDM experiment can lead to the false conclusion that mercury atoms have an EDM of the size [91]

$$\delta d_{\mathrm{Hg}} = \frac{\hbar}{4E}(\delta\omega(E) - \delta\omega(-E)). \tag{3.3.1}$$

If the frequency measurement with mercury atoms is used to detect and analytically cancel magnetic field fluctuations in an nEDM experiment, the contribution of this shift to the nEDM result can be as large as

$$\delta d_{\mathrm{n}} = \frac{\gamma_{\mathrm{n}}}{\gamma_{\mathrm{Hg}}}\delta d_{\mathrm{Hg}}. \tag{3.3.2}$$

The ratio of the gyromagnetic ratios $\frac{\gamma_{\mathrm{n}}}{\gamma_{\mathrm{Hg}}}$ was measured to be -3.84 [53]. In the following, these relations are used to estimate the impact of different sources of uncertainties and shifts in the Larmor frequency measurements with mercury vapor on the accuracy of magnetic field and nEDM measurements.

Effects causing a shift in the magnetic field measurements do not necessarily cause systematic shifts in the nEDM measurement. A constant shift that adds the same value to every magnetic field measurement (a systematic shift of the magnetometer) cancels out in an nEDM experiment. If the shift scales linearly with the electric field, it is a systematic effect and the shift in the nEDM measurement can be calculated with equation 3.3.1 and equation 3.3.2. A statistical uncertainty in the magnetic field measurement translates to a statistical uncertainty of the nEDM measurement. In this thesis, the statistical uncertainty of the nEDM measurement is calculated according to equation 3.3.1 and equation 3.3.2 as well. However, by repeating the measurement N times, the statistical uncertainty is reduced by a factor of $\sqrt{N}$. In a double chamber experiment, one single free precession measurement corresponds to $N = 2$ which already reduces of the estimated uncertainties by a factor of $\sqrt{2}$.

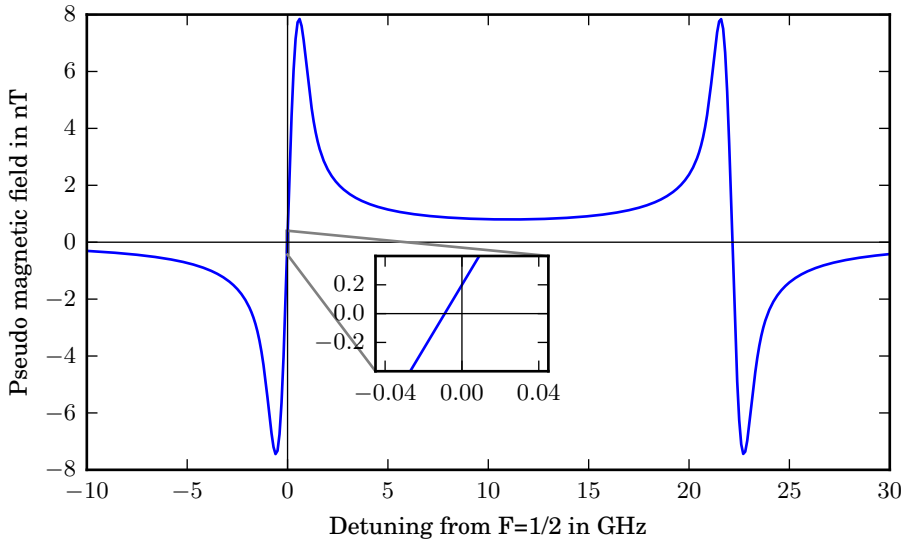

Figure 3.3.1: Light shift magnetic field in a laser beam as a function of the detuning from the F=1/2 hyperfine transition for typical environmental parameters. The light beam has a 2.5 mm radius and a power of 1 µW. The plot is based on an implementation of equation 1.3.1 by Gerd Petzoldt and Thomas Stolz. It is described in more detail in [98]. Consequences of the light shift for magnetic field and EDM measurements are discussed in section 3.3.1.

3.3.1 VECTOR LIGHT SHIFT

Light traversing the atomic vapor with a frequency close to resonance can shift opposite magnetic sub levels in opposite directions via the vector light shift (VLS) as described in section 1.3.1. For an atom with F=1/2 in the ground state, like ^{199}Hg, the hamiltonian is modified by the light in the same way as by a magnetic field, causing a precession ω_{VLS} of mercury atoms in the ground state that are prepared accordingly [50]. In a real magnetic field, the observed Larmor precession is caused by the sum of the Zeeman shifts due to the real magnetic field B_0 and the fictive magnetic field $B_{\mathrm{VLS}} = \gamma_{\mathrm{Hg}}\omega_{\mathrm{VLS}}$.

Plotted as a function of detuning from resonance, the fictive magnetic field B_{VLS} caused by the light has a dispersive shape (see equation 1.3.1), and is zero on resonance when evaluated for a single transition. However, as the hyperfine states $F = \frac{1}{2}$ and $F = \frac{3}{2}$ in the $^3P_1$ state of ^{199}Hg are only 22.15 GHz apart, the shift caused by one of the hyperfine transitions is not zero at the position of the second one. To get the full picture of the light shift fictive magnetic field, the B_{VLS} caused by both hyperfine transitions have to be added up. Due to this superposition, the NLP is shifted away from resonance. An example for a full light shift curve is given in figure 3.3.1. In this example, the vapor temperature is 300 K, and a fully circularly polarized beam is used with a power of 1 µW and a radius of 2.5 mm.

The width of the peaks depends on the vapor pressure and Doppler broadening. In the mercury EDM experiment at the University of Washington [15, 99] a buffer gas

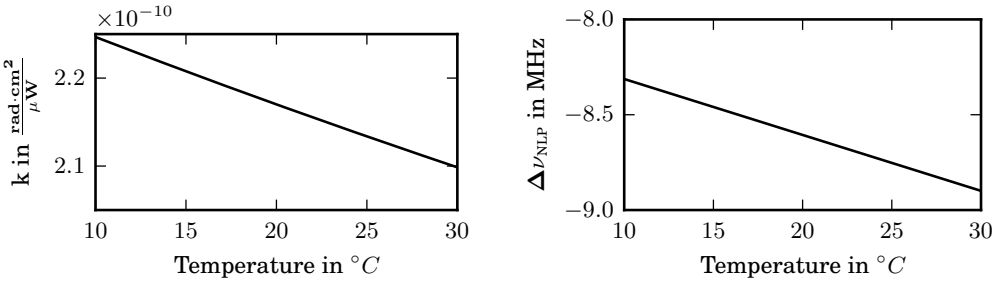

(a) Slope of the light-shift curve $\omega_{\mathrm{VLS}}(\Delta\nu)$ at the NLP.

(b) Offset of the NLP from resonance.

Figure 3.3.2: Temperature dependence of the slope of the light shift curve close to the NLP (a), and the distance $\Delta\nu_{\mathrm{NLP}}$ between the NLP and the center of the transition (b).

broadens the transitions which leads to a higher and almost constant level between the hyperfine transitions. As the pressure in an nEDM precession chamber is very low ($5\times10^{10}\,\mathrm{cm}^{-3}$ [75]), the width of the features is smaller and dominated by the Doppler shift.

The same is true for the NLP. With higher temperatures, the increased Doppler width of the F=3/2 transition shifts the the NLP further away from resonance with the F=1/2 transition. The extent of this temperature dependence is shown in figure 3.3.2b.

Close to its zero-crossing, the precession frequency ω_{VLS} can be approximated linearly as

$$\omega_{\mathrm{VLS}}(\Delta\nu_L) = P_L\cdot I_L\cdot k\cdot\Delta\nu_L. \tag{3.3.3}$$

Where P_L is the degree of circular polarization of the light and takes the values 1 for pure left-circular, and −1 for pure right-circular polarization. I_L is the intensity of the readout beam, and $\Delta\nu_L$ the frequency detuning of the laser from the NLP in MHz. The constant k can be calculated from equation 1.3.1 and is positive for the zero crossing close to the $F=\frac{1}{2}$ and negative close to the $F=\frac{3}{2}$ transition. Evaluating k for the zero crossing at $F=\frac{1}{2}$ and a temperature of $T=300\,\mathrm{K}$, yields $2.12\times10^{-10}\,\mathrm{rad\,cm^2\,\mu W^{-1}}$. The temperature depndence of k is shown in figure 3.3.2a.

Expressed as a fictive magnetic field caused by a perfectly circularly polarized readout beam, the linear approximation of the light shift becomes

$$B_{\mathrm{VLS}} = I_L\cdot\frac{k}{\gamma_{\mathrm{Hg}}}\cdot\Delta\nu_L, \tag{3.3.4}$$

and the shift between resonance and the zero crossing is −8.81 MHz for these conditions.

With a readout power of 10 μW, which is roughly the highest power that is acceptable in terms of light induced depolarization [75], and a beam with a 5 mm diameter, the pseudo magnetic field becomes

$$B_{\mathrm{VLS}}(\Delta\nu_L) = 2.26\cdot10^{-10}\,\frac{\mathrm{T}}{\mathrm{MHz}}\cdot\Delta\nu_L. \tag{3.3.5}$$

Readout beam power	10 µW
Readout beam radius	2.5 mm
Precession cell radius	24 cm
Precession cell height	12 cm
Temperature	300 K
Angle α	1/400 rad

Table 3.3.1: Experimental parameters that were used to estimate the uncertainties in this chapter.

Here, the laser wavelength is detuned from the no light shift point by $\Delta\nu_L$ in MHz.

The Larmor frequency of every atom in the ground state is modified as long as the atom is subject to the readout beam. However, as the precession volume is larger than that of the readout beam, the atoms will not be affected by the light shift all the time.

As the effect of the light on the spin states of the atoms is the same as that of a magnetic field, it adds to the absolute value of the real magnetic field B_0 depending on the angle φ between the two fields:

$$B_{\text{eff}}^2 = B_0^2 + B_{\text{VLS}}^2 - 2B_0 B_{\text{VLS}} \cos(\varphi). \tag{3.3.6}$$

Because the readout light is supposed to traverse the vapor perpendicular to the holding field, it is more intuitive to use the angle α by which φ deviates from 90°. B_{eff} can then be written

$$B_{\text{eff}} = \sqrt{B_0^2 + B_{\text{VLS}}^2 + 2B_0 B_{\text{VLS}} \sin(\alpha)}. \tag{3.3.7}$$

The Larmor frequency of the atoms in this effective magnetic field is

$$\omega_{\text{eff}} = \gamma \cdot B_{\text{eff}} = \sqrt{\omega_0^2 + \omega_{\text{VLS}}^2 + 2\omega_0 \omega_{\text{VLS}} \sin(\alpha)}. \tag{3.3.8}$$

Due to the fictive magnetic field caused by the vector light shift, the Larmor frequency of the mercury atoms during the field measurement in an EDM experiment is changed in two different ways:

- The average Larmor frequency is changed directly due to the modified magnitude of the effective magnetic field caused by the light shift (direct light shift).
- As B_{VLS} is mainly perpendicular to B_0, it can cause a geometric phase. The latter effect will be discussed in section 3.3.2.2.

Direct vector light shift

For an atom that is subject to the readout beam during the whole measurement time, one can show with equation 3.3.8 that the shift of the Larmor frequency measurement caused by the direct light shift effect $\delta\omega_{\text{dVLS}}$ can be approximated as

$$\delta\omega_{\mathrm{dVLS}}^{\mathrm{beam}} \approx \underbrace{\omega_{\mathrm{VLS}} \cdot \sin(\alpha)}_{(1)} + \underbrace{\frac{1}{2} \cdot \cos^2(\alpha) \cdot \frac{\omega_{\mathrm{VLS}}^2}{\omega_0}}_{(2)} \approx \omega_{\mathrm{VLS}} \cdot \alpha + \frac{1}{2} \cdot \frac{\omega_{\mathrm{VLS}}^2}{\omega_0}. \tag{3.3.9}$$

Here, a series expansion was used with the assumption $\omega_{\mathrm{VLS}} << \omega_0$.

The deviation δB_{dVLS} of the measured magnetic field from the holding field B_0 inside the readout beam is

$$\delta B_{\mathrm{dVLS}}^{\mathrm{beam}} \approx \underbrace{B_{\mathrm{VLS}} \cdot \sin(\alpha)}_{(1)} + \underbrace{\frac{1}{2} \cdot \cos^2(\alpha) \cdot \frac{B_{\mathrm{VLS}}^2}{B_0}}_{(2)} \approx B_{\mathrm{VLS}} \cdot \alpha + \frac{1}{2} \cdot \frac{B_{\mathrm{VLS}}^2}{B_0}. \tag{3.3.10}$$

As the readout beam usually does not illuminate the whole precession cell, the ratio of the time spent in and outside the beam has to be considered.

With the ratio of the volume that is illuminated by the laser beam to the whole precession chamber volume $\nu_{\mathrm{b/c}} = \frac{A_{\mathrm{beam}} \cdot L_{\mathrm{beam}}}{V}$, and the assumption that each atom spends the same amount of time in each part of the precession volume, the average frequency shift is

$$\delta\omega_{\mathrm{dVLS}} = \nu_{\mathrm{b/c}} \cdot \delta\omega_{\mathrm{VLS}}^{\mathrm{beam}} = \nu_{\mathrm{b/c}} \cdot \gamma \cdot \delta B_{\mathrm{VLS}}^{\mathrm{beam}}. \tag{3.3.11}$$

As both, $\nu_{\mathrm{b/c}}$ and $\frac{1}{\delta B_{\mathrm{dVLS}}}$, scale linearly with the cross-sectional area of the beam, the result of this is independent from the width- and depends only on the length of the laser beam path in the atomic vapor.

Splitting the direct light shift into the two terms given above (see equation 3.3.10), and using equation 3.3.5, the light shift can be evaluated in the proximity of the NLP for the two terms separately:

$$\delta\omega_{\mathrm{dVLS}} = \delta\omega_{\mathrm{dVLS}}^{(1)} + \delta\omega_{\mathrm{dVLS}}^{(2)}, \tag{3.3.12}$$

with

$$\delta\omega_{\mathrm{dVLS}}^{(1)} = \omega_{\mathrm{VLS}} \cdot \alpha,$$
$$\delta\omega_{\mathrm{dVLS}}^{(2)} = \frac{1}{2} \cdot \frac{\omega_{\mathrm{VLS}}^2}{\omega_0}.$$

The first of these two terms expressed as frequency shift $\delta\omega_{\mathrm{dVLS}}$ and as pseudo magnetic field δB_{dVLS} as functions of the frequency detuning $\Delta\nu_L$ from the NLP and the misalignment angle α is

$$\delta\omega_{\mathrm{dVLS}}^{(1)}(\Delta\nu_L) = 4.7 \cdot 10^{-9} \frac{\mathrm{rad}}{\mathrm{s \cdot MHz \cdot mrad}} \cdot \Delta\nu_L \cdot \alpha, \tag{3.3.13}$$

$$\delta B_{\mathrm{dVLS}}^{(1)}(\Delta\nu_L) = 9.8 \cdot 10^{-17} \frac{\mathrm{T}}{\mathrm{MHz \cdot mrad}} \cdot \Delta\nu_L \cdot \alpha. \tag{3.3.14}$$

For these values, a cell with the radius 0.24 m and the height 0.12 m, and the same environmental- and beam parameters as above (see table 3.3.1) are assumed.

If the field measurement shift was proportional to the electric field, the shift in an EDM measurement of the mercury atoms $\delta d^{(1)}_{\mathrm{dVLS,Hg}}$ and the shift caused by the mercury atoms when used as a co-magnetometer for the measurement of an nEDM $\delta d^{(1)}_{n}$ are

$$\delta d^{(1)}_{\mathrm{dVLS,Hg}}(\Delta\nu_L) = 9.3\cdot10^{-29}\cdot\frac{e\,\mathrm{cm}}{\mathrm{MHz{\cdot}mrad}}\cdot\Delta\nu_L\cdot\alpha, \tag{3.3.15}$$

$$\delta d^{(1)}_{\mathrm{dVLS,n}}(\Delta\nu_L) = 3.6\cdot10^{-28}\frac{e\,\mathrm{cm}}{\mathrm{MHz{\cdot}mrad}}\cdot\Delta\nu_L\cdot\alpha. \tag{3.3.16}$$

The second term in equation 3.3.9 for a 1 µT holding field as a function of the detuning from the NLP is

$$\delta B^{(2)}_{\mathrm{dVLS}}(\Delta\nu_L) = v_{\mathrm{b/c}}\cdot\frac{1}{2}\cdot\frac{B^2_{\mathrm{VLS}}}{B_0}, \tag{3.3.17}$$

$$\delta B^{(2)}_{\mathrm{dVLS}}(\Delta\nu) = 1.1\cdot10^{-17}\frac{\mathrm{T}}{\mathrm{MHz}^2}\cdot\Delta\nu_L^2. \tag{3.3.18}$$

For a detuning from the NLP smaller than 1 MHz, this is already smaller than $\delta B^{(1)}_{\mathrm{dVLS}}(\Delta\nu_L)$, even if the misalignment was only 1 mrad. However, while symmetric fluctuations of the laser do not contribute to $\delta B^{(1)}_{\mathrm{dVLS}}$ as it is linear in $\Delta\nu_L$, they do not cancel out for $\delta B^{(2)}_{\mathrm{dVLS}}$.

Assuming that α can be set as accurate as $1/400$ rad, the dominating shift for an nEDM measurement due to the direct vector light shift is

$$\delta d^{(1)}_{n}(\Delta\nu_L) = 8.9\cdot10^{-28}\frac{e\,\mathrm{cm}}{\mathrm{MHz}}\cdot\Delta\nu_L. \tag{3.3.19}$$

And for fluctuations of the laser frequency with the width $\Delta\nu_L$ around the lock point, the second term dominates with

$$\delta d^{(2)}_{n}(\Delta\nu_L) = 4.0\cdot10^{-29}\frac{e\,\mathrm{cm}}{\mathrm{MHz}^2}\cdot\Delta\nu_L^2. \tag{3.3.20}$$

The relations derived here are used to estimate the extend of different systematic uncertainties in the following.

3.3.1.1 *Adiabaticity*

When the laser frequency is detuned and the beam causes a light–shift pseudo-magnetic field, the atoms are passing the beam region several times during the free

precession period. The mean thermal velocity of mercury atoms is in the order of $150\,\mathrm{m\,s^{-1}}$ at room temperature. In an nEDM experiment, the holding field is typically in the order of µT leading to a precession frequency of <10 Hz. When the laser beam has a 5 mm diameter, most of the times when an atom passes through the laser beam the spin can thus not follow the magnetic field lines adiabatically.

For term (1) in equation 3.3.9, adiabaticity does not matter as it is determined by the component of the light–shift pseudo-magnetic field that is parallel to the holding field. The spins will thus experience a slightly increased or decreased holding field for the time they spend in the laser beam.

The second term in equation 3.3.9 however is reduced for non-adiabatic passages through the laser beam. The component of the light–shift pseudo-magnetic field that is perpendicular to the holding field causes small shifts of the spins out of the precession plane (θ-shift) during each non-adiabatic passage through the beam but no shifts in the precession plane. However, the component perpendicular to the holding field is usually much larger than the parallel component. Estimations of systematic effects that are caused by the second term in equation 3.3.9 can thus be treated as worst-case estimations.

3.3.2 GEOMETRIC PHASES

Particles moving in the electric field of a trap experience an effective motional magnetic field $\vec{E} \times \frac{\vec{v}}{c^2}$. Every time they hit the wall or other particles in the trap, their velocity changes. This causes the motional magnetic field to fluctuate during their precession time.

As no magnetic field is perfectly homogeneous, there are always components perpendicular to the average field that change magnitude and sign depending on the position throughout the trap. Particles moving randomly through these fields experience the sum of all perpendicular magnetic fields.

The precession frequency shift $\delta\omega$ such a magnetic field introduces that fluctuates perpendicular to a holding field is discussed in [100]. It can be written in powers of the electric field [91]:

$$\delta\omega = \delta\omega_{B^2} + \delta\omega_{BE} + \delta\omega_{E^2}. \tag{3.3.21}$$

The first term only depends on the vertical magnetic field in the storage volume, the second term scales linearly with the motional magnetic field and the inhomogeneities of the holding field, and the third term scales with the square of the electric field.

Only the second term in 3.3.21 scales linearly with the electric field. As it can not be distinguished from a nonzero EDM without further measures, it limits the accuracy of an EDM measurement. In [91] was shown that this systematic shift depends only on the volume average over the magnetic field components that are perpendicular to the holding field and is given by

$$\delta\omega_{BE} = -\frac{\gamma^2 E}{c^2}\left\langle x B_x + y B_y \right\rangle. \tag{3.3.22}$$

Giving rise to a systematic shift in an EDM measurement of

$$\delta d_{Hg} = -\frac{\hbar\gamma^2}{2c^2}\left\langle x B_x + y B_y \right\rangle. \tag{3.3.23}$$

With these formulas, the effect from the imperfections of the holding field as well as from the pseudo magnetic field potentially caused by the readout laser beam can be calculated. The latter can cause a shift because it traverses the mercury vapor in the x-y-plane and gets weaker along its path as the light is partially absorbed by the mercury vapor.

3.3.2.1 *Geometric phase for particles moving in an electric and an inhomogeneous magnetic field*

Evaluating equation 3.3.22 for a gradient in z direction in a cylindrical cell with the symmetry axis pointing in z direction gives [91]

$$\delta\omega_{BE} = \frac{\gamma^2 R^2 E}{16c^2}\cdot\frac{\partial B_z}{\partial z}. \tag{3.3.24}$$

This result was experimentally verified in [101]. Geometric phases acquired by the UCNs are typically smaller than those acquired by mercury atoms by more than an order of magnitude [88].

Although the systematic shift caused by this effect would dominate in an nEDM measurement for realistic magnetic field gradients according to [101], it was shown in [89] that, due to the different average height at which the mercury atoms and the neutrons measure the magnetic field of the trap, the gradient during this precession period can be measured. As the geometric phase scales linearly with the electric field, but the frequency difference caused by the different average height of the two species does not, the results of the nEDM measurements can be corrected for the gradient-related geometric phases to some extent (see figure 3.3.3).

Such a correction can not be done for the geometric phase caused by the light shift of the readout beam. With a sufficiently precise frequency lock of the laser to the NLP however, the light shift magnetic field can be made small. An examination of the size of this effect is presented in the following section.

3.3.2.2 *Light shift geometric phases*

As the readout beam traverses the atomic vapor in the precession cell, absorption reduces the intensity of the beam. Equation 3.3.4 describes the dependency of the fictional light shift field on the intensity of the Laser beam. In a scenario where the light shift is not zero, the readout beam effectively adds a magnetic field that is perpendic-

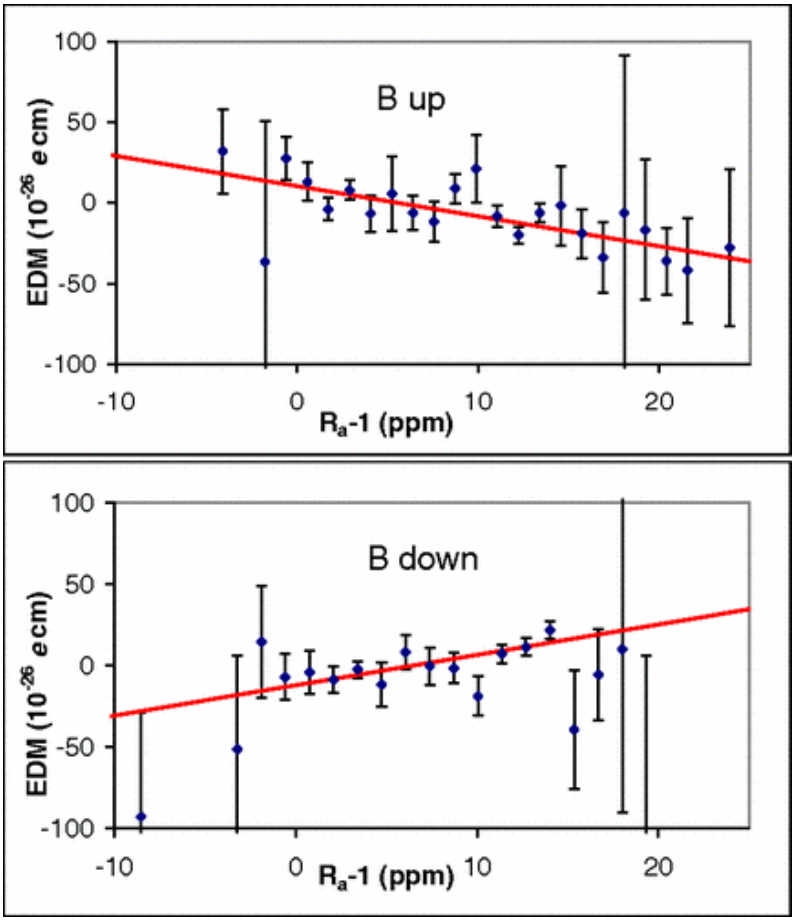

Figure 3.3.3: Correction for geometric phases caused by linear field gradients. The values on the x-axis are proportional to the frequency ratio of the UCNs and the ^{199}Hg atoms and thus to the field gradient during each measurement run. The y-axis shows the corresponding EDM values. If no further corrections were needed, at the crossing point of the the linear fits, the gradient would be $\frac{\partial B}{\partial z} = 0$. Taken from [24], where this technique and further effects that shift the crossing point are discussed.

ular to the holding field, restricted on the volume that is illuminated by the readout beam. It gets smaller from the point where the laser beam enters ($B_{\mathbf{VLS,0}}$) to the point where it leaves the cell.

One scenario that can lead to a non zero light shift is the Stark effect shifting the light shift curve in the precession chamber and this shift not being corrected for in the spectroscopy cell as shown in section 3.3.4.1. When the readout beam traverses the precession cell in x direction, equation 3.3.22 becomes

$$\begin{aligned}\delta\omega_{BE} &= -\frac{\gamma^2 E}{c^2}\left\langle x B_{\mathrm{VLS}}(x)\right\rangle, \\ &= -\frac{\gamma^2 E}{c^2}\left\langle x\cdot B_{\mathrm{VLS,0}}\cdot e^{-\lambda(x+R)}\right\rangle.\end{aligned} \tag{3.3.25}$$

With the fictional magnetic field being constrained to the intersection volume of the readout beam and the precession cell, the average over the whole precession chamber is

$$\begin{aligned}\left\langle x B_{\mathrm{VLS}}(x)\right\rangle &= \frac{\pi R_L^2}{V_c}\int_{-R_c}^{R_c} dx\cdot x B_{\mathrm{VLS}}(x), \\ &\approx \frac{\pi R_L^2}{V_c}\int_{-R_c}^{R_c} dx\cdot x\cdot B_{\mathrm{VLS,0}}(1-\lambda(x+R_c)) \\ &= -\frac{V_L}{V_c}B_{\mathrm{VLS,0}}\lambda\frac{2}{3}R_c^2.\end{aligned} \tag{3.3.26}$$

Where the volume of the laser beam with the radius R_L inside the vapor cell is V_L and the cell volume is V_c.

This leads to a change in the precession frequency due to the light shift geometric phase effect in the case of a small absorption of

$$\delta\omega_{\mathrm{LSGP}} = \frac{\gamma^2 E}{c^2}\cdot\frac{V_L}{V_c}B_{\mathrm{VLS,i}}\lambda\frac{2}{3}R_c^2. \tag{3.3.27}$$

When the vapor density is chosen such that 16% of the readout beam are absorbed by the mercury, which was shown to be a suitable choice in order to obtain a large amplitude in the transmission signal [21], and for experimental parameters as are used for estimating the light shift effects above (see table 3.3.1), the systematic shift caused by the light shift geometric phase effect is

$$\delta d_{LSGP} = -1.7\times10^{-29}\, e\,\mathrm{cm\,MHz^{-1}}\cdot\Delta\nu. \tag{3.3.28}$$

This effect is estimated using equation 3.3.27, assuming that the laser beam cross section is homogeneous along its beam path. However, the laser usually has a small widening component which causes additional gradients in the plane that is perpendicular to the holding field, and a contribution to the frequency shift as the term $\left\langle y\cdot B_y\right\rangle$

in equation 3.3.22 does not vanish. However, as the widening component y is small compared to the x-component, the $\langle y \cdot B_y \rangle$ is much smaller than $\langle x \cdot B_x \rangle$ for most applications.

If the laser beam has a widening component, this also leads to an additional weakening of the x-component of the laser beam from the entrance window to the exit window. However, this weakening is small compared to the weakening that is caused by absorption.

The light-shift geometric phase effect can not be seen in the gradient analysis [101] which is capable of distinguishing geometric phase effects from EDMs (see section 3.3.2.1). In the case that it turns out to be necessary to separate the light-shift geometric phase effect from an EDM, the only way to do that would be to additionally analyze the dependency of the results on the laser power and the optical absorbance of the precession cell. The latter could be achieved by varying the isotopic composition of the mercury vapor, as this would leave the particle density unaffected.

3.3.3 MISALIGNMENT

The accuracy of the angle α between the readout beam and the magnetic field in the precession chamber is dominated by aligning the optics that send the beam into the shielded room and the readout behind the room to be at the same height. Assuming that this can be done with an accuracy better than 1 cm and as the light travels 4 m between the optics, α is smaller than $1/400$ rad.

In principal, this is not correlated with the electric field which makes this a statistical uncertainty. However several systematic contributions are possible. For example, leakage currents could cause transverse magnetic fields that are proportional to the electric field. As this changes the angle between the magnetic field and the z-axis, it also effects α. However, this effect is expected to be much smaller than $1/400$ rad.

3.3.4 DEVIATION OF THE LASER FREQUENCY FROM THE NLP

Anything that causes the magnetometer transition to be shifted differently in the precession volume and the spectroscopy that is used for the frequency lock can cause light shift effects even if the laser wavelength is stabilized perfectly to the NLP in the spectroscopy cell.

3.3.4.1 *DC Stark shift*

DC Stark shifts in an electric field E can be expressed in terms of scalar- and tensor polarizabilities of the atoms. For atoms in hyperfine states F and the magnetic sublevels m_F, the shift can be parametrized as

$$\Delta E_m = -\tfrac{1}{2}\varepsilon^2\alpha_0 - \alpha_2(3\varepsilon_z^2 - \varepsilon^2)\cdot Y, \tag{3.3.29}$$

with Y given in section 1.3.2.2.

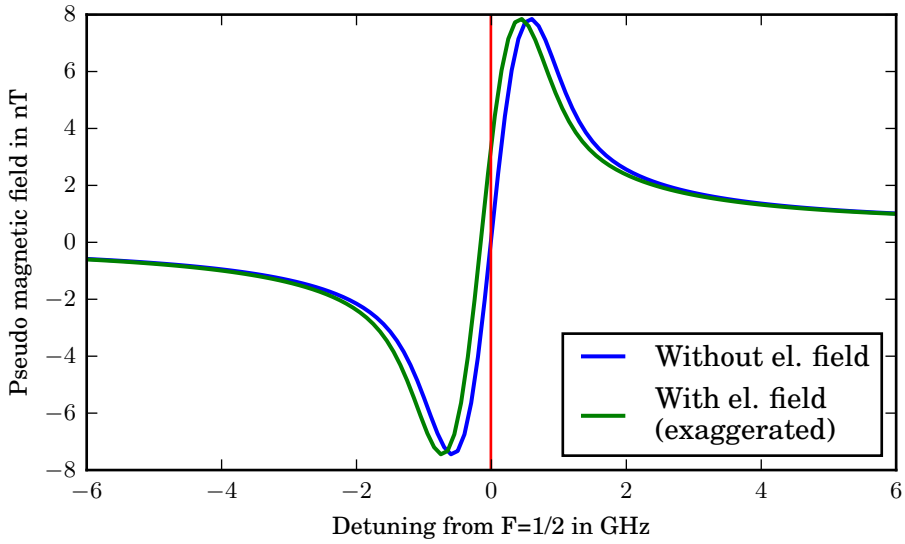

Figure 3.3.4: Light shift curve for low pressure mercury vapor with and without electric field. The shift is exaggerated for illustration. The vertical line marks the position of the NLP without electric field.

The first, scalar, term is the same for all hyperfine states and their magnetic sub-levels, and the shift due to the second, tensor, term changes for different $|F, mF\rangle$ states.

While the tensor Stark shift is zero for the atomic states that play a role in pumping and reading out the magnetometer, the scalar Stark effect shifts the ground state and the excited state by a different amount. This differential scalar Stark shift between the ground state and the $^3P_1$ state was measured to be $-3.32\,\mathrm{kHz}/(\mathrm{kV/cm})^2$ [56].

As the different magnetic sub-levels of the ground state are shifted by the same amount due to the scalar Stark effect, the Larmor frequency of the mercury atoms in the ground state is not directly affected.

However, due to the differential scalar Stark shift, the magnetometer transition is shifted with the electric field squared. In an EDM experiment using electric fields up to 20 kV/cm, this shift is 1.328 ± 0.024 MHz.

If the vapor cell used for the frequency lock of the laser is not subject to the same electric field, the transitions and thus the NLPs in the magnetometer are shifted compared to the spectroscopy. When the laser is locked to the NLP in the spectroscopy, switching on an electric field in the precession cell shifts the laser frequency away from the NLP as shown in figure 3.3.4. Thus, although the DC-Stark shift does not cause a systematic effect directly in magnetometry or EDM experiments, it can cause a light shift if it is not corrected. This light shift will cause all the shifts and uncertainties discussed in section 3.3.1 and section 3.3.2.2.

When the nEDM is measured for the highest achievable electric fields $|E_{max}|$ and $-|E_{max}|$ the DC Stark shift causes a constant $\Delta\nu$ in all measurements.

The first term in equation 3.3.9 dominates the direct vector light shift if the product of α and $\Delta\nu$ averaged over the free precession time $\langle\alpha\cdot\Delta\nu\rangle$ is not zero. For example, this is true if α and $\Delta\nu$ are constant on the timescale of one measurement τ.

The second term dominates for effects where $\langle\alpha\cdot\Delta\nu\rangle\approx 0$. This is the case when at least one of the two factors fluctuates on timescales that are smaller than τ while the other one can be either constant of fluctuate as well.

If the DC Stark shift is not compensated, it causes a constant $\Delta\nu$ of 1.33 MHz according to equation 3.3.29. Then, assuming that α is random but constant during τ, the vector light shift is dominated by $\delta d^{(1)}_{n,\mathrm{dVLS}}$=$1.2\times10^{-27}\,e$ cm. As it scales with E^2, this is a statistical uncertainty as long as inverting the electric field leads to the same $|E|$, and α is not correlated with the electric field. Any partial correlation leads to a systematic shift. However, the Stark shift can be compensated by applying the same electric field to the atomic vapor of the spectroscopy as to that in the precession chamber, or by calculating the DC Stark shift and compensating for it when the frequency lock is established as shown in section 3.4.1.

The light-shift geometric-phase effect caused by an uncompensated DC Stark shift is $2.2\times10^{-29}\,e$ cm according to equations 3.3.29, 3.3.4, and 3.3.27. This is a systematic effect and it and can not be detected or reduced by measuring the magnetic field gradients like the geometric phase effect as described in section 3.3.2.1. It does however scale with E^3 as the electric field causes the transverse magnetic field ($B_{\mathrm{VLS,x}}\propto E^2$) through the Stark shift, and additionally directly contributes to equation 3.3.22 linearly.

3.3.4.2 *Pressure shift*

As the vapor pressure in the spectroscopy cell is higher than in the precession chamber, the transitions of the atoms in the two setups are shifted relative to each other as well.

The pressure shift was measured using nitrogen as a buffer gas to be −2.54 MHz/Torr [102], and is thus small compared to the other shifts between spectroscopy and readout cell given above. Fluctuations of the vapor pressure in spectroscopy and precession chamber thus cause shifts in the frequency lock that are in the sub-kHz range, and, hence, uncritical.

3.3.4.3 *Temperature fluctuations*

In the precession cell, the NLP changes with the vapor temperature. This dependence is shown in figure 3.3.2b. In the vicinity of the of 300 K, the shift is smaller than 30 kHz K^{-1} [98], and should not be a problem in a temperature stabilized environment. In the spectroscopy cell, a change of the temperature additionally causes fluctuations of the vapor pressure that are not matched in the precession cell but are shown to be small in figure 3.3.2b.

3.3.4.4 *Biased calibration of the frequency axis in the frequency lock*

To establish a lock of the laser frequency to the (NLP), the locking routine that is described in further detail in section 3.4.1 has to find this point in the spectroscopy every time a lock is to be established. Systematic and statistical uncertainties in this routine cause the light shift related effects mentioned above. In practice, the set point for the frequency lock is determined by recording a Doppler-free spectrum that contains the magnetometer transition of ^{199}Hg, and the nearby transition of ^{204}Hg.

The difference between these two can be used as a standard to calibrate the frequency axis of the spectroscopy and to determine the set point for the lock. However, this method relies on knowing the frequency difference ΔIS of this transition between the two isotopes. Any uncertainty $\delta\Delta$IS on this frequency difference translates into a relative uncertainty in finding the correct offset Θ from the center of the magnetometer transition of

$$\delta\Theta = \frac{\delta\Delta\mathrm{IS}}{\Delta\mathrm{IS}} \cdot \Theta. \tag{3.3.30}$$

The current best result for ΔIS is (97 ± 18) MHz [80] with a relative uncertainty of 18.6 %. Using this to calibrate the frequency axis leads to a systematic uncertainty of the frequency the laser is locked to of

$$\delta\Theta = 1.6\,\mathrm{MHz}. \tag{3.3.31}$$

If corrections have to be made, like accounting for the Stark shift in the experiment, this is done with a systematic uncertainty of 18.6 % of the correction as well.

With this calibration of the frequency axis, the laser frequency lock would systematically miss the NLP by 1.6 MHz. With the frequency dependencies of the light-shift effects given in section 3.3.1, this leads to a systematic uncertainty in a single magnetic field measurement of

$$\delta B^{(1)}_{\mathrm{dVLS}} = 3.9 \times 10^{-16}\,\mathrm{T}.$$

The leading uncertainty caused by the vector light shift in an nEDM measurement assuming the uncertainty of α to be $1/400$ rad is

$$\delta d^{(1)}_{\mathrm{dVLS}} = 1.4 \times 10^{-27}\, e\,\mathrm{cm}.$$

Like for the uncompensated DC Stark shift, this uncertainty is statistical as long as there is no correlation between E and α.

However, according to section 3.3.2.2, the geometric phase caused by the light shift pseudo magnetic field introduces a true systematic effect

$$\delta d_{\mathrm{LSGP}} = 2.7 \times 10^{-29}\, e\,\mathrm{cm}$$

that is linear in E like an EDM. The only way to distinguish between the light shift geometric phase caused by a flawed calibration of the frequency axis and a real EDM would be to run measurements with varying readout power settings. The former is proportional to the intensity while the later is independent of it.

To reduce the shift caused by this calibration, the differential isotope shift ΔIS was determined in a dedicated measurement with the spectroscopy setup 2.5.2. The new measurement of the relative isotope shift reduces this shift to insignificance.

3.3.4.5 *Accuracy of finding the locking point*

Every time the frequency shift is to be established, the locking routine has to determine the value of the error signal that corresponds to the laser being set to the NLP. Besides systematical uncertainties, this process is also limited by statistical uncertainties. In section 3.4.1.1.2 is shown, that the accuracy of finding the NLP by recording one spectrum is 0.3 MHz. This can be improved further by recording and fitting the same spectrum repeatedly each time the laser is locked. With equation 3.3.19 and all other conditions as above (see table 3.3.1), this leads to an uncertainty of

$$\delta d^{(1)}_{\mathrm{dVLS}} = 2.7 \times 10^{-28}\, e\,\mathrm{cm}$$

in a single nEDM measurement, and

$$\delta B^{(1)}_{\mathrm{dVLS}} = 2.9 \times 10^{-17}\,\mathrm{T}$$

in a magnetic field measurement.

3.3.4.6 *Stability of the laser frequency*

Although the laser frequency is actively stabilized, there will always be residual fluctuations. As long as these are symmetric around the frequency the laser is locked to, they do not contribute to $\delta\omega^{(1)}_{\mathrm{dVLS}}$. However, they introduce shifts via $\delta\omega^{(2)}_{\mathrm{dVLS}}$ and $\delta\omega_{\mathrm{geo}}$. Assuming residual fluctuations of 1.7 MHz as was measured for a Doppler-free saturation spectroscopy setup (see section 3.4.1.1.2), the shift caused by the direct light shift effect is

$$\delta d^{(2)}_{\mathrm{n,dVLS}} = 1.2 \times 10^{-28}\, e\,\mathrm{cm}.$$

A way to reduce this further without the need to install new, more precise, hardware is shown in section 3.4.1.2.

3.3.5 INTENSITY OF THE READOUT BEAM

Residual fluctuations of the readout beam power contribute to the various light shift effects in a similar way as those of the laser frequency. The light shift pseudo magnetic field B_{VLS} scales linearly with the intensity of the beam like it does for frequencies close to the NLP. If the laser beam power in the precession cell has a correlation with the electric field, $\delta\omega^{(1)}_{\mathrm{dVLS}}$ and $\delta\omega^{(2)}_{\mathrm{dVLS}}$ are enhanced for higher electric fields, and can therefore

potentially cause a systematic shift. This might happen due to changes of the optical properties of the entrance windows caused by an electric field. Monitoring the optical depth of the precession cell is thus proposed. One way to do that is to send and monitor a readout light pulse when the vapor is not polarized or in the exact moment when the precessing magnetization is perpendicular to the readout beam.

3.3.6 MERCURY EDM

When mercury is used as a co-magnetometer in an nEDM measurement the atoms experience the same electric fields as the neutrons. An atomic EDM in the mercury atoms would thus cause a systematic shift according to equation 3.3.2. As the upper limit on the electric dipole moment of mercury atoms is $7.4 \times 10^{-30}\, e\,\mathrm{cm}$ (95% C.L.) [15], the nEDM can not be excluded (with 95% C.L.) for values that are smaller than 2.8×10^{-29} $e\,\mathrm{cm}$. However, even if an nEDM experiment with a mercury co-magnetometer aims beyond this limit, still conclusions can be drawn on the difference between the electric dipole moments of neutrons and mercury atoms.

3.3.7 SUMMARY OF SYSTEMATIC EFFECTS

Atomic magnetometry can provide information on the absolute magnetic field strength without calibration of the magnetometer. Several systematic effects, which have to be considered for a calibration-free magnetometry, are discussed in this chapter.

Equations describing the impact of the light shift effect on measurements of the magnetic field (equation 3.3.14) and on the nEDM-result (equation 3.3.16) when mercury is used in a co-magnetometer are derived for typical conditions in a co-magnetometer. The equations derived here are used to investigate the impact of different systematic uncertainties on the measurement results.

Uncertainties of parameters that contribute to the light shift and their impact on magnetic field and EDM measurements are estimated. It is shown that with the Isotope shift measurement presented in section 2.5.2, the corresponding systematic uncertainty of setting the laser frequency is reduced from 1.6 MHz to 15 kHz which is smaller than the statistical accuracy of finding the NLP (see section 3.3.4.5).

Geometric phases in electric fields and magnetic field gradients have been covered in previous works and compensation of geometric phases by extracting the magnetic field gradient and extrapolating to zero is an established technique. However, a systematic effect that has not been mentioned in literature so far is the combination of the light-shift effect and geometric phases. The size of the light-shift induced geometric phase effect in linear approximation is estimated to be

$$\delta d_{LSGP} = -1.7 \times 10^{-29}\, e\,\mathrm{cm\,MHz}^{-1} \cdot \Delta\nu \tag{3.3.32}$$

for typical experimental parameters (see table 3.3.1) in a co-magnetometer.

The light-shift induced geometric phase can not be extrapolated form tracking the field gradients in the same way as the regular geometric phases. If an EDM experiment with a mercury co-magnetometer reaches an accuracy where light-shift geometric phases matter, it is proposed to vary the readout beam power or the isotopic mixture of the mercury vapor to detect this effect.

Another effect that has not been taken into account in previous works is a light-shift effect that is caused by the DC Stark shift. Section 3.3.4.1 shows that the relative shift of the readout beam frequency from resonance can be as large as 1.33 MHz and thus cause light-shift effects.

One of these effects is the 'DC-Stark shift induced light-shift geometric phase effect'. Assuming that the laser is perfectly locked to the NLP in spectroscopy, the DC Stark effect shifts the transition in the mercury vapor in the nEDM cell by 1.33 MHz. This leads to a light-shift geometric phase effect of the size 2.2×10^{-29} e cm as described above. As this effect scales with E^3 it is anti-symmetric in the electric field and can thus be a systematic effect in an nEDM measurement.

While all Stark shift and geometric phase related effects are only relevant for magnetometry applications with electric fields like EDM measurements, the light-shift effect is also relevant for magnetometry without an electric field.

3.3.8 SYSTEMATICS IN CO- VS. PURE MAGNETOMETRY IN NEDM EXPERIMENTS

Differences between mercury co-magnetometers and pure mercury magnetometers in nEDM experiments can be grouped in three major categories which are summarized in this section.

In pure mercury magnetometer cells that are placed above and below the UCN chamber stack, the mercury atoms are not subject to an electric field. Electric field related systematic effects are thus only an issue in co-magnetometry. Consequences of this are discussed in section 3.3.8.1. Practical implications when mercury and UCNs are co-habitating the same volume are discussed in section 3.3.8.2. Finally, geometric considerations of the two different kinds of magnetometers are shown in section 3.3.8.3.

3.3.8.1 *Electric field vs. no electric field*

In a mercury co-magnetometer (see figure 1.4.3), the Stark-shift induced light-shift effect and the geometric-phase effect cause shifts in the measurement of the magnetic field and the results of an nEDM measurement when the co-magnetometer is used to correct for magnetic field drifts. While the Stark shift can be accounted for by adopting the laser frequency (see section 3.3.4.1), the geometric phases are more problematic. To correct for the geometric phases, the magnetic field is assumed to have a constant value B_0 and a linear gradient. As the geometric phase effect for mercury is typically large, linear fits have to be applied over several orders of magnitude (see figure 3.3.3) to extract their crossing point.

Any components of the magnetic field with $\langle x B_x + y B_y \rangle \neq 0$ cause geometric phases. If the magnetic holding field has a component B_{geo} with $\langle |\boldsymbol{B}| \rangle = 0$ but $\langle x B_x + y B_y \rangle \neq 0$ (like an uncorrected linear gradient or a component $\propto z^3$), the co-habitating mercury magnetometer can thus even reduce the sensitivity of a single nEDM measurement.

In pure magnetometers that are placed above and below the UCN cell-stack (see figure 3.3.5), there are no electric field effects. However, they are also less sensitive to local effects that change the magnetic field inside the UCN precession chambers and of those especially effects that are proportional to the electric field. If only external magnetometers are used, it is thus crucial to make sure that effects like leakage currents are small enough. At some level, this becomes difficult without a co-magnetometer.

3.3.8.2 *Co-habitating vs single-species*

Practical issues of cohabitating UCN and ^{199}Hg atoms are discussed in section 1.4.2.1.1. A major advantage of standalone magnetometers is that a higher mercury vapor pressure can be used. As the particle density in a co-magnetometer is limited to below $\sim 5 \times 10^{10}$ cm^{-3}, a readout based on rotation of a linear polarization axis is not feasible as the rotation angle would be too small [75]. In a standalone magnetometer, a factor of thousand more mercury atoms can be used which makes the mercury EDM readout scheme feasible [15]. In this readout scheme, off-resonant light is used which leads to a low absorption of the laser light. A higher power laser beam can thus be used without

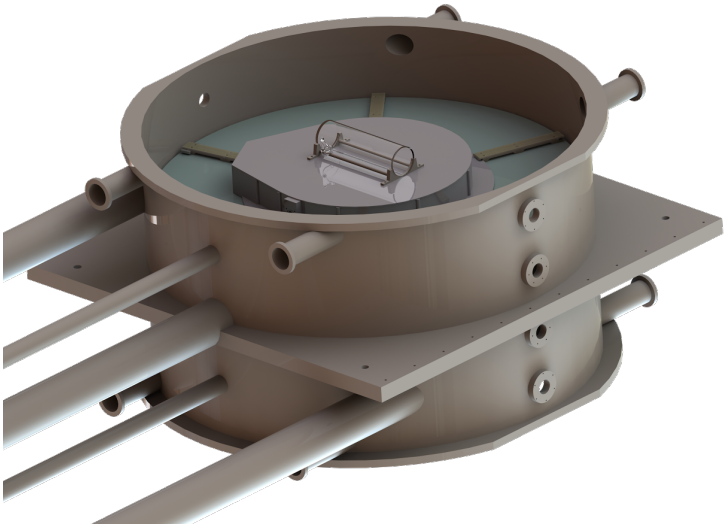

Figure 3.3.5: Vacuum chamber for nEDM experiment. Instead of a large external magnetometer cell, a small cell made entirely from quartz can be used as discussed in the text. One such cell is mounted to each ground electrodes of the UCN cell stack. The vacuum chamber and the UCN cell stack with the electrodes is identical to the one shown in figure 1.4.3. Image taken from [103].

dominating the mercury depolarization rate. The shot noise in this scheme is smaller and the SNR can be increased compared to the absorptive readout scheme (see equation 3.2.7).

Residual circular polarization of the linearly polarized laser beam causes large light shift effects as the laser is not locked to the NLP but to a frequency where the light shift effect is large. However, as long as the power and the circular component of the linear polarization of the laser beams in both vapor cells is the same, the field measured above and below the UCN chambers is shifted by the same amount and thus the value for the nEDM is not affected (see equations 3.3.1 and 3.3.2).

Another benefit of a higher vapor pressure in pure vapor magnetometers is that smaller, sealed, cells can be used. Such a configuration is shown in figure 3.3.5.

3.3.8.3 *Geometric considerations*

As in a two-chamber nEDM experiment the precession frequency of UCNs in parallel and anti-parallel electric and magnetic fields are measured simultaneously, a drift of a spatially constant magnetic field does not cause an nEDM shift. Instead, the difference between the average magnetic field in the two precession chambers[1] dominates the uncertainty in a single nEDM measurement.

Without using a co-magnetometer, the magnetic field at the position of the UCN chambers has to be reconstructed. Approximating the magnetic field to be rotationally symmetric with respect to the common cylinder axis of the two precession chambers

1 With a small offset as the UCNs do not average over the magnetic field in the precession cells homogeneously (see chapter 3.1)

with the center of the stack being $z = 0$, it can be written $B_z(z) = \sum_n \frac{1}{n!} \frac{\partial^n B}{\partial z^n} z^n$. Using a stack of pure UCN chambers with pure mercury magnetometers, one above and one below the UCN precession chambers, the odd components of the magnetic field of higher order than the linear gradient cause a shift in the nEDM measurement. The shift of the reconstructed magnetic field caused by the even components of the real magnetic field is the same for both UCN chambers.

Using a mercury co-magnetometer instead, the average magnetic field in both cells would be monitored accurately if no electric field was applied. However, with an electric field, the dominating shift in an nEDM measurement is caused by the mercury geometric-phase effect. In general, every component of the magnetic field with $\langle |\boldsymbol{B}| \rangle = 0$, where $\langle\rangle$ indicates averaging over the cell volume, can be corrected well with a co-magnetometer. On the other hand, field components with $\left\langle x B_x + y B_y \right\rangle \neq 0$ cause geometric phases. The shape of the magnetic field in the experiment is thus decisive which kind of magnetometry is better suited to be used to correct magnetic field inhomogeneities in an nEDM experiment.

In principle, instead of just one cell, two cells could be placed one after the other in the laser beam. This way, the difference of the magnetic field at the two positions could be extracted from the beat in the transmission signal. However, as the precessing spins in the first cell would modulate the laser beam intensity with their Larmor frequency, the atoms in the second cell would see a light beam that is modulated with a frequency close their Larmor frequency. Any non-zero light shift would thus cause a near resonant oscillating pseudo-magnetic field in the second cell, which would among other effects, lead to a large shift of the Larmor frequency [88]. Furthermore, the slow precession frequency of mercury atoms makes the period of the beat long. In general, the small bandwidth of mercury magnetometers due to the slow precession frequency limits the magnetic field measurements to low frequencies. In external magnetometry cells (not co-magnetometry with neutrons) it could be possible to mix two different atomic species. If, for example, cesium vapor is added to the same precession cell, a laser-based readout of the cesium atoms could measure high-frequency fluctuations of the magnetic field. The mercury vapor would add the information on slow changes and the absolute value of the magnetic field.

3·4 COMPONENTS OF THE HG-(CO)MAGNETOMETER

Pushing the sensitivity of the magnetic field measurement towards the fundamental sensitivity limit (equation 3.2.6) in a real magnetometer requires efforts in understanding and reducing systematic uncertainties and to optimize the signal to noise ratio of the magnetometer signal. This chapter presents three key projects addressing these efforts.

3.4.1 FREQUENCY LOCK

Typically, when lasers have been frequency locked to a Doppler-free spectroscopy signal of the transition ${}^1S_0 \rightarrow {}^3P_1$, $F = \frac{1}{2}$ in ^{199}Hg, this has been done using techniques that rely on an AOMs or electro-optic modulators (EOMs). In [43], for example, an AOM sweeps the wavelength of a branch of the beam that is used for the frequency lock, around the center of a peak in the spectroscopy signal. The method of homodyne detection[1] then provides a valid error signal with a nonzero slope at the point where the lock is to be established. Hence, a controller can stabilize the laser wavelength at this point.

However, problems arise when AOMs are used. They introduce a fragile point in the laser beam setup where a careful and stable alignment is necessary. Small changes in the laser beam path cause the AOM setup to fail or underperform. As the magnetometer needs to be designed to run for months without frequent measurement-time consuming maintenance, such sensitive points should be avoided if possible.

Additionally, in the AOMs that were tested for this setup[2], more than 90% of the laser power was lost in a double-pass setup. Having the light pass the AOM twice, however, is necessary to avoid a dependence of the angle between the initial- and the shifted laser beam on the extent of the frequency shift.

Techniques to stabilize the laser light frequency without the need to modulate it have been investigated and optimized for feasibility, accuracy, and robustness in an nEDM experiment and are discussed in the following sections.

3.4.1.1 *Locking to a saturation spectroscopy signal*

In a first approach to build a static Doppler-free frequency lock that does not need wavelength modulation, the dichroic atomic vapor laser lock (DAVLL) technique was applied to a signal obtained with Doppler-free saturation spectroscopy. A more detailed description of this spectroscopy technique is given in section 2.3.1.

A magnetic field created by Helmholtz coils in the spectroscopy cell introduces a wavelength-dependent circular dichroism in the atomic vapor for the readout light.

1 See [43] for details
2 Brimrose, Model QZF-150-50-254.

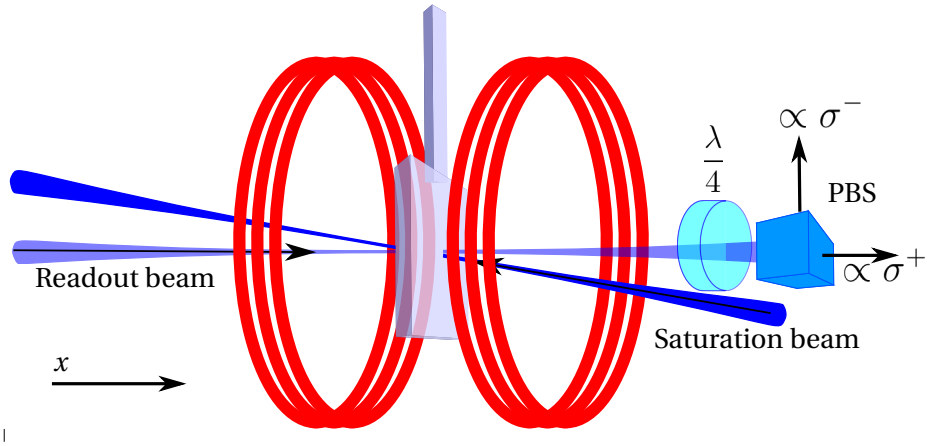

Figure 3.4.1: Doppler-free saturation spectroscopy setup. The laser beams overlap inside the spectroscopy cell in the center of this figure. The coils that create the magnetic field are illustrated in red. The whole setup is described in the main text.

Saturation- and readout beam are both linearly polarized initially. After passing the spectroscopy cell, the probe beam is split into two components whose intensities are proportional to the σ^+ and the σ^- component of the transmitted probe beam. This is achieved by using a quarter-wave plate followed by a polarizing beam splitter cube as shown in figure 3.4.1.

Subtraction of the resulting two intensity signals yields a dispersive error signal allowing to lock the laser frequency to any point on the central slope. The transmitted intensities of the circular components over the detuning of the laser frequency from resonance are shown in figures 3.4.2a and 3.4.2b. Subtracting the two signals produces the error signal shown in figure 3.4.2c. A first laser lock that used a similar technique with cesium vapor is described in [104].

Although a robust frequency lock to the magnetometer transition in mercury is feasible with this setup [105], it is not optimal for the purpose of locking the laser to the NLP. This point is ≈8 MHz away from the center of the transition, and the width of the Doppler-free features is typically about the same size as this offset.

Consequently, it is not easy to get the dynamic range of the error signal large enough to include the NLP. Additionally, an error signal which allows to lock the laser not near the edge but to the center of the dynamic range would be preferable.

By removing the waveplate and the polarizing beam-splitter (PBS) cube, the signal becomes symmetric again, but now with two dynamic ranges where the laser could be locked, one, on each side of the center of the transition. Taking out these two optical components results in the same signal as adding, instead of subtracting, the σ^+ and the σ^- component of the transmitted probe beam. An example for this is shown in figure 3.4.2d. Now the center of the dynamic range, which is interesting for the lock, is shifted away from the center of the undisturbed transition.

With this technique it is possible to tune the signal such that the NLP is roughly in the middle of this dynamic range. A larger magnetic field shifts the two outer features to the sides while it leaves the feature in the center unaffected. Consequently, Zeeman-

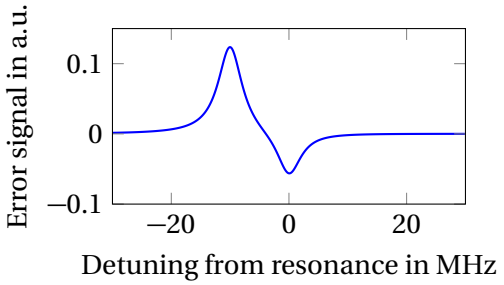

(a) Transmission signal of the σ^- component in the readout beam.

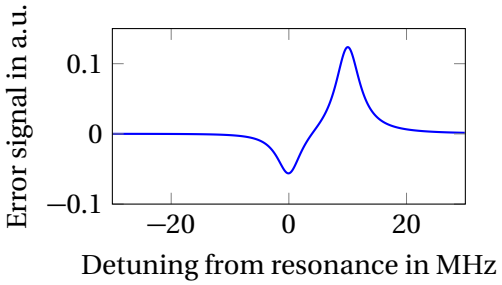

(b) Transmission signal of the σ^+ component in the readout beam.

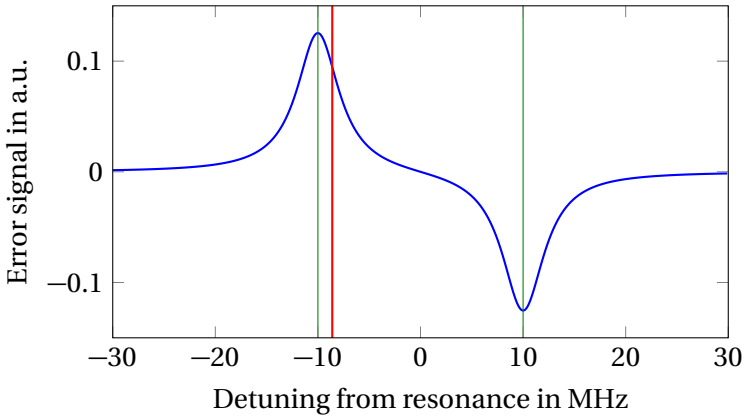

(c) Differential transmission signal $\sigma^- - \sigma^+$

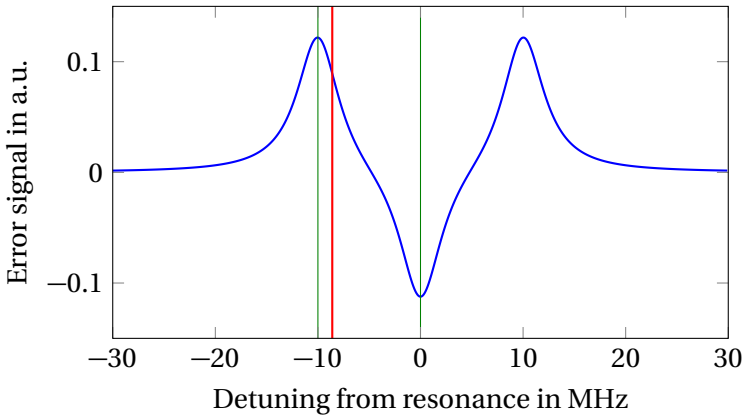

(d) Total transmission signal $\sigma^- + \sigma^+$

Figure 3.4.2: Error signal in different spectroscopic arrangements. (a) and (b) show the transmission of the σ^+ and σ^- components, while (c) and (d) show the subtraction and the sum of the two components. The red line marks the NLP and the green lines the dynamic range.

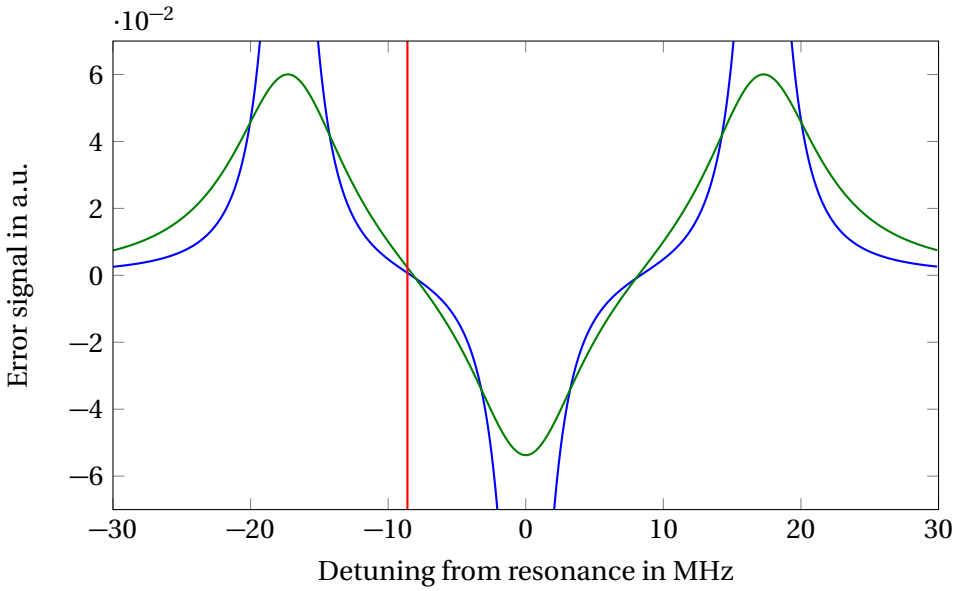

Figure 3.4.3: Two error signals with the same Zeeman-splitting and different widths of the Doppler-free features. The red line indicates the NLP. The magnetic field is chosen such that the NLP is in the center of the dynamic range.

shifting the left feature by two times the distance between the NLP and the center of the transition yields an error signal that is centered around the NLP.

However, if the spectroscopic features are too narrow, the signal is almost flat at this point and thus not useful for a locking algorithm. This situation is shown in figure 3.4.3 as a blue line. On the other hand, the slope of the error signal at the NLP can be increased by making the Doppler-free features broader. A variety of effects that broaden the Doppler-free features are described in chapter 2.4. Especially the angle between pump- and probe beam is a useful handle to deliberately increase the width of these features and set it very accurately. The green line in figure 3.4.3 shows a signal that is produced with the same pump and readout beams as the blue one, but with a larger angle between them. The slope of this artificially broadened signal is larger at the NLP than that of the narrower signal.

The steepest slope of a Lorentzian can be found at a distance of $\frac{\sqrt{3}}{6}$ times its width from the center. For the slope of an error signal containing the subtraction of two Lorentzians to be maximized, the distance between the two features consequently has to be $\frac{1}{\sqrt{3}}$ times their width. The same arguments lead to a optimal distance between two Gaussians of $\frac{1}{2}$ times their width. Therefore, depending on the mechanisms the Doppler-free features are broadened by, the optimal width of the signals is somewhere between $\sqrt{3}$ and 2 times the distance between the Doppler-free features.

This shows that the choice of the magnetic field in the spectroscopy and the width of the features provide independent ways to center the dynamic range around the frequency the laser shall be locked to and to optimize the slope of the error signal at this point for the given shift.

A down side of this is that the more a signal is broadened the smaller it gets. This reduces the SNR that can be achieved for any given shift of the center of the dynamic

range when that shift is increased. As the steepest slope achievable in a Lorentzian as well as in a Gaussian scales inversely proportional with their widths, increasing the dynamic range by a factor of two, reduces the SNR and consequently the accuracy of the frequency lock by a factor of two.

However, as the NLP is less then 10 MHz away in mercury vapor with low pressures and the width of the Doppler-free features is typically not much smaller than that, this technique can be used for co-magnetometry in an nEDM experiment.

To get rid of the background, a transmission signal of a reference beam is subtracted from the spectroscopy signal. It passes the spectroscopy cell but does not overlap the pump beam inside the atomic vapor. Hence it allows to cancel or at least to reduce the Doppler-broadened background from the resulting signal without affecting the Doppler-free features.

3.4.1.1.1 *The locking routine*

The ability of producing and interpreting spectroscopic pictures with an automatic system enables a more flexible and robust frequency lock.

When a lock is to be established, a wavelengthmeter is used to perform a first, coarse, tuning of the laser to the right wavelength. Then, a spectrum of the Doppler-broadened peaks is recorded and fitted. From this fit, the position of the Doppler-broadened feature containing the magnetometer transition in ^{199}Hg and ^{204}Hg is determined, the spectroscopy zooms in on these two transitions, and a Doppler-free spectrum is recorded.

A fit to this spectrum determines the positions of the ^{199}Hg and the ^{204}Hg transition more accurately. The distance between these is inherent to the isotopes and does not change with environmental parameters. It can thus serve as a calibration source for the frequency axis of every spectrum containing both peaks. This is necessary as the only information for the x-axis in these spectra is the triangular Voltage applied to the piezo in the seed laser (see section 2.2.1 for details) to sweep the lasers frequency. Only after conversion of the x-axis to the frequency of the laser light, the position of the NLP in the spectrum can be determined. A measurement of the relative isotope shift between ^{199}Hg and ^{204}Hg is described in section 2.5.2. Precise knowledge of this is important as any uncertainty causes a systematic shift of the frequency axis calibration and thus a light shift. This is shown in section 3.3.1. A proportional-integral-derivative (PID) controller then stabilizes the laser frequency to this point.

Once the lock is established, it is important to keep the error signal inside the dynamic range. If for example the probe beam is blocked for a short time, the PID would try to bring the error signal back to where it was locked and rush out of the dynamic range. When the blocking is removed again, the controller cannot bring the laser frequency back to the NLP anymore and the lock is lost.

To avoid this, a window limits the PID to work only inside the dynamic range and to ignore signals that are not inside this window. However, as the dynamic range is small compared to long-term drifts of the system, the PID controller needs to be allowed to walk the piezo voltage to values that are outside the window as it was initially defined for it to be able to keep the laser locked to the NLP. To account for this, the center of the window is constantly redefined by a software controller that effectively applies a

low pass filter to the error signal. Fast and large disturbances, like someone blocking the laser beam or heavy concussion of the locking setup, will thus be ignored by the frequency lock. While this will, inevitably, result in reduced accuracy for the duration of the disturbance, the accuracy will be restored immediately afterwards. A schematic illustration of this dynamic frequency lock is shown in figure 3.4.4. An example of the error signal recorded in three different conditions is shown in figure 3.4.5. In figure 3.4.5a, the frequency was not stabilized, while in figure 3.4.5b the frequency is stabilized under usual laboratory conditions. In figure 3.4.5c, the lock was engaged, like in 3.4.5b, but the breadboard the setup was mounted on was knocked on manually. In case the lock is lost anyway, the locking routine can automatically determine the locking point as described above and lock the laser from scratch. To avoid malfunctions that are not recognized by the locking routine, the locking routine pauses the lock to record and save a spectrum in appropriate moments (when the experiment does not need the laser to be frequency locked). In case there was a large disturbance that caused the lock to jump to a different Doppler-free feature during a period where the lock was established, this would be revealed in hindsight by the spectrum recorded at the end.

3.4.1.1.2 *Evaluation of the saturation spectroscopy lock*

An evaluation of the stability of a frequency lock using saturation spectroscopy as described above can be found in [98]. In the described test setup, two probe beams passed the same vapor cell, but only one of them had an overlap with the preparation beam. The difference between the two probe beam signals was used to get the full Doppler-free features on a reduced background.

Fluctuations of the error signal indicated statistical fluctuations of the laser light frequency within 1σ of 1.7 MHz in this measurement.

To determine the accuracy of finding the locking point before the wavelength lock is established, a series of 100 spectra was recorded and fitted. The distance $\delta V_{199-204}$ between the features caused by the two isotopes for each of these spectra is shown in figure 3.4.6.

The relative statistical uncertainty of the distance between the isotopes is 0.0031. When a lock is to be established, a spectrum is recorded and fitted. The x-position of the NLP can than be determined at least with the same accuracy as the relative uncertainty between the two isotopes. The model that was fitted to the signal is then used to determine the voltage the error signal has to be locked to. In absolute numbers, the statistical accuracy of locking the laser to the NLP is then 0.3 MHz. However, by repeating this procedure N times, this uncertainty can be reduced by a factor $\frac{1}{\sqrt{N}}$.

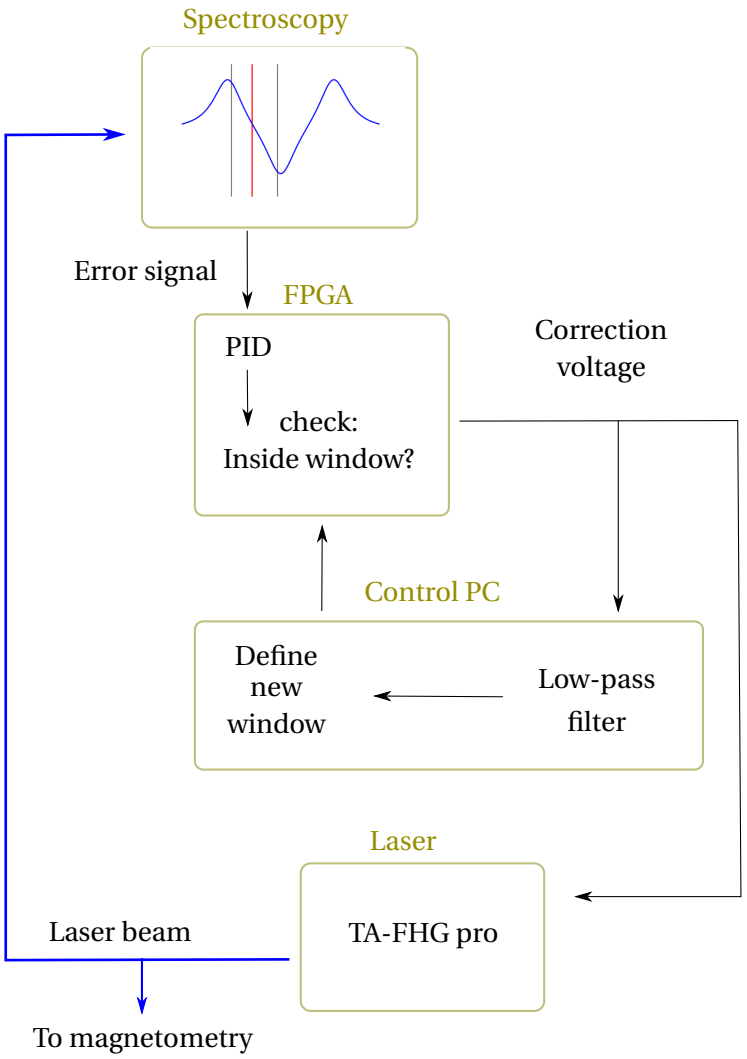

Figure 3.4.4: Protection of the dynamic frequency lock against malfunction in adverse conditions. The output of the PID is limited to make sure that the error signal stays within the dynamic range. To account for drifts, the window follows the locking point as described in the text.

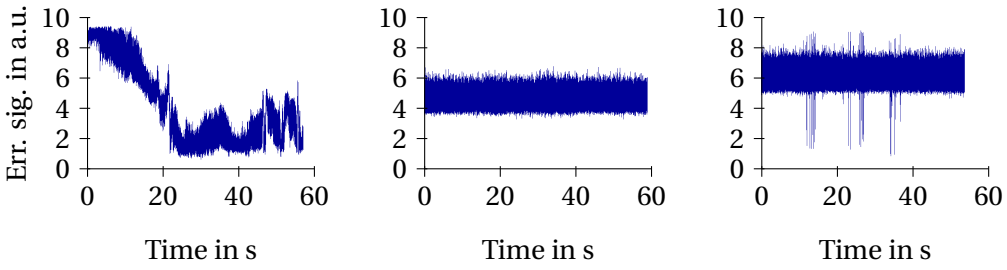

(a) Error signal while the laser is not locked.

(b) Error signal while the laser is locked in normal conditions.

(c) Error signal while the laser is locked with knocking on the laser table and wiping through the spectroscopy beam.

Figure 3.4.5: Error signal of the frequency lock in different conditions.

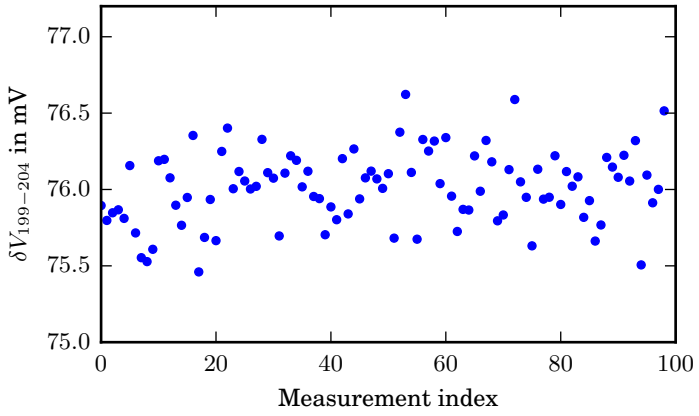

Figure 3.4.6: Series of 100 measurements of the difference between the features caused by ^{199}Hg and ^{204}Hg. This is used to estimate the accuracy of locking the laser to the NLP.

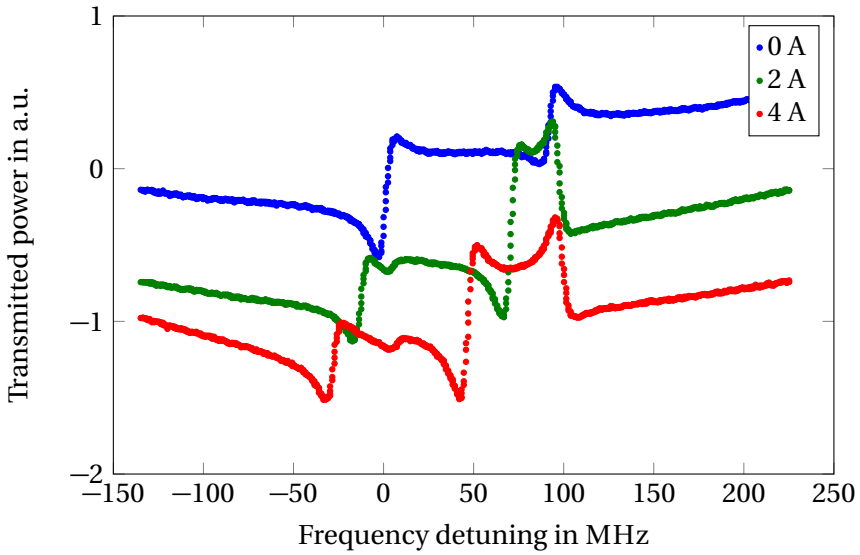

Figure 3.4.7: Polarization spectroscopy signal for the frequency lock recorded in different magnetic fields. The magnetic field (expressed as current in the field coil in A) shifts the error signal as described in the text.

3.4.1.2 *Locking to a polarization spectroscopy signal*

Another way to produce the signal to lock the laser frequency to is polarization spectroscopy. This technique is described in more detail in section 2.3.2. The advantage is that Doppler-free signals on a very low Doppler-broadened background can be produced. A locking procedure can profit from that in two ways. For one thing, it becomes less sensitive to intensity fluctuations caused by the intensity of the laser beam itself and from fluctuations caused by mechanical vibrations or drifts. For another thing, the photodiode signal can be amplified more without the need to subtract a large offset.

Figure 3.4.7 shows a signal that was recorded with polarization spectroscopy in three different magnetic fields. The preparation beam is circularly polarized and the probe beam polarization is detuned by an appropriate angle to produce a dispersive signal for the $\Delta m = -1$ transition. When the magnetic field is increased, the dispersive feature is shifted to the left. This allows to choose where to center the dynamic range the PID can lock the laser frequency to. Besides making it possible to center this dynamic range around the NLP without having to broaden the transitions and thus reducing the slope of the signal, this allows to lock the laser to any frequency in the range approximately from −50 MHz to 150 MHz around the NLP. This allows to measure the light-shift curve of mercury vapor in an EDM experiment by locking the laser to different frequencies in the range given above while the magnetic field is monitored with another magnetometer, and measuring the impact of the readout light on the precession frequency of the atoms.

Another large advantage of this technique for a lock to the NLP is that narrower Doppler-free features can be used. As shown above, the slope of the error signal scales inversely proportional to the width of the contributing features. Instead of broadening

the features as needed for optimal operation of the lock to the saturation spectroscopy signal, the features can be made as narrow as possible.

3.4.1.3 *Summary of static locking techniques with Doppler-free signals*

Locking the laser as described in [105] is possible, but the NLP is not in the center of the dynamic range. To have some dynamic range on the left side of the NLP, the left feature has to be shifted further than the NLP. As the right feature is shifted by the same amount, the large relative shift between the two features makes the slope small.

The new technique, shown in figure 3.4.3, has a feature that is not shifted by the magnetic field. It thus reduces the relative shift between the the two features that form the error signal by a factor of two. Additionally, the NLP can be put into the center of this dynamic range by shifting the left feature exactly by two times the NLP. The slope of the error signal at the position of the NLP can be maximized by increasing the width of the Dopper-free features.

Because this still needs a rather large relative shift between the Doppler-free features, the maximal achievable slope is limited. Polarization spectroscopy solves this problem, as the whole error signal can be shifted by adjusting the magnetic field accordingly. The slope of the signal is thus nearly independent from the exact position the laser is to be locked to.

3.4.2 READOUT

In addition to fluctuations of the light power produced by the laser itself, further noise sources for the readout signal are potential mechanical noise and electrical noise added in the photodiode amplification circuit.

Mechanical noise is caused by motion of the laser beam with respect to the optical components. If the light hits some of the components near the edge of their optical aperture, and gets partially clipped, or if there are optical imperfections like dust particles in the beam path, mechanical movement causes fluctuations of the transmitted laser power. For all optical components that are close to the laser source, the mechanical noise can be reduced by a careful alignment of the beam and a clean environment. For the readout of the magnetometer, however, special care has to be taken in order to account for this.

As the laser travels more than 4 m through the shielded room, small angle fluctuations of the laser entering the shielded room can cause relatively large displacements of the laser beam at the place where it is detected. One possibility to reduce this effect is to use optical fibers [75], but it was found that using potentially problematic fibers can be avoided by implementing large scale photodiodes[3] with an active area of 5.8 mm × 5.8 mm behind an anti-reflection coated plano-convex lens with a diameter of 5 cm.

3 Hamamatsu S1337-66BQ

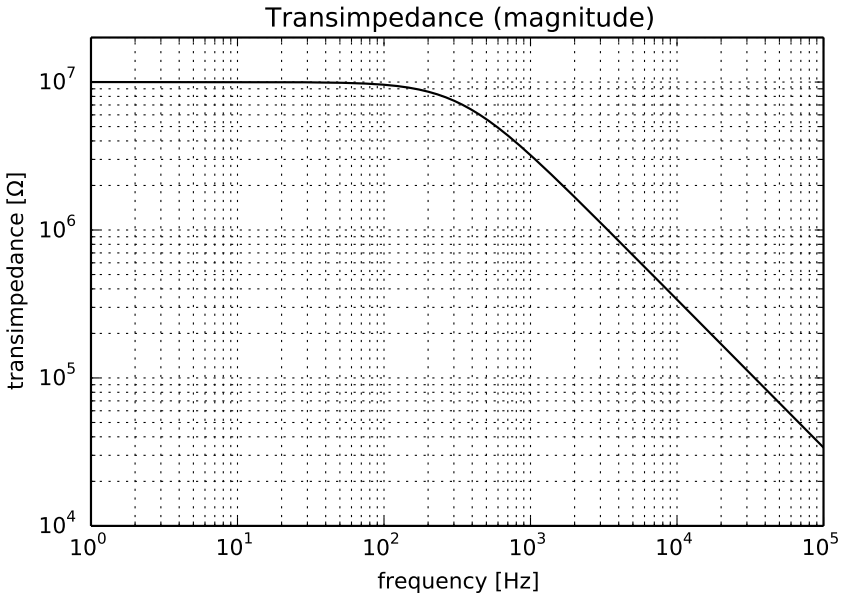

Figure 3.4.8: Transfer function of the transimpedance amplifier stage. Taken from [96].

The photodiode is intentionally not placed exactly in the focal point of the lens. If there are imperfections or dirt on the photodiode, spreading the light on a larger surface makes the readout more robust to mechanical vibrations of the laser beam.

A problem that typically comes with large active areas of photodiodes is that, due to the higher capacity, the bandwidth of the readout is limited to smaller frequencies. However, the preamplification circuit for these photodiodes, which was designed for this project and is discussed in more detail in [96], achieves a corner frequency of 337 Hz while the precession frequency of the mercury atoms in a 1 µT field is 7.71 Hz. Figure 3.4.8 shows the whole transfer function of the transimpedance amplifier.

As the DC component of the transmitted laser power does not carry any information about the magnetic field, it is discarded by a high pass filter with a very small corner frequency that leaves frequencies above 0.1 Hz unaffected. The resulting AC signal is amplified again to achieve voltages without a DC offset and a transimpedance amplification of 23.2 $\mathrm{V\,\mu W^{-1}}$. All these components are implemented on the same printed circuit board (PCB) as the photodiode and housed in a massive aluminum shield. As the photodiode is not solar blind, this housing was build to be light tight. In front of the photodiode, a light-thight lens tube carrying an optical band pass filter[4] is mounted to the aluminum housing. A picture of the readout setup and the high pass filter transfer function and step response are shown in section B.

This filter transmits only about 25% of the readout light which reduces the overall conversion factor of the readout to roughly 7 $\mathrm{V\,\mu W^{-1}}$, but it also blocks any stray light that is present in the environment. A signal that was recorded with this setup is shown in figure 3.4.9.

4 Asahi Spectra XBPA254

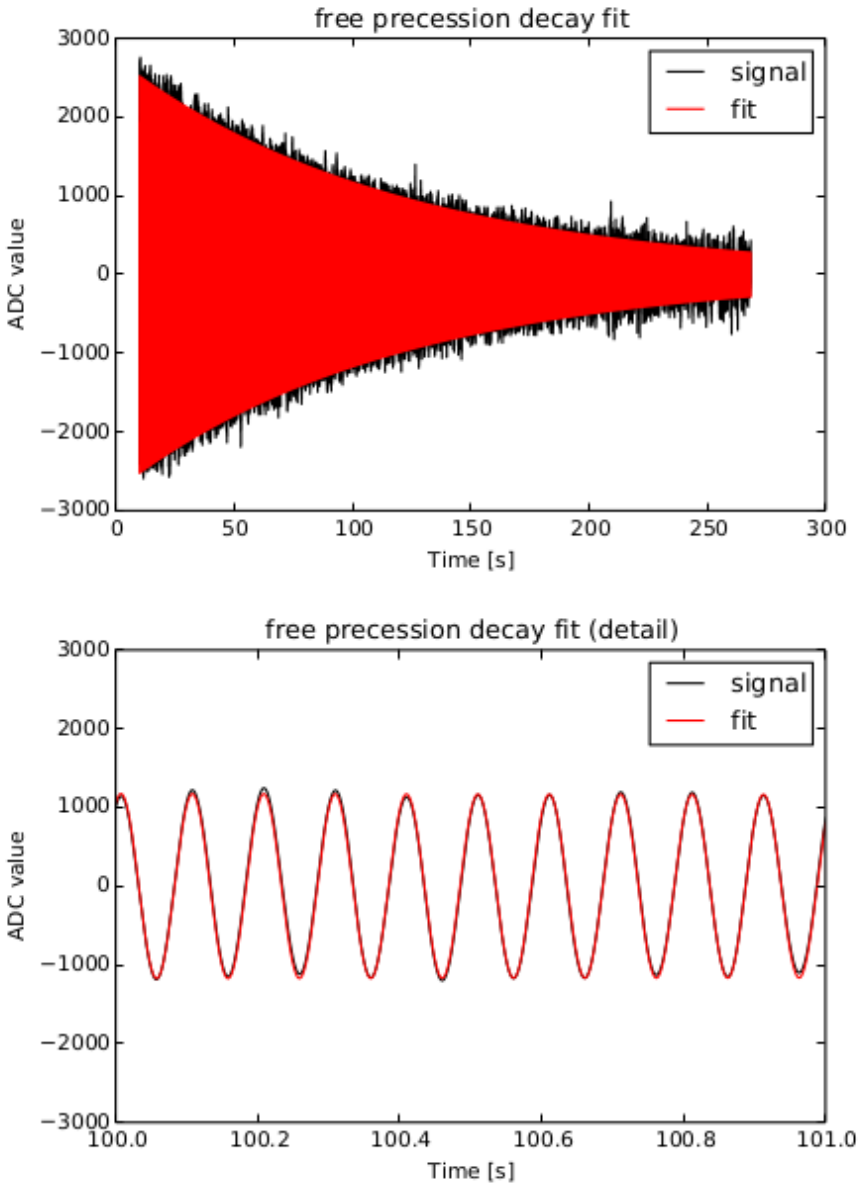

Figure 3.4.9: Raw signal of the ^{199}Hg magnetometer recorded with the readout presented in this section. The figure is taken from [96].

Another important figure when the readout is used in mercury vapor magnetometry is the dark noise of the board. The readout electronics were designed for an input power equivalent of a theoretical dark noise (Johnson noise) of 6.2 pW for the bandwidth of 337 Hz. This dominates over the photon shot noise for light intensities that are smaller than 20 nW. In [96] was shown that the real dark noise of the whole amplifier corresponds to an input power noise of less than 1.73×10^{-11} W which is roughly the same as the photon shot noise that is caused by a 100 nW readout beam. Being able to use a low-power readout beam without being dominated by dark noise is beneficial to relax systematic effects that are described in section 3.3.1. Further information and characterization measurements of the readout electronics can be found in [96].

Linearly polarized readout

Although a readout with frequency detuned linearly polarized light like in [99] is not possible in a co-magnetometer as the rotation of the linear polarization vector would be too small [75], it is worth considering to use an absorptive readout with linearly polarized light that is frequency locked to the NLP. This means, that linearly instead of circularly polarized light would be sent through the cell to read out the precession. Behind the cell, the laser beam has to be decomposed with a $\frac{\lambda}{4}$ waveplate and a PBS in two components that are proportional to the two circular components σ^+ and σ^- that add up to the linear polarization initially. As the absorption for σ^+ and σ^- is maximal and minimal for opposite orientations of the rotating atomic polarization, both signals are modulated with the Larmor frequency and phase shifted by π relative to each other.

Subtracting these two components leads to a signal with the same amplitude as the transmission signal of a circularly polarized laser beam with the same power. The linearly polarized beam, however, has the advantage that the light shift effect would be suppressed further. Assuming that a linear polarization of 90% can be transferred into the vapor cell, the light shift would be suppressed by a factor of 10. Another advantage would be that common-noise in the two channels is reduced. A disadvantage of this technique is the fact that the light has to go through more optical components which reduces the amplitude of the signal and potentially adds noise due to a relative movement of the laser beam to the optical components.

Another option for the detection of the linearly polarized readout light would be to use a polarizing beam splitter with the optical axis oriented parallel to the polarization of the undisturbed linearly polarized readout light (for example, the s-component). If the laser frequency is locked to the NLP, absorption has a larger effect on the transmitted light than rotation. Every time the atomic polarization is aligned parallel or antiparallel to the laser beam, the transmitted light has a large circularly polarized component. When the atomic polarization is perpendicular to the direction of the laser beam, the transmitted beam is still linearly polarized.

Monitoring the p-component of the polarization behind the beam splitter thus results in a sinusoidal signal with a frequency of two times the Larmor frequency. Compared to the transmission signal of a circularly polarized laser beam of the same power, the amplitude for this readout scheme is reduced by a factor of four. However, the background is reduced as well. How much the background can be reduced depends on the

degree of linear polarization of the readout beam and how much it is reduced by the optical components. Besides reducing the laser intensity noise, a smaller background intensity also leads to a smaller shot noise (see section 3.2.3).

3.4.3 POWER STABILIZATION OF THE LASER SYSTEM

Fluctuations of the laser power introduce uncertainties and noise in a mercury magnetometer in various ways. They directly contribute to the noise on the readout signal as the laser power transmitted through the vapor cell changes proportional to the input power. Additionally, the spectroscopy signal that is used to stabilize the wavelength of the laser changes with fluctuations of the laser power and can thus translate them to frequency fluctuations. The importance of a stable laser wavelength was shown in chapter 3.3.

To stabilize the output power of the laser system, a pickup of the laser beam is monitored by a photo diode that is mounted to a DC preamplifier board, and the signal is fed to a PID algorithm. As the laser system uses a tapered amplifier (TA), the output of this PID can be used to modulate the the current applied to the TA. This way, the laser intensity can be adjusted independent from the wavelength.

3.4.3.1 *Photodiode preamplifier board*

The same photodiodes and optical filters as the ones that are used in the magnetometer readout are mounted on a two-stage preamplification board which is again housed in a light tight aluminum shield. A transimpedance amplifier is placed close to the photodiode with a transimpedance of 10 MΩ for frequencies that are smaller than 1.5 kHz. At this point the gain has dropped by -3dB (See fig C.1).

The feedback resistor is specified to have a temperature dependence below 5×10^{-5} ppm/°C. In an experiment with a temperature stabilization that keeps temperature fluctuations below 0.1 K, relative drifts of the error signal due to the feedback resistor are thus smaller than 5 ppm. To reduce mechanical noise in the power stabilization, the beam that is used for this purpose is split from the main beam shortly after the laser. This reduces the chance for the beam to interact with optical imperfections. Additionally, large photodiodes are used to reduce clipping of the beam. This is important because individual fluctuations of the laser power that is monitored by this setup would lead to fluctuations of the laser power in the rest of the setup.

A second stage amplifies this signal by a factor of ten. The whole schematic of the preamplifier board is shown in figure C.2.

Figure 3.4.10 shows the Allan deviation of the error signal in the intensity lock. The noise reduction becomes effective for timescales that are longer than milliseconds as is expected from the frequency response of the preamplifier. The stability of this setup is expected to be dominated by the temperature stability of the readout.

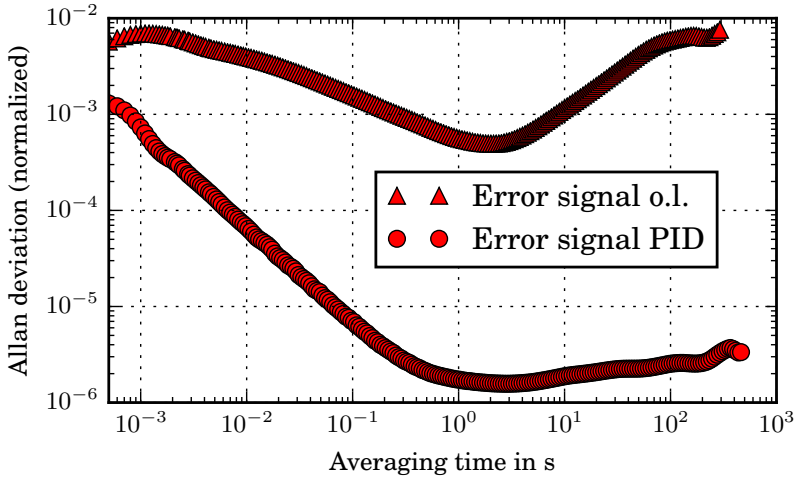

Figure 3.4.10: Allan deviation of the error signal in the power stabilization with (PID) and without (o.l.) the lock established. The label “normalized” means that the values are given relative to the total power of the signals.Taken from [103].

3·5 SHIELDING FACTOR MEASUREMENT WITH A MERCURY MAGNETOMETER

To achieve a spatially and temporally homogeneous magnetic field inside the precession chamber, besides creation of the field with a careful arrangement of field coils [107] and a high stability of the current supplies feeding these coils, the external field has to be shielded from penetrating into the experimental volume.

The nEDM apparatus in Munich uses two complementary strategies to reduce external disturbances. In a first step, slow changes of the external magnetic field in the experimental area are compensated with a surrounding-field compensation (SFC). All together, 24 large coils enclose a volume of $9 \times 6 \times 6\,\mathrm{m}$ around the whole experiment. With 180 fluxgates being distributed inside this volume, fluctuations of the magnetic field in the experimental area can be monitored and reduced actively with a feedback to the large coils [72].

Passive shielding is achieved with several layers of a highly magnetizable metal (magnifer®[1]) sheets grouped to an outer shield or MSR and an inner shield or insert (see figure 3.5.1) [108]. To achieve small fields and gradients inside the shielding, the remanent magnetization of the magnifer® layers is reduced with a technique that has been developed for this experiment [109].

The MSR with inner dimensions $2.3 \times 2.5 \times 2.8\,\mathrm{m}^3$ contains a layer of aluminum to shield the inside form high frequency noise additionally to the magnifer® sheets. A large door allows users to walk in and to bring in and work on pre-assembled experiments or to set up experiments in the MSR. For better passive shielding, experiments can be fixed to the rear wall of the MSR and the insert is guided into the room and around the experiment on rails through the large door. The insert also contains the field coils to produce static and alternating fields for a Ramsey measurement.

The most important figure of merit besides spacial homogeneity and temporal stability of the field created by the coils in the insert, is passive damping of fluctuations of external magnetic fields. The ratio of the amplitude of a sinusoidal magnetic field fluctuation outside the magnetic shield and its remainders inside the shield is called shielding factor. It depends on the frequency of the perturbation and has been measured with different magnetometers for the shield in Munich [106]. The mercury magnetometer has been used to measure the shielding factor for very small frequencies.

3.5.1 MEASUREMENT SETUP

Coaxial holes through the MSR and the insert make it possible to send laser beams in a straight line through the whole experiment. There are four of these straight paths that are arranged along a vertical line in the center of the MSR. These holes can be used to send laser beams through the shield that polarize and read out mercury vapor cells in-

1 Krupp Magnifer 7904 is used in this shield

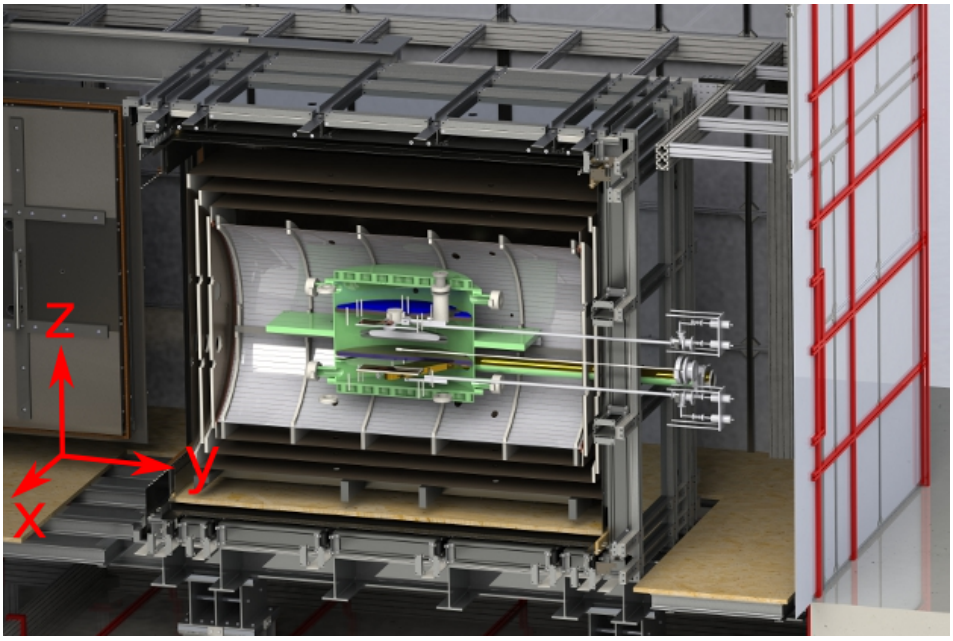

Figure 3.5.1: Cut through the MSR, the insert, and a fraction of the large coils which are part of the SFC. Inside the insert, a vacuum chamber for an nEDM experiment is shown. Taken from [106].

side the insert. The beams traverse the shield in x-direction as shown in figure 3.5.1. To measure the shielding factor, a mercury vapor cell in the center of the x-y-plane, and slightly lower than the center in z-direction, was used. For an independent field measurement, a SQUID magnetometer, that was provided by the Physikalisch-Technische Bundesanstalt Berlin (PTB Berlin), was placed approximately 15 cm above the mercury cell.

The vapor cell was cylindrical with a length of 10 cm and a radius of 5 cm. Its body is made from quartz with the laser beams passing through the flat faces. To the sides, two nonmagnetic glass valves are attached via a graded seal tube.

Two different coatings for the cell walls were tested to reduce the depolarization rate: fomblin oil and paraffin. Both wall coatings resulted in a similar typical decay time of ~120 seconds. However, as the fomblin oil slowly ran down the walls of the cell and accumulated on the bottom, the decay time degraded over the course of a day. Paraffin was more practical as it sticks to the walls. To coat the cell with paraffin, droplets were chased over the whole surface inside the cell while it was heated. A side-view of the cell is shown in figure 3.5.2. The flat windows through which the laser beams pass along the cylindrical axis of the cell are omitted in the process of chasing the liquid paraffin through the cell to make sure that their optical properties are not impaired. A view through these flat windows is shown in figure 3.5.3. To fill the cell, it was hooked to a vacuum pump and evacuated for several days. Then, a mercury reservoir was opened to release mercury vapor into the cell. After closing the reservoir, the cell was evacuated again until the density of atoms inside was appropriate in terms of absorption of the readout beam.

Figure 3.5.2: Side view of the all-quartz cell that was used as precession cell in the shielding factor measurement. The empty cell was provided by Timothy E. Chupp from the University of Michigan. The quartz was visibly coated with paraffin.

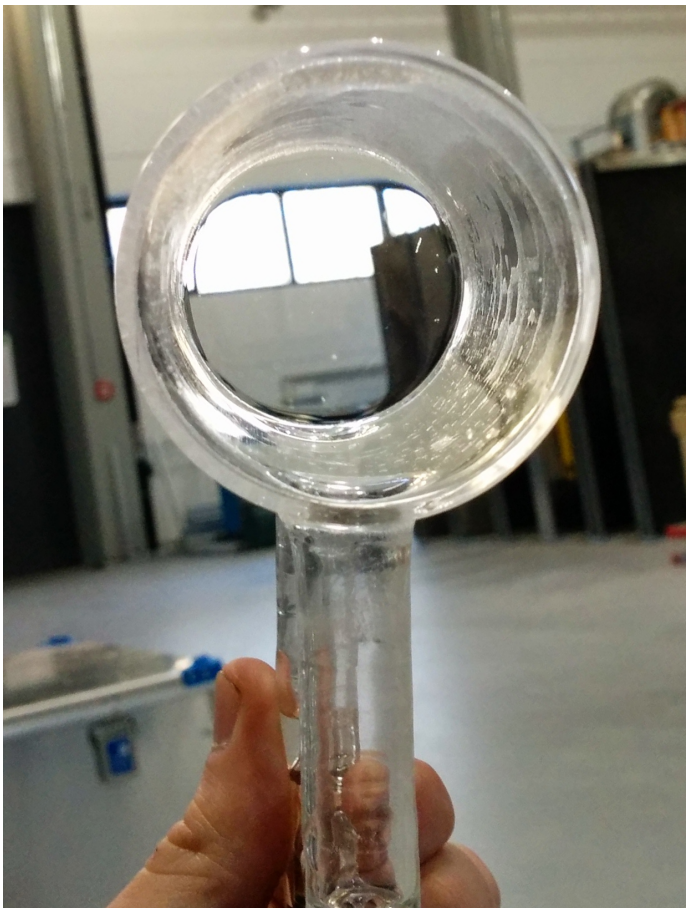

Figure 3.5.3: The same cell as in figure 3.5.2, but viewed along the cylinder axis. To allow the laser beams to traverse the cell, no thick paraffin coating is applied to the optical windows.

The two laser beams that are used to pump and probe the magnetization of the mercury vapor went through the same holes in the shield and windows in the vapor cell, but there was a small angle between them. This is important to reduce the amount of stray light from the pumping beam that reaches and saturates the readout as it has $10^3 - 10^4$ times more power than the readout beam.

A known external sinusoidal perturbation was applied using the SFC in the same direction as an internal holding field. Before the magnetic shields were installed, the field created by the SFC at the center of the experimental volume without any shielding in place had been measured [106]. The mercury magnetometer and the SQUID magnetometer measure the sum of the holding field and the fraction of the external field that penetrates into the shield. This was done for the two axis (z and y) that are perpendicular to the laser beams. For these directions, the circularly polarized pumping and probing beam can polarize the vapor with transverse optical pumping and monitor the precession by observing the transmitted intensity. As the absolute value of the magnetic field was not important, the laser frequency was not locked to the NLP in a Doppler-free spectroscopy, but to the side of the ^{199}Hg peak in the Doppler-broadened spectrum. Assuming an uncertainty of the angle between the magnetic field and the laser beam of 5 mrad, the light shift effect can lead to a shift in the magnetic field measurement of 400 fT. The uncertainty of the angle between the magnetic field and the laser beam will be smaller in the final experiment. However, at the time of the shielding factor measurement, the trim coils for the holding field had not been configured yet.

3.5.2 FREQUENCY RESPONSE

Due to the long averaging time in a typical free precession decay measurement with mercury, alternating magnetic fields can only be measured with accurate results for their amplitude and phase if they are alternating with a period that is long compared to the averaging time.

Results of a simulation of this system are shown in figure 3.5.4. Frequency response and phase shift caused by the averaging are given as functions of the ratio of the averaging time and the cycle length of the measured sinusoidal signal. After having measured the alternating field inside the shield with the mercury magnetometer, results from this simulation were used to reconstruct the actual from the observed amplitude.

3.5.3 RESULTS

A time series of a field measurement with mercury during one of the shielding-factor measurement runs is shown in figure 3.5.5. For this measurement, a 1 mHz sinusoidal field with a $(10.6 \pm 0.1)\,\mu$T amplitude[2] was applied in the y-direction with the SFC. After polarizing the mercury vapor, the precession was monitored for 120 s before a new burst of the preparation beam polarized the vapor again. This procedure was repeated for several thousand seconds to record at least five periods of the external perturbation.

2 The field created by the SFC would have this amplitude at the position of the mercury magnetometer if there was no MSR.

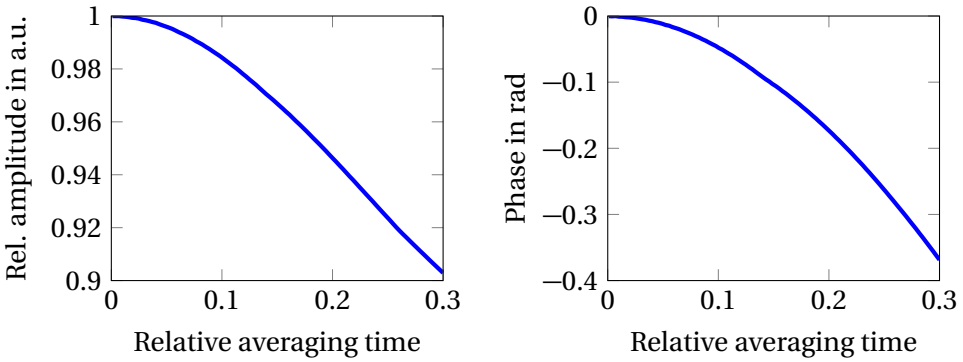

(a) Amplitude measured with the mercury magnetometer divided by the actual amplitude.

(b) Phase between the signal measured with the mercury magnetometer and the actual field.

Figure 3.5.4: Effect of averaging on the measurement of a sinusoidal magnetic field.

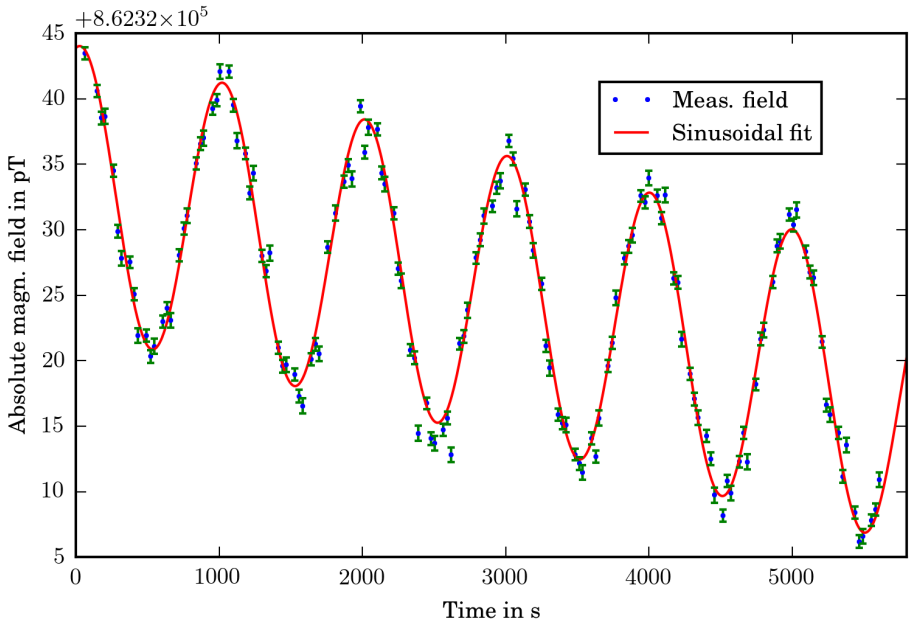

Figure 3.5.5: Magnetic field measured with the mercury magnetometer during the shielding factor measurement. The holding field is 0.86 µT.

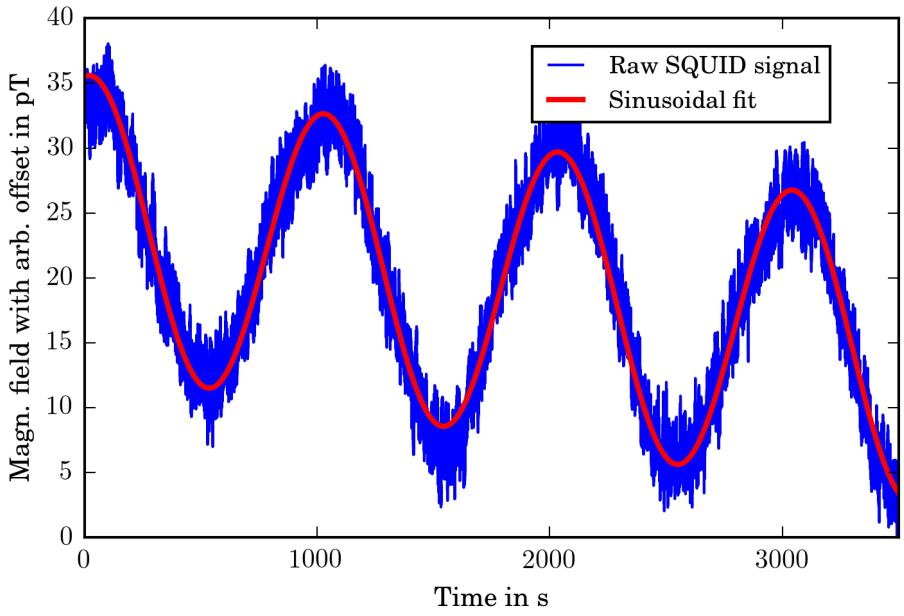

Figure 3.5.6: Magnetic field measured with the SQUID magnetometer during the shielding factor measurement. A problem with the data acquisition caused the measurement to stop after ~3500 s.

Each 120 s long decay signal was split into three parts that were fitted individually providing three independent magnetic field measurements per decay.

The measured alternating field inside the MSR has a much smaller amplitude than the field applied outside and an obvious linear drift. Parallel to the measurement with mercury, the SQUID system recorded the y-direction of the magnetic field approximately 15 cm above the mercury vapor cell. The resulting measured field in y-direction is shown in figure 3.5.6. A sinusoidal signal with a constant drift is fitted to both time series individually.

For the mercury signal, the amplitude resulting from the fit is (10.87 ± 0.02) pT. Corrected for averaging, the amplitude of the real field becomes (10.92 ± 0.02) pT.

The same model is fitted to the signal that was measured with the SQUID. Here, the factor that converts the voltage provided by the SQUID electronics to a magnetic field is known with an accuracy of 5% [110]. This dominates the uncertainty of the amplitude measurement with the SQUID system of (11.30 ± 0.57) pT.

It should be noted that even though the results measured with mercury and with the SQUID are compatible, the two magnetometers are not expected to measure exactly the same field because of the different positions of the two magnetometers and the fact that the mercury magnetometer measures the absolute value of the magnetic field, while the SQUID magnetometer detects only the z-component of the magnetic field. However, the difference expected from these effects is smaller than the uncertainty of the SQUID measurement.

The shielding factor in y-direction for fluctuations with a frequency of 1 mHz and amplitudes around 5 µT determined with the mercury magnetometer is thus 97 ± 1 k.

While the SQUID system is a good choice for detecting relative changes of high frequency magnetic fields, the mercury magnetometer measures the absolute value of the field with a high accuracy but is restricted to low frequencies. Combining both systems provides a good overall picture of the magnetic field.

This symbiosis is also beneficial in systems combining high pressure noble gas vapors with SQUID systems. Here, the SQUIDs monitor the precession of the magnetization in the vapor. However, the high magnetization that is needed for a good signal make this systems more invasive than the low pressure mercury vapor and cause them to be prone to systematic effects like interaction between the rotating macroscopic magnetization and the atoms.

The same measurement was done for the z-direction. With an external amplitude of $(16.20 \pm 0.16)\,\mu\mathrm{T}$, the mercury magnetometer measured $(13.20 \pm 0.03)\,\mathrm{pT}$, while the SQUID saw $(13.8 \pm 0.7)\,\mathrm{pT}$. This corresponds to a shielding factor of 1.23 ± 0.01 million. There is a huge difference between the shielding factors in z- and in y-direction because in the side walls of the magnetic shields that are perpendicular to the y-direction, there is the door and huge access holes that can be used to guide UCNs and high voltage cables into the shielded room.

Part 4

SUMMARY

4.1

SUMMARY

Mercury is a powerful probe to measure magnetic fields and to examine fundamental interactions with spins. For future precession experiments using ^{199}Hg, it is essential to investigate the interaction of ^{199}Hg with electric and magnetic fields from constant fields to near resonant light, and to improve the accuracy of measurements of the atomic spectrum further. Theoretical models for these interactions and properties of the mercury spectrum were given in chapter 1.3.

In this thesis, the development of a magnetometry setup is presented that is optimized to operate a mercury co-magnetometer in an nEDM experiment, but can also be used for pure mercury magnetometry. In a spatially appropriately homogeneous magnetic holding field, the systematic uncertainty of a magnetic field measurement with this system would be dominated by the uncertainties of previously published spectroscopic properties of mercury.

Spectroscopy

A Doppler-free spectroscopy setup was built that is capable of resolving the spectroscopic properties that are relevant for laser-based mercury precession experiments with a higher accuracy than previously published results.

During the experiments, a degenerating effect of some mercury vapor cells, that had also been reported by previous experiments using resonant light, was observed and spectroscopy was used to show that this effect is likely caused by photo-chemical reactions of excited mercury atoms.

Spectroscopic techniques that can resolve the mercury transitions without Doppler broadening were discussed and the shape and structure of the Doppler-free spectra that were recorded of all naturally abundant mercury isotopes was explained based on the quantum numbers of the transitions.

The spectroscopy setup was used to reduce the uncertainty of the differential isotope shift between the $^1S_0 \rightarrow {}^3P_1$ transition in ^{199}Hg and ^{204}Hg by about two orders of magnitude. In this measurement, the shift between these two transitions was compared to their Zeeman splitting (see section 2.5.2). As an accurate knowledge of the relative isotope shift between ^{199}Hg and ^{204}Hg is crucial for a bias-free operation of the mercury magnetometer, an experiment to verify these results with a different approach was proposed.

A proof of principle experiment measuring the scalar and tensor component of the DC Stark shift in mercury was shown in section 2.5.3. To compare the spectra with and without an electric field without being sensitive to fluctuations of the laser frequency, two Doppler-free spectroscopy setups were used in parallel, sharing the same laser source. This was the first measurement of the DC stark shift in mercury with Doppler-free signals. As no elaborate effort was expended to determine the exact value

of the electric field strength inside the spectroscopy cell, the scalar and tensor stark shift constants resulting from this experiment were not more accurate than previously published results. However, with a careful electric field design, this measurement procedure can be used to measure the DC Stark shift with a higher accuracy.

(Co-)Magnetometry

A laser based mercury magnetometer system was developed and used to measure the small magnetic field in a magnetic shield to determine the shielding factor (see section 3.5). Uncertainties and systematic shifts in mercury magnetometry and co-magnetometry in nEDM experiments were discussed.

The current smallest uncertainty in experiments searching for the nEDM, $1.82 \times 10^{-26}\ e\,\mathrm{cm}$, was achieved using a mercury co-magnetometer. Next generation nEDM experiments aim to set upper limits in the order of $1 \times 10^{-28}\ e\,\mathrm{cm}$. Besides increasing the UCN density and polarization lifetime, magnetometry is critical for the accuracy of nEDM experiments. Systematic effects in mercury magnetometry can limit the accuracy or even lead to a false result. A mercury (co-)magnetometry system (see chapter 3.1) was developed and the components were optimized for the more challenging operation as a co-magnetometer. The magnetometer readout, presented in section 3.4.2, was optimized to detect a weak, modulated, laser beam on a large active area to reduce power noise that is caused by mechanical vibrations. While the power stabilization setup, presented in section 3.4.3, reduces power fluctuations of the laser, the frequency of the laser light is set and stabilized with a Doppler-free spectroscopy setup, shown in section 3.4.1. Different spectroscopic techniques were developed and optimized to create an error signal for the self-calibrating frequency lock.

Systematic effects that limit this system were discussed. The literature value for the differential isotope shift between ^{199}Hg and ^{204}Hg, which is used in the calibration of the frequency lock, was the dominant systematic uncertainty in the magnetic field measurement of

$$\delta B^{(1)}_{\mathrm{dVLS}} = 3.9 \times 10^{-16}\,\mathrm{T}$$

leading to a (mainly, see section 3.3.4.4) statistical uncertainty of

$$\delta d_{\mathrm{dVLS}} = 1.4 \times 10^{-27}\ e\,\mathrm{cm}$$

when mercury is used for magnetometry in an nEDM measurement. A new systematic effect that has not been described in literature yet, arising from the combination of the light shift effect and geometric phases, was found and described. With the systematic uncertainty of the frequency calibration mentioned above, the light-shift geometric-phase effect causes a systematic uncertainty of

$$\delta d_{\mathrm{LSGP}} = 2.7 \times 10^{-29}\ e\,\mathrm{cm}.$$

The differential isotope shift between ^{199}Hg and ^{204}Hg was measured using the Zeeman effect for calibration (see section 2.5.2) with a higher accuracy, reducing the corresponding d_{dVLS} and δd_{LSGP} to insignificance.

More systematic effects in mercury co-magnetometry that have not been mentioned in previous works arise from a combination of a frequency shift caused by the DC Stark effect in constant electric fields and the vector light shift effect leading to a (mainly, see section 3.3.4.1) statistical uncertainty of

$$\delta d^{(1)}_{n,\mathrm{dVLS}} = 1.2 \times 10^{-27}\, e\,\mathrm{cm}$$

in a typical nEDM experiment if it is not considered and a Stark-shift induced light-shift geometric-phase effect of

$$\delta d_{n,\mathrm{SiLSGP}} = 2.2 \times 10^{-29}\, e\,\mathrm{cm}$$

which scales anti symmetric with the electric field ($\propto E^3$) and can thus cause a systematic shift of the result. It was shown that spectroscopy in high electric fields is possible and that the Stark shift can be accounted for in the frequency lock of the laser system.

The remaining uncertainty is dominated by the accuracy of the spectroscopy to set the laser to the NLP causing the statistical uncertainty

$$\delta d^{(1)}_{\mathrm{dVLS}} = 2.7 \times 10^{-28}\, e\,\mathrm{cm}$$

when used in a co-magnetometer in an nEDM experiment, and

$$\delta B^{(1)}_{\mathrm{dVLS}} = 7.4 \times 10^{-17}\,\mathrm{T}$$

in pure mercury magnetometry (see section 3.3.4.5). Paths to improve the uncertainties in the frequency lock of the laser further were shown in section 3.4.1.1 and section 3.4.1.2. If necessary, future experiments can furthermore reduce all light shift related effects by reducing the readout power. Introducing a mechanism to enhance the precision of aligning the laser beam with respect to the magnetic field reduces all light-shift effects but the light-shift induced geometric-phase effect. Improving the alignment of the laser beam to the magnetic holding field to be perpendicular within ±1 mrad reduces these uncertainties by a factor of ~ 2.5.

The size of the geometric phases, and thus whether a co-magnetometer or a pure mercury vapor magnetometer is favorable in an nEDM experiment, depends on the shape and homogeneity of the magnetic field in the UCN precession chambers in this particular experiment. With the magnetometry system presented in this thesis, the light-shift related uncertainties are small enough to measure the nEDM with an uncertainty smaller than $1 \times 10^{-28}\, e$ cm, regardless, whether mercury is used in a co-magnetometer or in pure mercury magnetometers above and below the UCN chambers.

Part 5

APPENDIX

A

LONGITUDINAL DE-POLARIZATION

When an atom travels through the precession chamber in a straight line l_i between two collisions where the spin can not follow the magnetic field lines adiabatically, the spin gathers an angle $\theta_i = \frac{\Delta B_{T,i}}{B_0} \cdot l_i$ to the magnetic field. Here, B_0 is the holding field, and $\Delta B_{T,i}$ is the change in the transverse component during the free flight of the atom. The polarization of the atom changes by $\Delta P_i = 1 - cos\theta_i \approx \frac{\theta_i^2}{2}$. The depolarization rate $\frac{1}{T_{1,i}}$ is the change in polarization divided by the time τ_i the atom needed to travel along l_i:

$$\frac{1}{T_{1,i}} \approx \frac{\theta_i^2}{2\tau_i} = \frac{\Delta B_{T,i}^2}{B_0^2} \cdot \frac{l_i^2}{4\tau_i} = \frac{\Delta B_{T,i}^2}{B_0^2} \cdot \frac{l_i \cdot v_i}{4} \tag{A.1}$$

Here, v_i is the velocity of the atom. The average depolarization rate is then given by

$$\frac{1}{T_1} = \left\langle \frac{1}{T_{1,i}} \right\rangle. \tag{A.2}$$

For a rough estimate of the depolarization rate $\frac{1}{T_1}$ can be achieved by using average values with average velocity v_{th}, the average free path length in the vapor cell $\bar{l}$ and the average change of the transverse field component during the free paths $\langle \Delta B_T \rangle$:

$$\frac{1}{T_1} = \frac{\langle \Delta B_T \rangle^2}{B_0^2} \cdot \frac{\bar{l} \cdot v_{\text{th}}}{4} \tag{A.3}$$

B

READOUT

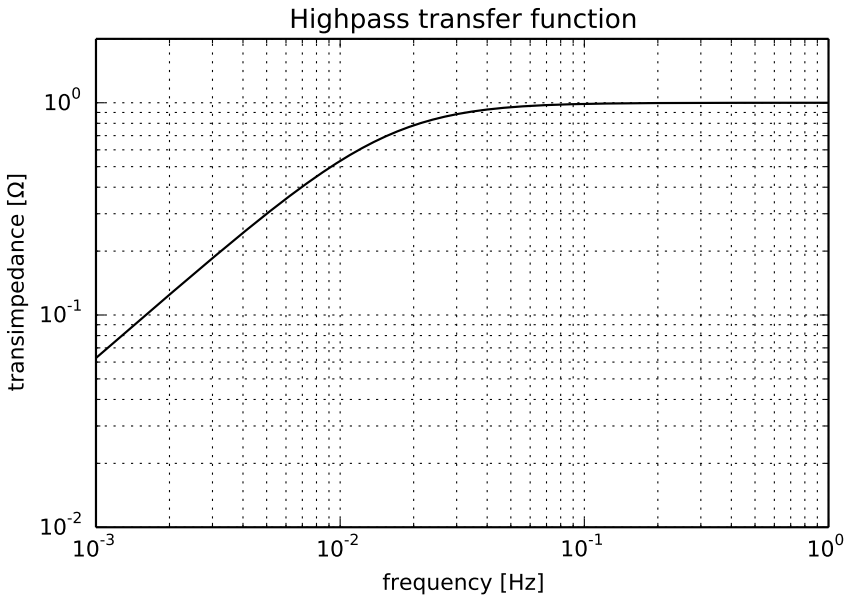

Figure B.1: Transfer function of the high pass filter. To get rid of the DC component of the readout signal, a high pass filter with a small corner frequency was implemented. Taken from [96].

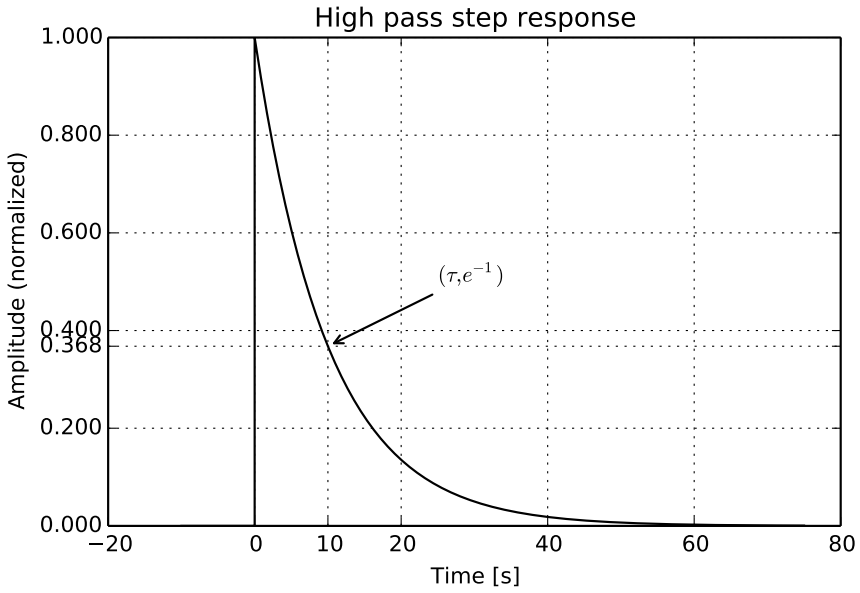

Figure B.2: Step response of the high pass filter. Due to the low corner frequency, the filter has a slow response to large steps of the signal. This can be relevant when the strong polarizing beam partially hits the photodiode. The average over one period in the free precession decay signal then follows the step response curve. To avoid this, the polarizing beam should be adjusted appropriately. If it can not be avoided completely, the step response curve should be considered in the fit. Taken form [96].

Figure B.3: Rendering of the readout setup. The readout electronics are inside a massive light-tight aluminum shield.

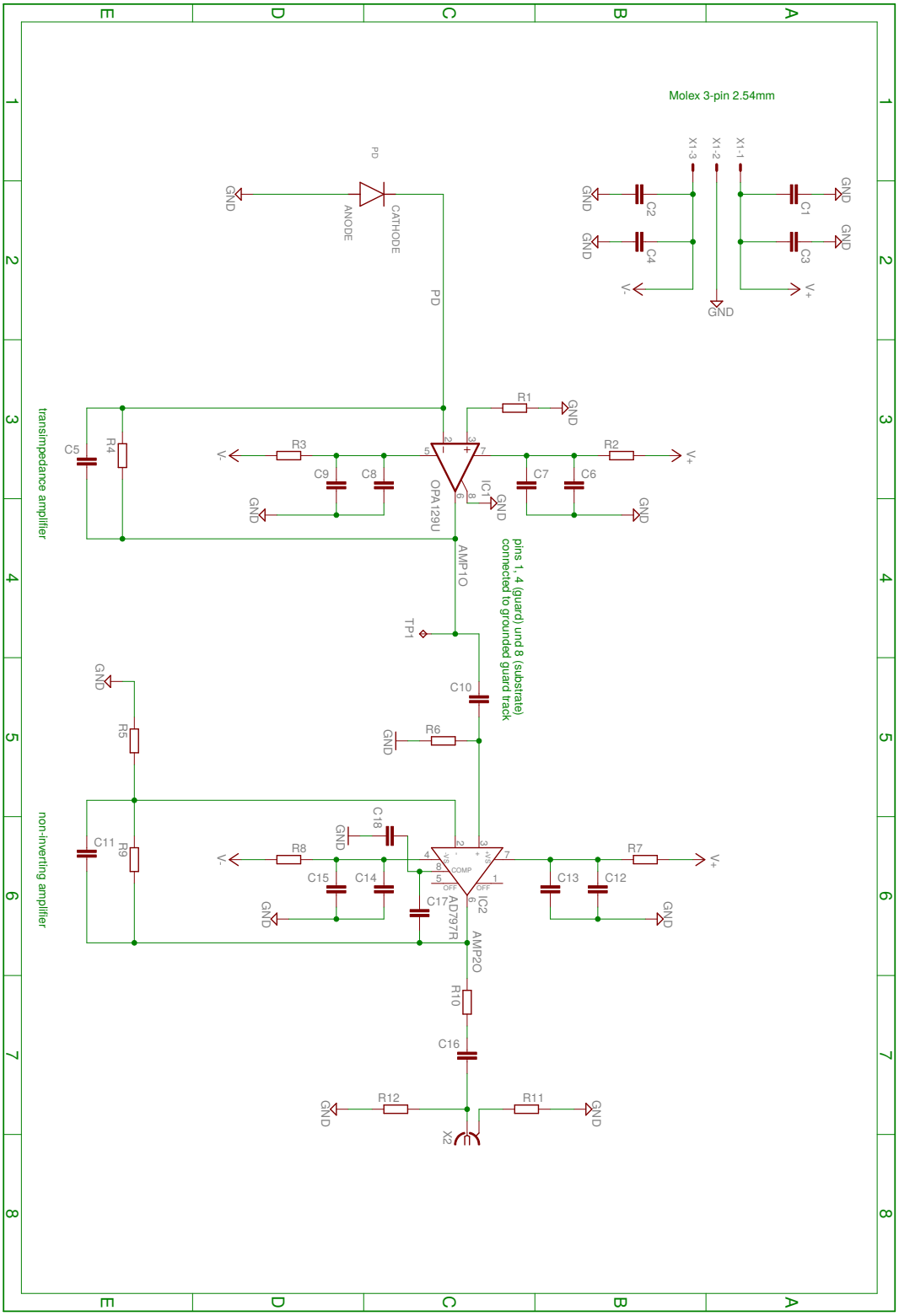

Figure B.4: Layout of the photodiode amplification board. Taken from [96].

C

POWERLOCK READOUT

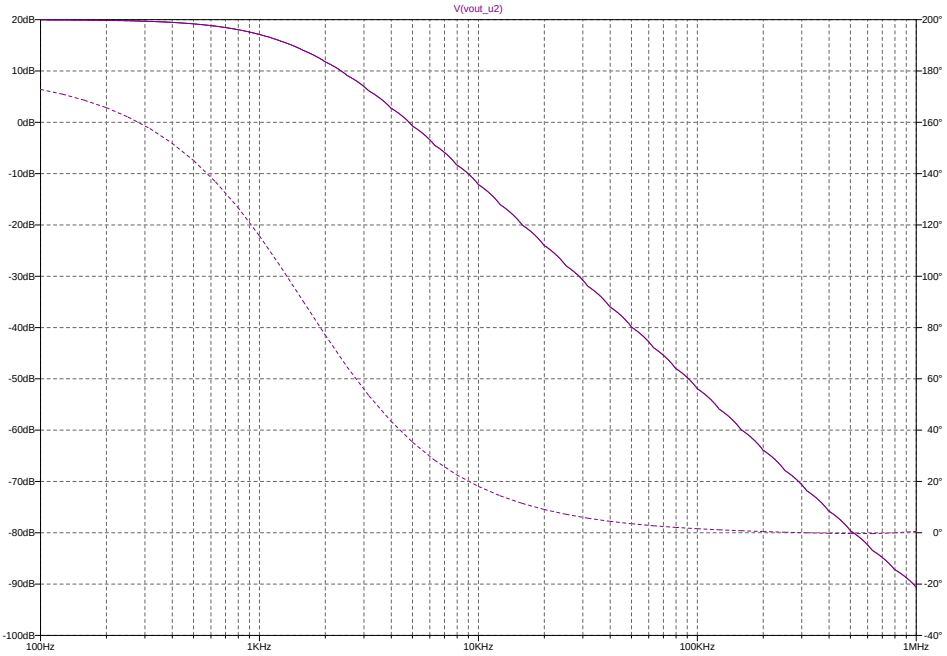

Figure C.1: Frequency response of the photodiode preamplifier board for the power lock.

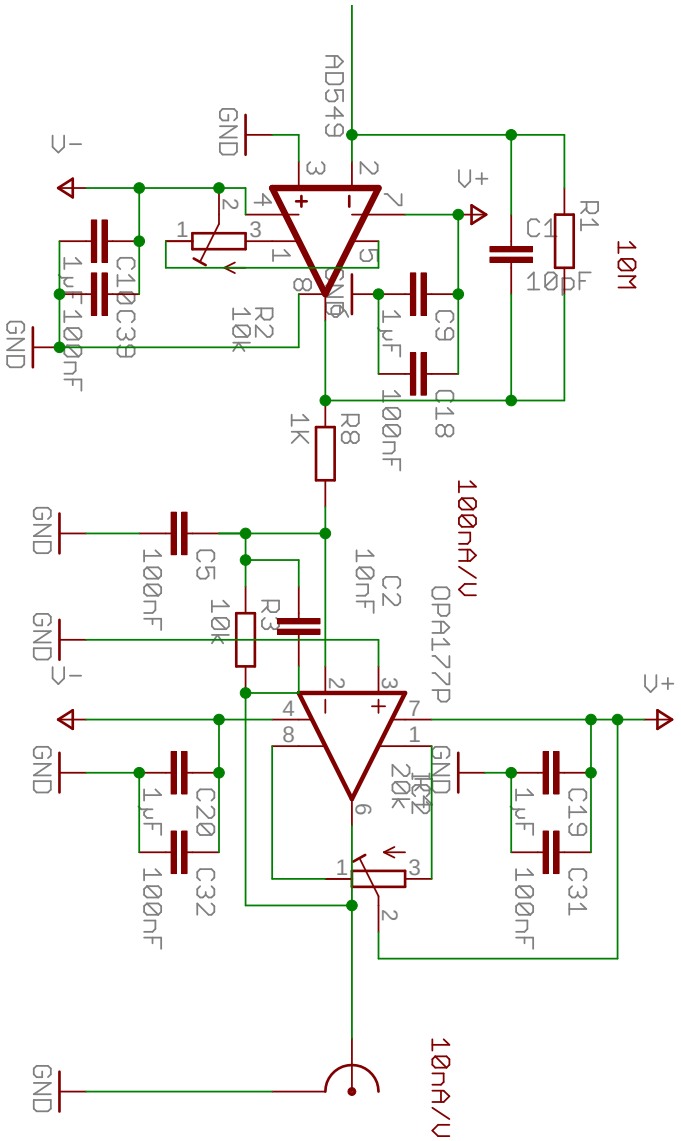

Figure C.2: Schematic of the photodiode preamplifier board for the power lock. The total transimpedance is 100 MΩ

BIBLIOGRAPHY

[1] V. C. Rubin and W. K. Ford Jr. “Rotation of the andromeda nebula from a spectroscopic survey of emission regions.” In: *The Astrophysical Journal* 159 (1970), p. 379.

[2] A. G. Riess, A. V. Filippenko, P. Challis, A. Clocchiatti, A. Diercks, P. M. Garnavich, R. L.. Gilliland, C. J. Hogan, S. Jha, R. P. Kirshner, et al. “Observational evidence from supernovae for an accelerating universe and a cosmological constant.” In: *The Astronomical Journal* 116.3 (1998), p. 1009.

[3] P. Huet and E. Sather. “Electroweak baryogenesis and standard model CP violation.” In: *Phys. Rev. D* 51 (1995), pp. 379–394.

[4] V. A. Kostelecky. *CPT and Lorentz Tests in the Standard Model*. Tech. rep. hep-ph/9810274. IUHET-387. Bloomington, IN: Indiana Univ. Dept. Phys., 1998.

[5] P. W. Higgs. “Broken Symmetries and the Masses of Gauge Bosons.” In: *Phys. Rev. Lett.* 13 (16 1964), pp. 508–509.

[6] F. Englert and R. Brout. “Broken symmetry and the mass of gauge vector mesons.” In: *Physical Review Letters* 13.9 (1964), p. 321.

[7] S. Chatrchyan et al. “Observation of a new boson at a mass of 125 GeV with the CMS experiment at the LHC.” In: *Physics Letters B* 716.1 (2012), pp. 30 –61.

[8] G. Aad et al. “Observation of a new particle in the search for the Standard Model Higgs boson with the ATLAS detector at the LHC.” In: *Physics Letters B* 716.1 (2012), pp. 1 –29.

[9] D. Budker and M. Romalis. “Optical magnetometry.” In: *Nature Physics 3, 227 - 234* (2007).

[10] R. Golub and J. M. Pendlebury. “Ultra-cold neutrons.” In: *Reports on Progress in Physics* 42.3 (1979), p. 439.

[11] W. G. Wadey. “Magnetic shielding with multiple cylindrical shells.” In: *Review of Scientific Instruments* 27.11 (1956), pp. 910–916.

[12] S. A. Murthy, D. Krause, Z. L. Li, and L. R. Hunter. “New limits on the electron electric dipole moment from cesium.” In: *Phys. Rev. Lett.* 63 (9 1989), pp. 965–968.

[13] C. J. Berglund, L. R. Hunter, D. Krause Jr., E. O. Prigge, M. S. Ronfeldt, and S. K. Lamoreaux. “New Limits on Local Lorentz Invariance from Hg and Cs Magnetometers.” In: *Phys. Rev. Lett.* 75 (10 1995), pp. 1879–1882.

[14] A. N. Youdin, D. Krause Jr, K. Jagannathan, L. R. Hunter, and S. K. Lamoreaux. “Limits on spin-mass couplings within the axion window.” In: *Physical review letters* 77.11 (1996), p. 2170.

[15] B. Graner, Y. Chen, E. G. Lindahl, and B. R. Heckel. "Reduced Limit on the Permanent Electric Dipole Moment of ^{199}Hg." In: *Phys. Rev. Lett.* 116 (16 2016), p. 161601.

[16] D. Bear, R. E. Stoner, R. L. Walsworth, V. Alan Kostelecky, and Charles D. Lane. "Limit on Lorentz and CPT Violation of the Neutron Using a Two-Species Noble-Gas Maser." In: *Phys. Rev. Lett.* 85 (24 2000), pp. 5038–5041.

[17] S. Afach et al. "Constraining interactions mediated by axion-like particles with ultracold neutrons." In: *Physics Letters B* 745 (2015), pp. 58 –63.

[18] I. Altarev et al. "Test of Lorentz Invariance with Spin Precession of Ultracold Neutrons." In: *Phys. Rev. Lett.* 103 (8 2009), p. 081602.

[19] M. Pospelov and A. Ritz. "Electric dipole moments as probes of new physics." In: *Annals of Physics* 318.1 (2005). Special Issue, pp. 119 –169.

[20] N. F. Ramsey. "A Molecular Beam Resonance Method with Separated Oscillating Fields." In: *Phys. Rev.* 78 (6 1950), pp. 695–699.

[21] C. A. Baker et al. "Apparatus for measurement of the electric dipole moment of the neutron using a cohabiting atomic-mercury magnetometer." In: *Nuclear Instruments and Methods in Physics Research Section A: Accelerators, Spectrometers, Detectors and Associated Equipment* 736 (2014), pp. 184 –203.

[22] Khriplovich. *CP Violation Without Strangeness*. Springer, 1965.

[23] J. Engel, M. J. Ramsey-Musolf, and U. Van Kolck. "Electric dipole moments of nucleons, nuclei, and atoms: The Standard Model and beyond." In: *Progress in Particle and Nuclear Physics* 71 (2013), pp. 21–74.

[24] J. M. Pendlebury, S. Afach, N. J. Ayres, C. A. Baker, G. Ban, Georg Bison, Kazimierz Bodek, M. Burghoff, P. Geltenbort, K. Green, et al. "Revised experimental upper limit on the electric dipole moment of the neutron." In: *Physical Review D* 92.9 (2015), p. 092003.

[25] C. F. Gauß. "Anzeige der Abhandlung des Herrn Hofr. Gauß: Intensitas vis magneticae terrestris admensuram absolutam revocata." In: *Astronomische Nachrichten* 10 (Feb. 1833), p. 349.

[26] P. W. Anderson and J. M. Rowell. "Probable Observation of the Josephson Superconducting Tunneling Effect." In: *Phys. Rev. Lett.* 10 (6 1963), pp. 230–232.

[27] R. C. Jaklevic, J. Lambe, A. H. Silver, and J. E. Mercereau. "Quantum Interference Effects in Josephson Tunneling." In: *Phys. Rev. Lett.* 12 (7 1964), pp. 159–160.

[28] M. Hämäläinen, R. Hari, R. J. Ilmoniemi, J. Knuutila, and O. V. Lounasmaa. "Magnetoencephalography—theory, instrumentation, and applications to noninvasive studies of the working human brain." In: *Rev. Mod. Phys.* 65 (2 1993), pp. 413–497.

[29] J. M. Taylor, P. Cappellaro, L. Childress, L. Jiang, D. Budker, P. R. Hemmer, R. Yacoby, R. Walsworth, and D. S. Lukin. "High-sensitivity diamond magnetometer with nanoscale resolution." In: *Nature Physics* 4.10 (2008), pp. 810–816.

[30] K. Jensen, N. Leefer, A. Jarmola, Y. Dumeige, V. M. Acosta, P. Kehayias, B. Patton, and D. Budker. "Cavity-enhanced room-temperature magnetometry using absorption by nitrogen-vacancy centers in diamond." In: *Physical review letters* 112.16 (2014), p. 160802.

[31] A. Kastler. "Some suggestions concerning the production and detection by optical means of inequalities in the populations of levels of spatial quantization in atoms. Application to the Stern and Gerlach and magnetic resonance experiments." In: *J. Phys. Radium* 11.11 (1950).

[32] H. G. Dehmelt. "Modulation of a Light Beam by Precessing Absorbing Atoms." In: *Phys. Rev.* 105 (6 1957), pp. 1924–1925.

[33] W. E. Bell and A. L. Bloom. "Optical detection of magnetic resonance in alkali metal vapor." In: *Physical Review* 107.6 (1957), p. 1559.

[34] S. Groeger, G. Bison, J.-L. Schenker, R. Wynands, and A. Weis. "A high-sensitivity laser-pumped Mx magnetometer." In: *The European Physical Journal D - Atomic, Molecular, Optical and Plasma Physics* 38.2 (2006), pp. 239–247.

[35] H. B. Dang, A. C. Maloof, and M. V. Romalis. "Ultrahigh sensitivity magnetic field and magnetization measurements with an atomic magnetometer." In: *Applied Physics Letters* 97.15 (2010), p. 151110.

[36] W. Heil, C. Gemmel, S. Karpuk, Y. Sobolev, K. Tullney, F. Allmendinger, U. Schmidt, M. Burghoff, W. Kilian, S. Knappe-Grüneberg, et al. "Spin clocks: Probing fundamental symmetries in nature." In: *Annalen der Physik* 525.8-9 (2013), pp. 539–549.

[37] S. Appelt, A. Ben-Amar Baranga, C. J. Erickson, M. V. Romalis, A. R. Young, and W. Happer. "Theory of spin-exchange optical pumping of ^{3}He and ^{129}Xe." In: *Phys. Rev. A* 58 (2 1998), pp. 1412–1439.

[38] Skyler M. Degenkolb. "Optical Magnetometry Using Multiphoton Transitions." PhD thesis. University of Michigan, 2016.

[39] S. J. Seltzer and M. V. Romalis. "Unshielded three-axis vector operation of a spin-exchange-relaxation-free atomic magnetometer." In: *Applied physics letters* 85.20 (2004), pp. 4804–4806.

[40] B. Patton, E. Zhivun, D. C. Hovde, and D. Budker. "All-Optical Vector Atomic Magnetometer." In: *Phys. Rev. Lett.* 113 (1 2014), p. 013001.

[41] M. L. Huber, A. Laesecke, and D. G. Friend. "The vapor pressure of mercury." In: *National Institute of Standards and Technology, NISTIR* 6643 (2006).

[42] J. Franck and G. Hertz. "Über Zusammenstöße zwischen Elektronen und den Molekülen des Quecksilberdampfes und die Ionisierungsspannung desselben." In: *Physikalische Blätter* 23.7 (1967), pp. 294–301.

[43] Michael Petersen. "Laser-cooling of neutral mercury and laser-spectroscopy of the 1So-3 Po optical clock transition." PhD thesis. L'OBSERVATOIRE DE PARIS, 2009.

[44] H. Hachisu, K. Miyagishi, S. G. Porsev, A. Derevianko, V. D. Ovsiannikov, V. G. Pal'chikov, M. Takamoto, and H. Katori. "Trapping of Neutral Mercury Atoms and Prospects for Optical Lattice Clocks." In: *Phys. Rev. Lett.* 100 (5 2008), p. 053001.

[45] M. V. Romalis, W. C. Griffith, J. P. Jacobs, and E. N. Fortson. "New Limit on the Permanent Electric Dipole Moment of ^{199}Hg." In: *Phys. Rev. Lett.* 86 (12 2001), pp. 2505–2508.

[46] P. G. Harris et al. "New Experimental Limit on the Electric Dipole Moment of the Neutron." In: *Phys. Rev. Lett.* 82 (5 1999), pp. 904–907.

[47] J. E. Sansonetti, W. C. Martin, and S. L. Young. "Handbook of basic atomic spectroscopic data." In: *Carbon* 100 (2005), p. 1634.

[48] P. S. Doidge. "A compendium and critical review of neutral atom resonance line oscillator strengths for atomic absorption analysis." In: *Spectrochimica Acta Part B: Atomic Spectroscopy* 50.3 (1995), pp. 209 –263.

[49] W. Happer and B. S. Mathur. "Effective Operator Formalism in Optical Pumping." In: *Phys. Rev.* 163 (1 1967), pp. 12–25.

[50] C. Cohen-Tannoudji and J. Dupont-Roc. "Experimental study of Zeeman light shifts in weak magnetic fields." In: *Physical Review A* 5.2 (1972), p. 968.

[51] D. C. Morton. "Atomic Data for Resonance Absorption Lines. II. Wavelengths Longward of the Lyman Limit for Heavy Elements." In: *The Astrophysical Journal Supplement Series* 130.2 (2000), p. 403.

[52] D. Budker and D. F. Jackson Kimball. *Optical magnetometry*. Cambridge University Press, 2013.

[53] S. Afach et al. "A measurement of the neutron to 199Hg magnetic moment ratio." In: *Physics Letters B* 739 (2014), pp. 128 –132.

[54] J. N. Dodd. "The g J Value of the 6 3 P 1 Level in Mercury." In: *Proceedings of the Physical Society* 78.1 (1961), p. 65.

[55] L. R. Hunter, D. Krause Jr, S. Murthy, and T. W. Sung. "Precision measurement of the Stark shift of the cesium D lines." In: *Physical Review A* 37.9 (1988), p. 3283.

[56] D. M. Harber and M. V. Romalis. "Measurement of the scalar Stark shift of the $6^1S_0 \rightarrow 6^3P_1$ transition in Hg." In: *Phys. Rev. A* 63 (1 2000), p. 013402.

[57] R. D. Kaul and William S. Latshaw. "Stark Shift in the 6s6p 3 P 1 State of Mercury." In: *JOSA* 62.5 (1972), pp. 615–618.

[58] R. Jackiw and C. Rebbi. "Vacuum Periodicity in a Yang-Mills Quantum Theory." In: *Phys. Rev. Lett.* 37 (3 1976), pp. 172–175.

[59] J. H. Christenson, J. W. Cronin, V. L. Fitch, and R. Turlay. "Evidence for the 2π Decay of the K_2^0 Meson." In: *Phys. Rev. Lett.* 13 (4 1964), pp. 138–140.

[60] Tatsuya Nakada. "Review on CP violation." In: *AIP Conference Proceedings*. Vol. 302. 1. AIP. 1994, pp. 425–463.

[61] R. H. Cyburt, B. D. Fields, and K. A. Olive. "Primordial nucleosynthesis in light of WMAP." In: *Physics Letters B* 567.3 (2003), pp. 227 –234.

[62] A. D. Sakharov. “Violation of CP invariance, C asymmetry, and baryon asymmetry of the universe.” In: *Soviet Physics Uspekhi* 34.5 (1991), p. 392.

[63] T.E. Chupp, P. Fierlinger, M. J. Ramsey-Musolf, and J.T. Singh. “Electric Dipole Moments of the Atoms, Molecules, Nuclei and Particles.” To be published. 2017.

[64] V. Anastassopoulos et al. “A storage ring experiment to detect a proton electric dipole moment.” In: *Review of Scientific Instruments* 87.11 (2016), p. 115116.

[65] A. Steyerl et al. “A new source of cold and ultracold neutrons.” In: *Physics Letters A* 116.7 (1986), pp. 347 –352.

[66] F. M. Piegsa, M. Fertl, S. N. Ivanov, M. Kreuz, K. K. H. Leung, P. Schmidt-Wellenburg, T. Soldner, and O. Zimmer. “New source for ultracold neutrons at the Institut Laue-Langevin.” In: *Phys. Rev. C* 90 (1 2014), p. 015501.

[67] A. Frei, Yu Sobolev, I. Altarev, K. Eberhardt, A. Gschrey, E. Gutsmiedl, R. Hackl, G. Hampel, F. J. Hartmann, W. Heil, et al. “First production of ultracold neutrons with a solid deuterium source at the pulsed reactor TRIGA Mainz.” In: *The European Physical Journal A* 34.2 (2007), pp. 119–127.

[68] L. I. Schiff. “Measurability of nuclear electric dipole moments.” In: *Physical Review* 132.5 (1963), p. 2194.

[69] J. Baron et al. “Order of Magnitude Smaller Limit on the Electric Dipole Moment of the Electron.” In: *Science* 343.6168 (2014), pp. 269–272.

[70] Matthew Swallows. “A search for the permanent electric dipole moment of mercury-199.” PhD thesis. University of Washington, 2007.

[71] I. S. Altarev et al. “New measurement of the electric dipole moment of the neutron.” In: *Physics Letters B* 276.1 (1992), pp. 242 –246.

[72] Tobias Lins. “High Precision Physics in Low Magnetic Fields: Implementation of a Sub-Nanotesla Field with Femtotesla Temporal Stability.” PhD thesis. Technische Universität München, 2016.

[73] M. V. Romalis and G. D. Cates. “Accurate ^{3}He polarimetry using the Rb Zeeman frequency shift due to the Rb—^{3}He spin-exchange collisions.” In: *Phys. Rev. A* 58 (4 1998), pp. 3004–3011.

[74] Z. Chowdhuri, M. Fertl, M. Horras, K. Kirch, J. Krempel, B. Lauss, A. Mtchedlishvili, D. Rebreyend, S. Roccia, P. Schmidt-Wellenburg, et al. “Experimental study of 199Hg spin anti-relaxation coatings.” In: *Applied Physics B* 115.2 (2014), pp. 257–262.

[75] Martin Christoph Fertl. “A laser based mercury co-magnetometer for the neutron electric dipole moment search.” PhD thesis. ETH ZÜRICH, 2014.

[76] C. R. Webster and R. N. Zare. “Photochemical Isotope Separation of Hg-196 by Reaction with Hydrogen Halides.” In: *J. Phys. Chem* 85 (1981), pp. 1302–1305.

[77] G. Müller, D. Hessel, H. Schmidt, W. Häussler, and U. Offermanns. “Quellenprofile und filterung bei der photochemischen quecksilber-isotopentrennung.” In: *Journal of Photochemistry* 13.2 (1980), pp. 109–121.

[78] Yu V. Vyazovetskii and A. P. Senchenkov. “Production of highly enriched mercury isotopes by a photochemical method.” In: *Technical Physics* 43.1 (1998), pp. 60–66.

[79] N. R. Stankov. “Application of mercury isotopes and their production.” In: *Journal of radioanalytical and nuclear chemistry* 205.2 (1996), pp. 175–179.

[80] W. G. Schweitzer. “Hyperfine structure and isotope shifts in the 2537-Å line of mercury by a new interferometric method.” In: *JOSA* 53.9 (1963), pp. 1055–1072.

[81] C. Wieman and Th. W. Hänsch. “Doppler-free laser polarization spectroscopy.” In: *Physical Review Letters* 36.20 (1976), p. 1170.

[82] W. Demtröder. *Laserspektroskopie: Grundlagen und Techniken*. Springer-Verlag, 2007.

[83] F. Köhler, K. Blaum, M. Block, S. Chenmarev, S. Eliseev, D. A. Glazov, M. Goncharov, J. Hou, A. Kracke, D. A. Nesterenko, et al. “Isotope dependence of the Zeeman effect in lithium-like calcium.” In: *Nature communications* 7 (2016).

[84] Thorsten Sven Zechlau. “Ultra-Cold Neutron Transport and Spin Manipulation System for the Measurement of the Neutron Electric Dipole Moment.” Dissertation. München: Technische Universität München, 2016.

[85] X. Fu, K. Liu, R. Zhao, W. Gou, J. Sun, Z. Xu, and Y. Wang. “Polarization spectroscopy of the 1 S 0-3 P 1 transition of mercury isotopes at 253.7 nm.” In: *Chinese Optics Letters* 13.7 (2015), p. 073001.

[86] K. F. Smith et al. “A search for the electric dipole moment of the neutron.” In: *Physics Letters B* 234.1 (1990), pp. 191 –196.

[87] K. Green, P. G. Harris, P. Iaydjiev, D. J. R. May, J. M. Pendlebury, K. F. Smith, M. Van der Grinten, P. Geltenbort, and S. Ivanov. “Performance of an atomic mercury magnetometer in the neutron EDM experiment.” In: *Nuclear Instruments and Methods in Physics Research Section A: Accelerators, Spectrometers, Detectors and Associated Equipment* 404.2 (1998), pp. 381–393.

[88] J. M. Pendlebury, W. Heil, Y. Sobolev, P. G. Harris, J. D. Richardson, R. J. Baskin, D. D. Doyle, P. Geltenbort, K. Green, M. G. D. Van Der Grinten, et al. “Geometric-phase-induced false electric dipole moment signals for particles in traps.” In: *Physical Review A* 70.3 (2004), p. 032102.

[89] C. A. Baker, D. D. Doyle, P. Geltenbort, K. Green, M. G. D. Van der Grinten, P. G. Harris, P. Iaydjiev, S. N. Ivanov, D. J. R. May, J. M. Pendlebury, et al. “Improved experimental limit on the electric dipole moment of the neutron.” In: *Physical Review Letters* 97.13 (2006), p. 131801.

[90] J. P. Jacobs, W. M. Klipstein, S. K. Lamoreaux, B. R. Heckel, and E. N. Fortson. “Limit on the electric-dipole moment of ^{199}Hg using synchronous optical pumping.” In: *Phys. Rev. A* 52 (5 1995), pp. 3521–3540.

[91] G. Pignol and S. Roccia. “Electric-dipole-moment searches: Reexamination of frequency shifts for particles in traps.” In: *Physical Review A* 85.4 (2012), p. 042105.

[92] M. V. Romalis and L. Lin. “Surface nuclear spin relaxation of 199Hg.” In: *The Journal of Chemical Physics* 120.3 (2004), pp. 1511–1515.

[93] Marlon Horras. “A highly sensitive 199Hg magnetometer for the nEDM experiment.” PhD thesis. ETH Zürich, 2012.

[94] G. D. Cates, S. R. Schaefer, and W. Happer. “Relaxation of spins due to field inhomogeneities in gaseous samples at low magnetic fields and low pressures.” In: *Phys. Rev. A* 37 (8 1988), pp. 2877–2885.

[95] M. J. Bales, P. Fierlinger, and R. Golub. “Non-extensive statistics in spin precession.” In: *EPL (Europhysics Letters)* 116.4 (2017), p. 43002.

[96] Roman Thiele. “Implementation and characterization of a mercury magnetometer.” MA thesis. TUM, 2014.

[97] Johannes Weber. “Optisches Pumpen von 199 Hg -Atomen mit einem UV-Laser (Optical pumping of 199 Hg atoms with a UV laser).” MA thesis. Technische Universität München, 2012.

[98] Thomas Stolz. “Reducing Light Shifts in Optical Mercury-Magnetometry by Frequency Stabilizing a 254 nm Laser with Doppler-Free Saturation Spectroscopy.” MA thesis. TUM, 2014.

[99] M. D. Swallows, T. H. Loftus, W. C. Griffith, B. R. Heckel, E. N. Fortson, and M. V. Romalis. “Techniques used to search for a permanent electric dipole moment of the 199 Hg atom and the implications for CP violation.” In: *Physical Review A* 87.1 (2013), p. 012102.

[100] S. K. Lamoreaux and R. Golub. “Detailed discussion of a linear electric field frequency shift induced in confined gases by a magnetic field gradient: Implications for neutron electric-dipole-moment experiments.” In: *Phys. Rev. A* 71 (3 2005), p. 032104.

[101] S. Afach, C. A. Baker, G. Ban, G. Bison, K. Bodek, Z. Chowdhuri, M. Daum, M. Fertl, B. Franke, P. Geltenbort, et al. “Measurement of a false electric dipole moment signal from 199Hg atoms exposed to an inhomogeneous magnetic field.” In: *The European Physical Journal D* 69.10 (2015), p. 225.

[102] J. P. Jacobs and R. B. Warrington. “Pressure shift and broadening of the 254-nm intercombination line of mercury by N 2.” In: *Physical Review A* 68.3 (2003), p. 032722.

[103] David Wurm. *Private communication.*

[104] T. Petelski, M. Fattori, G. Lamporesi, J. Stuhler, and G. M. Tino. “Doppler-free spectroscopy using magnetically induced dichroism of atomic vapor: a new scheme for laser frequency locking.” In: *The European Physical Journal D - Atomic, Molecular, Optical and Plasma Physics* 22.2 (2003), pp. 279–283.

[105] H. Liu, S. Yin, J. Qian, Z. Xu, and Y. Wang. “Optimization of Doppler-free magnetically induced dichroic locking spectroscopy on the 1 S 0 – 3 P 1 transition of a neutral mercury atom.” In: *Journal of Physics B: Atomic, Molecular and Optical Physics* 46.8 (2013), p. 085005.

[106] I. Altarev et al. “A large-scale magnetic shield with 10^6 damping at millihertz frequencies.” In: *Journal of Applied Physics* 117.18 (2015), p. 183903.

[107] Stefan Stuiber. “in preparation.” PhD thesis. Technische Universtät München.

[108] I. Altarev, E. Babcock, D. Beck, M. Burghoff, S. Chesnevskaya, T. Chupp, S. Degenkolb, I. Fan, P. Fierlinger, A. Frei, et al. “A magnetically shielded room with ultra low residual field and gradient.” In: *Review of scientific instruments* 85.7 (2014), p. 075106.

[109] I. Altarev et al. “Minimizing magnetic fields for precision experiments.” In: *Journal of Applied Physics* 117.23 (2015), p. 233903.

[110] Jens Voigt. *Private communication.*